Alma Mater Studiorum – Università di Bologna

DOTTORATO DI RICERCA IN

GEOFISICA

Ciclo XXXII

Settore Concorsuale: 02/C1

Settore Scientifico Disciplinare: FIS/06

TURBULENCE IN THE ATMOSPHERIC BOUNDARY LAYER: INTERCOMPARISON AMONG ARCTIC STATIONS, DEVIATIONS FROM MOST, AND SUBMESO MOTIONS

Presentata da: Mario Schiavon

Coordinatore Dottorato

Prof.ssa Nadia Pinardi

Supervisore

Dott.ssa Oxana Drofa

Co-Supervisore

Prof.ssa Silvana Di Sabatino

Esame finale anno 2020

Summary

Monin–Obukhov similarity theory (MOST) provides a convenient framework to model the turbulent exchange in the atmospheric surface layer. However, MOST applicability is limited in several conditions: e.g., weak wind and very-stable stratification; complex terrain; presence of non-local, submeso motions. Because these conditions are common in atmospheric flows and alternative theories are lacking, their study is important for practical applications and is an area of active research.

In this work, two years of observations from three Arctic stations (located in Ny-Ålesund, Svalbard) are considered, to characterize the near-surface turbulence exchange in the area, which presents critical conditions for MOST applicability: i.e., complex terrain and long-lasting stable conditions, which favour submeso motions like gravity waves. Particular attention is dedicated to the similarity relationship between the shear stress, τ, and the vertical velocity variance, $\langle w^2 \rangle$, which are key variables to characterize the vertical turbulence exchange. Besides the stability effect predicted by MOST and the topographic influence, the effect of submeso motions on the $\tau / \langle w^2 \rangle$ similarity relationship is considered. This is done by using spectral analysis and by defining a parameter, R_τ, which quantifies the relative low-frequency contribution to the shear stress, and thus the strength of the submeso effect.

It is shown that submeso motions affect small-scale turbulence thus modifying the flux-variance similarity relationship, which, besides stability and surface characteristics, depends on R_τ. In particular, the efficiency of the vertical transport by small-scale turbulence (i.e., $\tau / \langle w^2 \rangle$ evaluated over short averaging times, i.e., $\lesssim 100\,\mathrm{s}$) diminishes for increasing submeso effect (i.e., increasing R_τ). This connects MOST applicability with more profound characteristics of the turbulent flow—i.e., the different time scales of the flow and the interplay among them—giving an alternative interpretation of MOST applicability limits found by other authors.

The effect of submeso motions on small-scale-turbulence has impacts on modelling closures and on the form of second-order moment equations. In particular, considering the budget of $\langle uw \rangle$ (i.e., the stream-wise component of the shear stress), a simple balance among shear production, buoyancy, and pressure redistribution (parametrized with a Rotta-type closure) does not hold when the submeso effect is significant (i.e., $R_\tau \gtrsim 1$). This demands for a modification of the closures (such as the pressure-redistribution time scale) and/or for an extension of the budget, with additional terms accounting for unsteadiness, vertical transport of third-order moments, and interaction of submeso motions with small-scale turbulence.

Concerning the near-surface turbulent exchange in the area, dynamics dominates on stability both for near-neutral and stable conditions. This supports the important role played by R_τ in determining turbulence behaviour and the stability independence of the vertical velocity spectrum (and thus of the small-scale-turbulence length scale), and suggests alternative roots for small-scale-turbulence production, of topographic or submeso origin.

Contents

1 Introduction

Modelling closures of the turbulent exchange in the atmospheric surface-layer are based, to a large extent, on conventional paradigms, such as down-gradient turbulent transport expressed through eddy diffusion coefficients, in analogy with molecular transport. These concepts, which underlie also Monin-Obukhov similarity theory (MOST) (Monin and Obukhov, 1954; Monin and Yaglom, 1971; Obukhov, 1971), are often used beyond their assumptions, for practical reasons or because alternatives lack. According to MOST and its extensions (e.g., Nieuwstadt, 1984b), surface-layer turbulent exchange is driven by the local vertical fluxes of heat and momentum, from which a velocity-, a temperature-, and a length-scale are obtained. When turbulence statistics are nondimensionalized with these scales, they become universal functions of stability (the only effect accounted for by MOST), which are so-called similarity relationships.

In spite of the simple and convenient framework provided by MOST, empirical evidences have also shown its limitations—and, more generally, the limitations of the conventional paradigms on which MOST is based. MOST limitations in the stable boundary layer (SBL) are well known (Mahrt, 2014). Collapse of the Richardson-Kolmogorov direct cascade has been observed, and related to MOST failure for very-stable conditions (Grachev et al., 2013). The key role of wind speed in the SBL, with this variable that affects turbulence behaviour more than vertical fluxes of heat and momentum (Sun et al., 2012, 2016; Van de Wiel et al., 2012a; Mahrt et al., 2013, 2015; Acevedo et al., 2016) has prompted the adoption of alternative paradigms, such as the Hockey-Stick Transition (HOST) hypothesis (Sun et al., 2012). Concerning unstable conditions, it is well recognized that horizontal velocity statistics do not follow MOST because of the direct effect of large-scale, convective eddies, which span the entire boundary-layer depth (Kaimal, 1978; Wilson, 2008). But critical conditions for MOST applicability occur also for near-neutral conditions when wind speed is low (Schiavon et al., 2019).

The role of submeso motions in limiting MOST applicability—for instance through non-gradient contributions to the vertical fluxes of heat and momentum—has also been recognized (Vickers and Mahrt, 2003). According to Mahrt (2014), we consider "submeso motions" as "motions between the main turbulent eddies and smallest mesoscale motions, traditionally specified to be 2 km horizontal scale" (note, however, that a clear scale separation is not always observed). Being related to many physical phenomena such as gravity waves, inertial oscillations, orographically induced wake vortices, pulsating cold air drainage, and density flows (Mahrt, 2007), submeso motions are ubiquitous and characterize a wide range of atmospheric flows (Anfossi et al., 2005; Vickers and Mahrt, 2007; Mortarini et al., 2016).

Due to their non-local origin, submeso motions are not expected to follow MOST. Hence, techniques have been developed to filter out the submeso contribution from fluxes and variances used in the evaluation of MOST similarity relationships. These techniques are usually based on spectral decompositions—such as multiresolution decomposition (Howell and Mahrt, 1997; Howell and Sun, 1999; Vickers and Mahrt, 2003)—and on the different spectral features associated to small-scale turbulence and submeso motions (e.g., Vickers and Mahrt, 2003; Falocchi et al., 2019). Their goal is the determination of the averaging time, which is chosen, when possible, in the spectral gap that divides small-scale turbulence and submeso motions. When this gap is absent, which is often the case for statistics containing horizontal velocity and temperature fluctuations, this separation is not possible and an arbitrary averaging time must be chosen. Because of the submeso contribution to second-order moments, similarity relationships are sensitive to the averaging time (Vickers and Mahrt, 2003;

Basu et al., 2006) and to data selection, with particular regard to stationarity criteria (Babić et al., 2016b). Beside the fact that stationarity is among MOST assumptions, and that it is necessary for the convergence of time averages to ensemble averages, non-stationarity (over timescales $\sim 1\,\mathrm{min}$–$1\,\mathrm{hr}$) is also related to the presence of submeso motions (Cheng and Brutsaert, 2005; Mahrt, 2007) and to different turbulence characteristics (Liang et al., 2014; Mortarini et al., 2016; Stiperski et al., 2019).

The large variability of similarity functions observed over different surfaces and in different environmental conditions (see de Franceschi et al. 2009 and Sfyri et al. 2018 for a survey of the literature) suggests that—except in simple cases such as steady flow over homogeneous surfaces—processes are missing within the MOST framework, which is challenged especially over complex terrain (Liang et al., 2014; Nadeau et al., 2013; Sfyri et al., 2018). Attempts has been made to connect this variability to flow characteristics and, in particular, to understand if a further parameter, besides stability, may affect similarity relationships. Acevedo et al. (2014) identified this parameter in the relative strength of submeso motions compared to small-scale turbulence; Stiperski et al. (2019) recognized it in the turbulence anisotropy degree. According to them, MOST "universal" similarity relationships correspond to conditions of weak submeso motions and three-dimensional, almost-isotropic turbulence, respectively. Turbulence anisotropy degree is related to the dominance of different processes in turbulence production/destruction (Stiperski and Calaf, 2018) and to different degrees of interaction between small-scale turbulence and submeso motions (Vercauteren et al., 2019).

MOST similarity relationships can be obtained from second-order moment budget equations (e.g. Zilitinkevich et al., 2013) under simplifying assumptions (i.e., steady and horizontally homogeneous turbulence and negligible divergence of third-order terms) and with appropriate closures for pressure redistribution and viscous dissipation (which are generally based on conventional paradigms). Apart from averaging issues (time averages do not converge in presence of low-frequency fluctuations), the validity of these equations in their most general form is independent of the spectral distribution of the considered variables. However, the leading terms in the budgets and the closures (i.e., velocity-, length, and temperature-scales) may change. It is thus reasonable that the spectral distribution of second-order moments may impact the existence and form of similarity relationships: for instance, differences are expected whether fluxes are dominated by three-dimensional small-scale turbulence or two-dimensional submeso motions. Furthermore, even when these equations are evaluated for small-scale turbulence only, because of the submeso effect, terms must be retained expressing the submeso–small-scale-turbulence interaction, or closures has to be changed to satisfy the budget (Mortarini et al., 2019): transfer of energy from submeso motions to small-scale turbulence has been observed in the SBL (Vercauteren et al., 2016). In some cases, such for internal gravity waves, these additional terms may be modelled (Finnigan and Einaudi, 1981; Baumert and Peters, 2009; Zilitinkevich et al., 2009). But this is not feasible for all submeso motions and when there is no scale separation with small-scale turbulence.

In this study, we compare flux-variance similarity relationships observed at three Arctic stations, located in Ny-Ålesund, Svalbard, over complex terrain. We focus mainly on the similarity relationship between the shear stress, τ, and the vertical velocity variance, $\langle w^2 \rangle$, which are key variables to characterize the vertical turbulent exchange and whose similarity relationship is robust (Acevedo et al., 2014; Stiperski et al., 2019). The effect of different surface characteristics (i.e., regular vs disturbed upwind fetch), averaging time, and stability are considered. But particular attention is dedicated also to the submeso effect by defining a parameter, R_τ, that quantifies the relative low-frequency contribution to the shear stress. Using two years of observations from the three stations, and focusing mainly on near-neutral and stable conditions (which are the most common in the area), the main goals of the work are:

- to characterize the near-surface turbulent exchange in the area, contrasting the general behaviour and differences among stations, and relating them to the local characteristics of the upstream terrain (e.g., roughness and intermediate-scale topography);
- to find MOST applicability limits, not only considering stability, but also in terms of the strength of the submeso effect (i.e., R_τ), and to relate them with the validity (or not) of conventional paradigms.

In particular, Sect. 2 describes the experiment (Sect. 2.1) and the observations used in this study (Sect. 2.2), the technique used to calculate (co)variances corresponding to different averaging times (Sect. 2.4), the choice of the averaging time used to separate small-scale turbulence from submeso motions and to define the high- and the low-frequency contribution to the shear stress (Sect. 2.5), the definition of the R_τ parameter that quantifies the relative low-frequency contribution to the shear stress, and thus the submeso effect (Sect. 2.6).

Sect. 3 deals with near-neutral conditions, which are used to characterize the topographic effect on the $\tau/\langle w^2\rangle$ relation, focusing mainly on one station, which is placed on a small hill (Sect. 3.3). Stable conditions are considered in Sect. 4, motivating the choice of the stability parameter (Sect. 4.1), considering the dependence of $\tau/\langle w^2\rangle$ on stability (Sect. 4.2), on R_τ, and on the averaging time (Sect. 4.4). An explanation for the submeso contribution to the shear stress observed at each station and its effect on $\tau/\langle w^2\rangle$ is also provided (Sect. 4.3). The stability dependence of the peak length scale of the vertical velocity spectrum, which is a key variable for modelling purposes, is presented in Sect. 4.5. Sect. 5 deals with unstable conditions, focusing on the free-convection limit.

Modelling implications of the presented results are discussed in Sect. 6, starting from second-order moments equations (Sect. 6.1) and discussing the submeso effect on closures and budgets for the case of internal gravity waves (Sect. 6.4). Then, the shear-stress budget is evaluated from observations, in stable conditions, for small and large submeso effect (Sect. 6.5). Finally, conclusions are drawn in Sect. 7.

2 Observations and Data Analysis

2.1 The Experimental Site

Ny-Ålesund (78°55′ N,11°55′ E) is located in the north-western side of Spitsbergen, Savlbard, Norway, close to the western branch of the Spitsbergen current. The experimental site faces Kongsfjorden and is surrounded by mountains and glaciers to the south and west (Fig. 1). Small lakes and rivers are present during the summer. Ny-Ålesund village, made by small buildings, is situated on

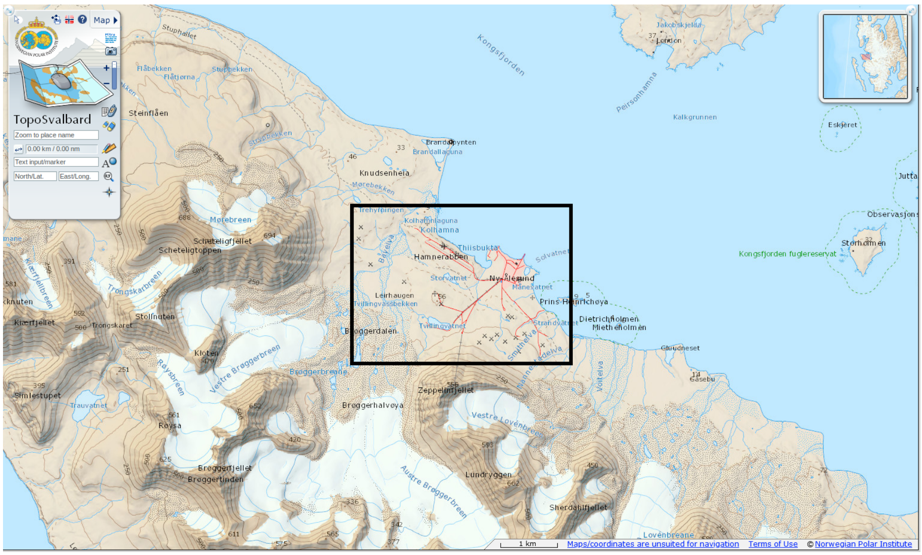

Figure 1: Topography of Kongsfjorden and Ny-Ålesund area (courtesy of the Norwegian Polar Institute). The experimental site is also indicated (black square).

Kongsfjorden coast, to the east of the airport. Roads cross the area especially in the eastern side, close to the village.

The area is characterized by complex topography and changes in surface characteristics because of land-sea-ice transitions. During the snow-free season, the ground is covered by stones and short grass, typical of arctic tundra. Snow is present from October to May-June.

Being north of the Arctic Circle, Ny-Ålesund experiences polar night and polar day conditions. During polar night, a long-lived stable boundary layer onsets. But long lasting stable conditions may occur also during the polar day and transition moths, because of the low sun and/or the snow-covered surface. This, combined with the complex topography, favour the presence of gravity waves.

Near-surface prevailing winds are from south-east and north-west, due to the channelling of synoptic winds by the fjord (Mazzola et al., 2016; Maturilli et al., 2013). For south-easterly winds, strong directional shear is present in the layer from $\approx 250\,\mathrm{m}$ up to $\approx 2\,\mathrm{km}$ because of the interaction of the westerly synoptic flow with the topography (Beine et al., 2001; Argentini et al., 2003; Maturilli and Kayser, 2017). Shallow drainage flows from the glaciers are also present and are likely related with the occurrence of gravity waves (Jocher et al., 2012).

2.2 Observations

Two years (2012–2013) of observations from three stations located in the Ny-Ålesund area are considered. The characteristics of each station relevant for this study are described below.

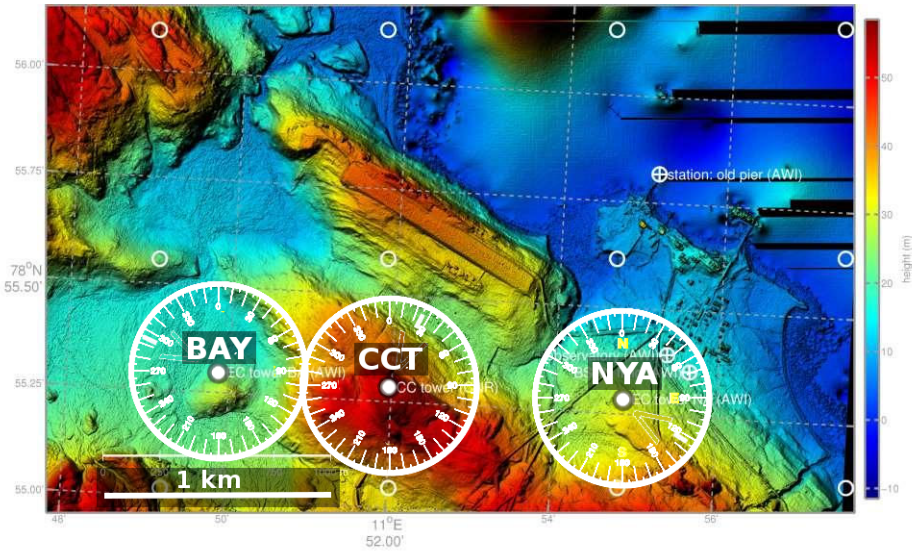

Figure 2: Close-up of the experimental site: colors refer to elevation in metres and the vertical scale of the topography is exaggerated (courtesy of A. Schulz, Alfred Wegener Institute). The three stations (NYA, BAY, and CCT) are also indicated.

2.2.1 NYA

The NYA station is located near the village of Ny-Ålesund (Fig. 2) over relatively flat terrain. The village is ≈ 1 km to the north-east; the airport relief is about at the same distance to the north-west. Several kilometres of unobstructed upwind fetch correspond to easterly wind. For snow-free conditions, the roughness length at this station is $z_0 \approx 10^{-3}$ m, typical of bare ground (Stull, 1988), while for snow-covered surface $z_0 \approx 10^{-4}$ m (Fig. S2).

The station is a 2-m mast, equipped with both slow- and fast-response sensors. Slow-response sensors measure wind speed and direction at 2 m (2.5 m after April 2013); relative humidity at 2.1 m; temperature at 2.1, 1.5, 1, and 0.5 m. Snow height is measured manually close to the station. An eddy-covariance (EC) system is placed at 2.1 m, with 20 Hz sampling rate.

In this study, the mean wind speed and direction is evaluated from the sonic-anemometer at 2.1 m —the same level where fluxes and variances are estimated. The temperature difference—used, for instance, to calculate the bulk Richardson number—is evaluated between 2.1 and 1 m, because lower thermometers may be covered by snow during the winter and changing the layer on which the temperature difference is evaluated may produce artificial variations in the bulk Richardson number. Table 1 reports the observational levels used in this study, for this and for the other stations.

2.2.2 BAY

BAY station is located near the Bayelva river (Fig. 1) and is actually composed of two stations: an EC station and a meteorological station. The latter is placed

Table 1: Measurement levels considered in this study for each station: mean wind and turbulence are measured at z; the temperature difference used to calculate the bulk Richardson number is evaluated between z_1 and z_2; heights are above snow-free ground.

Station	z (m)	z_1 (m)	z_2 (m)
NYA	2.1	1.0	2.1
BAY	2.9	1.0	2.0
CCT	3.7	4.8	2.0
	7.5	10.3	2.0

$\approx 100\,\mathrm{m}$ to the south-east of the EC station, whose position is shown in Fig. 2. The EC station is placed at the foot of a small bump with height $\approx 10\,\mathrm{m}$ (above the surrounding terrain) and horizontal scale $\approx 100\,\mathrm{m}$. The roughness length is $z_0 \approx 10^{-3}$–$10^{-2}\,\mathrm{m}$ for snow-free surface, depending on wind direction, and $z_0 \approx 10^{-4}$–$10^{-3}\,\mathrm{m}$ for snow-covered surface (Fig. S2).

At the EC station, an EC system is paced at 2.9 m above the ground, with 20 Hz sampling rate. At the meteorological station, slow-response instruments measure mean wind at 2 m, relative humidity at the same height, temperature at 2, 1, 0.2, and 0.05 m. Snow depth is measured automatically. In this study, mean wind is evaluated from the sonic anemometer at the EC station, i.e. at 2.9 m, while the temperature difference is evaluated at the meteo-station between 2 and 1 m, for the same reason discussed for the NYA station (Table 1).

2.2.3 CCT

The Climate Change Tower (CCT) is a 34-m high tower equipped with fast and slow response instruments at several levels. The CCT station is placed on a small relief with height $\approx 50\,\mathrm{m}$ and horizontal scale $\approx 500\,\mathrm{m}$, $\approx 1\,\mathrm{km}$ to the east and to the west of the BAY and NYA stations, respectively (Fig. 2). Among the three stations, it is located on the most heterogeneous terrain. The roughness length is $z_0 \approx 10^{-4}$–$10^{-3}\,\mathrm{m}$ for snow-free surface and $z_0 \approx 10^{-5}$–$10^{-4}\,\mathrm{m}$ for snow-covered surface, depending on wind direction (Fig. S2).

Mean wind, temperature and humidity are measured with slow-response instruments at 2, 4.8, 10.3, and 33.4 m above the ground. Three sonic anemometers are placed at intermediate levels, i.e., at 3.7, 7.5 and 20.5 m, with sampling frequencies of 21, 20, and 10 Hz, respectively. Data from 20.5 m are not considered in this study, because this level is too high compared with other stations and may be above the surface-layer (Sect. 3.3). Also for this station, mean wind is evaluated from sonic-anemometer measurements, while the temperature difference is calculated between 2 and 4.8 m for the layer corresponding to $z = 3.7\,\mathrm{m}$, and between 2 and 10.3 m for $z = 7.5\,\mathrm{m}$ (Table 1). Snow height is measured automatically.

Except when differently indicated, results corresponding to the CCT stations are obtained combining together observations from 3.7 and 7.5 m, to improve statistic and because differences in the results for the two levels are generally small.

2.3 Data Processing and Selection

Raw data are divided in 30-min records. For each record, the sonic reference system is aligned with the 30-min mean wind vector and then (co)variances are computed as 30-min block averages. Prior to calculate 30-min averages, raw data are checked for spikes, plausibility limits, and gaps.

Disturbed sectors (by the tower structure, at the CCT station, or by the sensor, at the NYA and BAY stations) are excluded from the analysis. The excluded sectors are: 200°–310° at the NYA station; 300°–360° and 0°–50° at the BAY station; 150°–270° at the CCT station. At the NYA and BAY stations, spectra in these sectors are dominated by high-frequency noise. The effect of precipitation and blowing snow has also been checked. The 3.7 m sonic anemometer at the CCT station turned out to be affected by blowing snow and thus these records are discarded for this anemometer.

Data corresponding to snow-free and snow-covered surface are considered together because results do not differ appreciably for the two conditions—the main effect of the snow cover is the variation of the roughness length, and its possible impact on the results is discussed in Sect. 3.

2.4 Multiresolution Decomposition

Besides to calculate them from 30-min block averages, (co)variances corresponding to different averaging times are estimated using the multiresolution decomposition (MRD) (Howell and Mahrt, 1997; Howell and Sun, 1999; Vickers and Mahrt, 2003). For each 30-min record, MRD spectra are calculated over the first 2^N samples , where N is the largest integer such that $2^N \leq M$, M the number of samples in each 30-min record: with a sampling rate of 20 Hz, this corresponds to the first ≈ 1600 s of each 30-min record. Then, the (co)variance corresponding to a given averaging time, T, is calculated integrating[1] the MRD (co)spectra from the smallest time scale up to T. Figure 3 shows an example of MRD (co)spectrum and corresponding integrated (co)spectrum.

Contrary to Fourier transform, MRD does not require periodicity. And (co)variances calculated by integrating MRD (co)spectra satisfy Reynolds averaging. Indeed, the MRD (co)variance corresponding to the averaging time T can be re-obtained dividing the 30-min record in subrecords of duration T, computing the (co)variance for each subrecord, and the averaging over all the subrecords.

Hereafter, the MRD (co)spectrum of α and β (where α and β can be velocity or temperature fluctuations) is indicated by $\alpha\beta(T)$, and corresponds to the contribution from the timescale T to the (co)variance between α and β. The MRD integrated (co)spectrum is indicated as $\langle\alpha\beta\rangle_T$, and corresponds to the (co)variance calculated with the averaging time T (angle brackets indicate averaging).

2.5 Choice of the Averaging Time

MRD (co)spectra are often used to set the averaging time, which is chosen in the spectral gap, i.e. the region that separates small-scale turbulence and submeso motions where (co)spectra attain very small values. For scales smaller than

---

[1] The integration, is this case, is actually a summation.

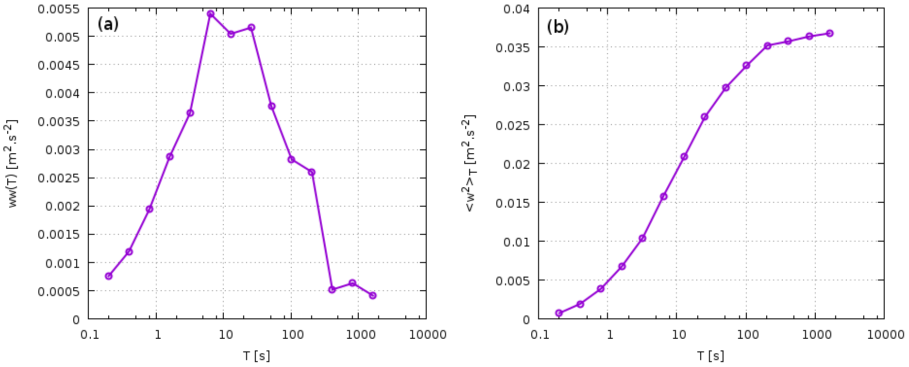

Figure 3: Examples of (a) spectrum and (b) integrated spectrum from MRD, in this case for the vertical velocity variance: (a) $ww(T)$ is the contribution to vertical velocity variance from the time scale T; (b) $\langle w^2 \rangle_T$ is the vertical velocity variance corresponding to the averaging time T, obtained by summing all the contributions in (a) from the smallest time up to T.

the gap scale, heat and momentum vertical fluxes are down-gradient; for larger scales, fluxes are erratic and can have both signs. The gap is more recognizable in "average" cospectra, obtained combining several cospectra, because the low-frequency end of single cospectra is characterized by large variability.

Figure 4 shows median MRD spectral distributions of several variables at the three stations for unstable and stable conditions identified according to the bulk Richardson number (e.g. Tampieri, 2017)

$$R_\mathrm{b} \equiv \frac{\beta z^2 \Delta\Theta(z_1, z_2)}{U^2(z)(z_2 - z_1)}, \tag{1}$$

where U is the 30 min mean wind speed (vectorial average) at the height z (corrected for the snow depth); $\Delta\Theta(z_1, z_2) \equiv \Theta(z_2) - \Theta(z_1)$ is the mean potential temperature difference between z_2 (close to z) and z_1 (close to the ground); $\beta \equiv g/\Theta(z_2)$ is the buoyancy parameter (the values of z, z_1, and z_2 for each station are reported in Table 1).

In Fig. 4, T is the MRD time scale, which is equivalent to the averaging time. Variances and covariances corresponding to the averaging time T are obtained by integrating MRD (co)spectra from the shortest time scale up to T. The spectral gap corresponds to a stationary point in the integrated (co)spectra, i.e., a region where the (co)variances do not change significantly with the averaging time.

For unstable conditions (Fig. 4a,c,e), the spectral distribution of the vertical velocity variance, the fluxes of heat and stream-wise momentum, and the temperature variance have a similar shape, with a well defined maximum in the high-frequency range, at $T < 100$ s. On the contrary, MRD spectra of the variances of the horizontal velocity components increase with averaging time without reaching any maximum. The fact that some variables have similar spectral shapes, suggest close relationships among them.

For stable conditions (Fig. 4b,d,f), the spectral distribution of the vertical velocity variance still has a well defined maximum in the high-frequency range, at $T \approx 1$–10 s, but the distributions of the heat and momentum fluxes, and that of the temperature variance, change significantly compared to the unstable case.

At all stations, for stable conditions, the median heat flux cospectrum has a gap at $T \approx 100\,\mathrm{s}$ (Fig. 4b, d, and f; black dash-dotted line). This is a typical gap time scale for the heat flux, and thus $T \approx 100\,\mathrm{s}$ is often used to separate submeso motions and small-scale turbulence (e.g., Vickers and Mahrt, 2003, 2006; Stiperski and Calaf, 2018; Stiperski et al., 2019). We thus use 100 s as cut-off time to separate the high-frequency contribution due to small scale turbulence ($T < 100\,\mathrm{s}$) from the low-frequency contribution due to submeso motions ($100\,\mathrm{s} < T < 30\,\mathrm{min}$, the record length). In agreement with several authors (cf., e.g., Nieuwstadt, 1984b; Basu et al., 2006; de Franceschi et al., 2009; Grachev et al., 2013; Stiperski and Calaf, 2018; Stiperski et al., 2019) we use a fixed cut-off time—the effect of this choice is discussed in Sec. 4.3. This is a first approximation and more refined analyses accounting for the variability of the cut-off time scale (Vickers and Mahrt, 2003; Falocchi et al., 2019) are left for future research.

For unstable conditions, the low-frequency contribution to heat flux is generally negligible (Figs. 4a, c, and e). As it is negligible the low-frequency contribution to the vertical velocity variance, both for stable and unstable conditions. The spectral distribution of these two statistics always peaks in the high-frequency range and gently decays for $T > 100\,\mathrm{s}$. The vertical velocity variance is always dominated by small scales because vertical velocity fluctuations with scale $\gg z$ are inhibited by the presence of the ground (e.g., Højstrup, 1982). The similar spectral distribution of the heat flux and the vertical velocity variance for unstable conditions roots in the dominance of the gradient production term $(-\sigma_w^2 \partial\Theta/\partial z)$ in the heat-flux budget equation (Eq. 20).

The major effect of the low-frequency contribution is thus expected for stable conditions. Figure 5 shows the heat flux vs the vertical temperature difference at the NYA and BAY stations, considering 30-min and 100-s covariances, i.e., $\langle w\theta\rangle_{30\mathrm{min}}$ and $\langle w\theta\rangle_{100\mathrm{s}}$, respectively. For unstable temperature stratification ($\Delta\Theta <$ zero), the heat flux is well correlated with the local temperature difference independently of the averaging time. Whereas, for stable temperature stratification, positive heat fluxes are observed, despite $\Delta\Theta >$ zero, when 30-min covariances are considered (Figs. 5a,c) while their occurrence is practically eliminated for 100-s covariances (Figs. 5b,d; cf. Vickers and Mahrt, 2003, 2006). A non-gradient low-frequency contribution to the heat flux estimated with the eddy-covariance technique can be produced by gravity waves (Foken and Wichura, 1996; Fritts et al., 2009), which are common in Ny-Ålesund due to the topography and the long lasting stable conditions. For instance, gravity waves have been observed at the NYA station (Jocher et al., 2012).

2.6 The R_τ Parameter

According to Sect. 2.5, $T = 100\,\mathrm{s}$ is used as cut-off time at all stations for near-neutral and stable conditions. This defines a high-frequency contribution—from time scales $\leq 100\,\mathrm{s}$—and a low-frequency contribution—from time scales $> 100\,\mathrm{s}$ and $\leq 30\,\mathrm{min}$ (the record length). The former is dominated by small-scale turbulence, the latter, by submeso motions.

Likely related to a variety of non-local phenomena, the the low-frequency contribution to variances and covariances is not expected to depend on local flow characteristics, such as stability or wind speed. Figure. 6 shows the vari-

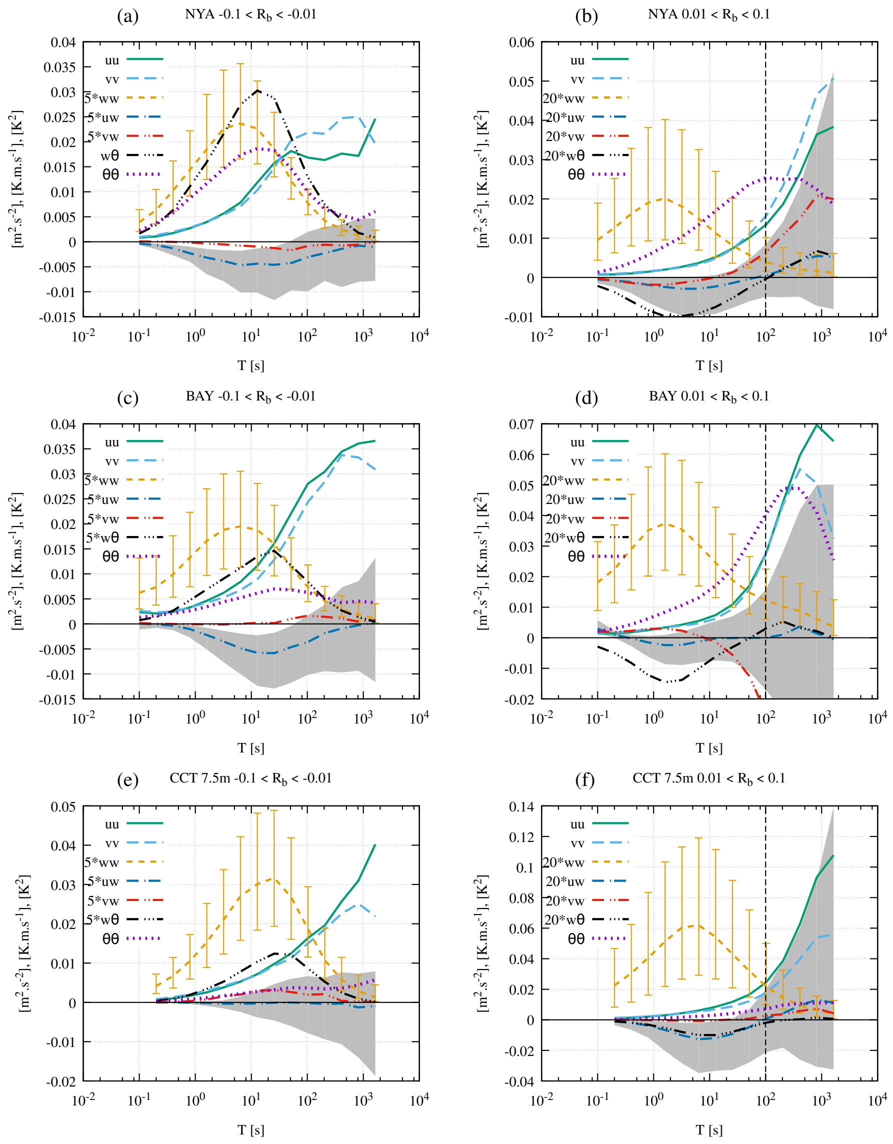

Figure 4: MRD spectral distribution of several (co)variances, at the three stations, for unstable (left) and stable (right) stratification. The represented statistics are: the variance of the three velocity components (uu, vv, and ww); the vertical flux of momentum (stream-wise-, uw, and crosswind-component, vw); the vertical heat flux ($w\theta$); the temperature variance ($\theta\theta$). Median (co)spectra are reported for each statistic (lines); (co)spectra variability, i.e., 25th–75th percentile range, is reported only for ww (error bars) and uw (grey area); for representation purposes, spectral distributions of ww, uw, vw, and $w\theta$ are multiplied by 5 and 20 for unstable and stable conditions, respectively. T is the MRD time scale; the averaging time used in the study for near-neutral and stable conditions, $T = 100\,\mathrm{s}$, is also indicated. CCT (co)spectra refer to $z = 7.5\,\mathrm{m}$.

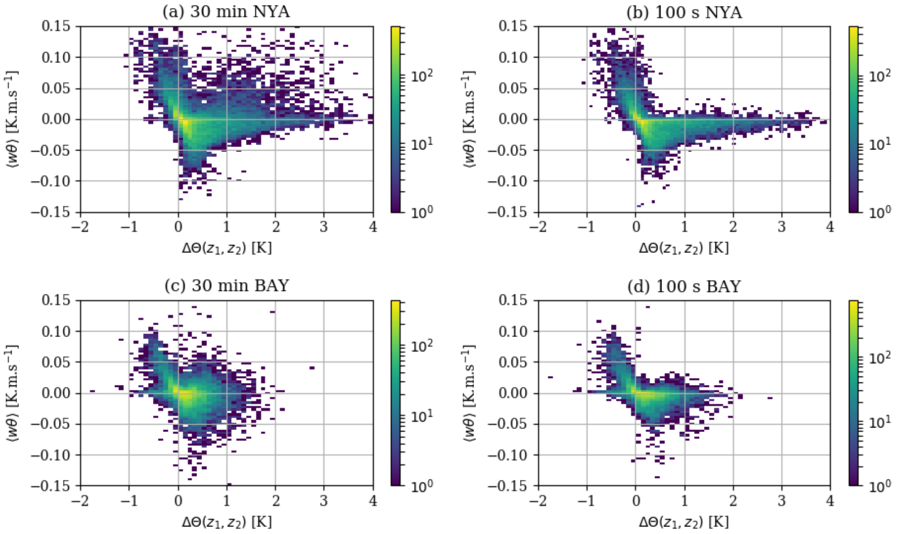

Figure 5: 30-min and 100-s kinematic heat flux vs potential-temperature difference at the NYA and BAY stations (z_1 and z_2 in Table 1). Colours correspond to the number of data points in each pixel (on a logarithmic scale).

ation with R_b of the high-frequency and the low-frequency contribution to the shear stress and to the heat flux, for $R_\mathrm{b} > 0$, at all stations. The high-frequency contribution to the shear stress, $\tau_{100\mathrm{s}}$, decreases as R_b^{-1} up to $R_\mathrm{b} \approx 10^{-2}$ (because $R_\mathrm{b} \sim U^{-2}$ and $\tau_{100\mathrm{s}} \sim U^2$) and then levels off (Fig. 6a). This behaviour is similar to that found when wind speed is used as independent parameter (e.g., Sun et al., 2012; Van de Wiel et al., 2012b; Mahrt et al., 2015; Acevedo et al., 2016), because, at least for the considered datasets, variations in R_b are mainly driven by U. Like $\tau_{100\mathrm{s}}$, the high-frequency contribution to the heat flux (Fig. 6c), $\langle w\theta \rangle_{100\mathrm{s}}$, depends on R_b in a way that is qualitatively consistent with results from other ABL experiments (Mauritsen et al., 2007) and with MOST predictions (Van de Wiel et al., 2012b). Conversely, no clear relation exists between local stability and the low-frequency contribution to the shear stress, $|\tau_{30\mathrm{min}} - \tau_{100\mathrm{s}}|$, and to the heat flux, $|\langle w\theta \rangle_{30\mathrm{min}} - \langle w\theta \rangle_{100\mathrm{s}}|$, which are, respectively, $\approx 10^{-2}\,\mathrm{m}^2\,\mathrm{s}^{-2}$ and $\approx 10^{-3}$–$10^{-2}\,\mathrm{K\,m\,s}^{-1}$ on average, independently of R_b (Fig. 6b,d). The magnitude of the low-frequency contribution to the heat- and momentum-flux is also independent of the high-frequency contribution, as can be noted comparing Fig. 6a and c with Fig. 6b and d.

Since the magnitude of the high-frequency contribution decreases with stability while the low-frequency contribution is almost constant, the relative magnitude of the low-frequency contribution increases with stability (Fig. 7a): on average, the low-frequency contribution to the shear-stress becomes dominant for $R_b \gtrsim 10^{-2}$. Similarly, because the low- and the high-frequency contributions are almost independent, on average, R_τ increases with decreasing $\tau_{100\mathrm{s}}$ (Fig. 7b). This means that R_τ, R_b, and $\tau_{100\mathrm{s}}$ are not fully independent—but they are neither equivalent. Figure 7 also shows that $R_\tau \approx 1$, $R_\mathrm{b} \approx 10^{-2}$, and $\tau_{100\mathrm{s}} \approx 10^{-2}\,\mathrm{m}^2\,\mathrm{s}^{-2}$ roughly correspond to each other: it will be shown that

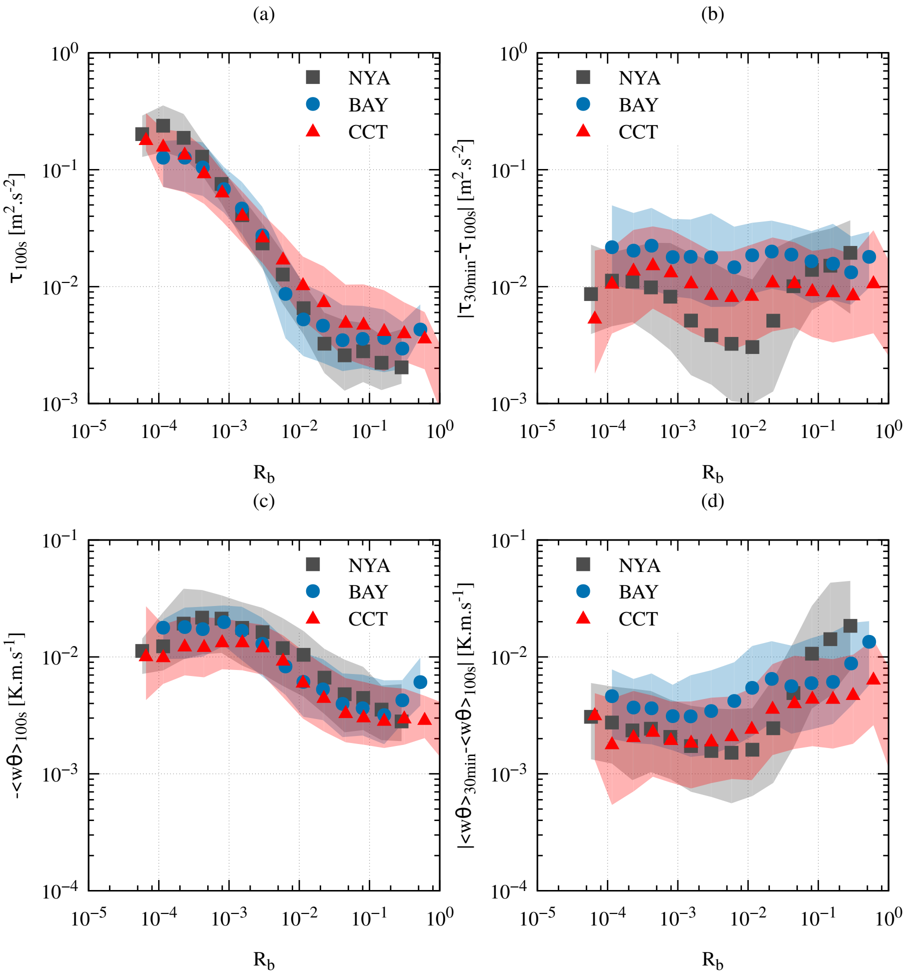

Figure 6: High- and low-frequency contribution to the shear stress (i.e., $\tau_{100\mathrm{s}}$ and $|\tau_{30\mathrm{min}} - \tau_{100\mathrm{s}}|$, respectively) and to the heat flux (i.e., $-\langle w\theta\rangle_{100\mathrm{s}}$ and $|\langle w\theta\rangle_{30\mathrm{min}} - \langle w\theta\rangle_{100\mathrm{s}}|$) vs bulk Richardson number, R_b, at the three stations (all wind directions) for stable conditions, $R_\mathrm{b} > 0$: data are binned in R_b; median values (points) and 25th–75th percentile range (shaded area) are shown for each bin containing at least 10 data points.

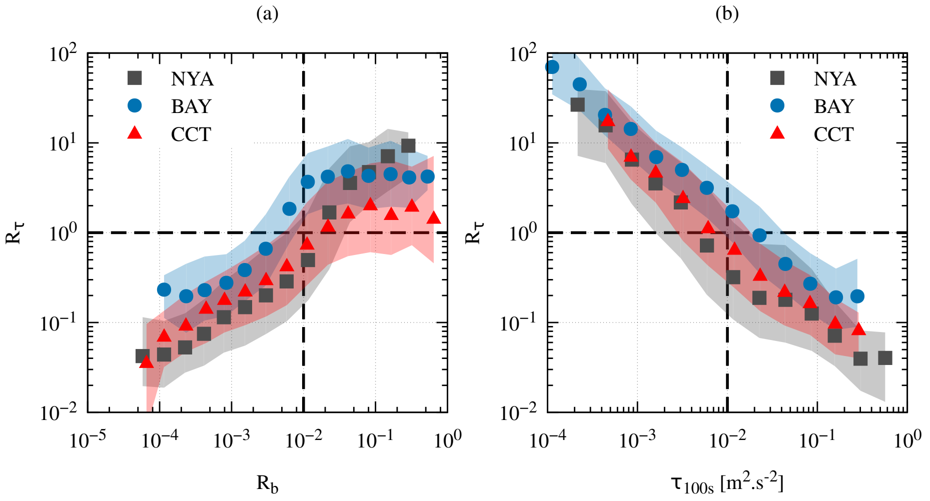

Figure 7: R_τ, Eq. 2, vs (a) R_b and (b) τ_100s (for $R_b > 0$). Data are binned in R_b and τ_100s: median values and 25th–75th percentile range are reported for each station, along with the "critical" values $R_\tau = 1$, $R_\mathrm{b} = 10^{-2}$, and $\tau_\mathrm{100s} = 10^{-2}\,\mathrm{m}^2\,\mathrm{s}^{-2}$

these three values mark the transition towards critical conditions for MOST applicability (Sect 4).

Because modes with time scale comparable with the record length (i.e., 30 min) are poorly sampled, the low-frequency contribution estimated as the numerator in Eq. 2 is significantly affected by statistical errors and, for each record, depends on the upper cut-off time in a non-systematic way. However, despite this uncertainty, a physical interpretation can be given "on average", by considering many records (Acevedo and Mahrt, 2010).

According to the above considerations and to use it in the following analysis, we define the relative low-frequency contribution to the shear stress

$$R_\tau \equiv \left| \frac{\tau_\mathrm{30min} - \tau_\mathrm{100s}}{\tau_\mathrm{100s}} \right|, \tag{2}$$

which quantifies

- the relative strength of submeso phenomena that may cause turbulence to not be in local equilibrium, and
- the deviation of experimental conditions from those where MOST, Reynold's averaging, and eddy-covariance assumptions are fulfilled.

Concerning the general idea, R_τ is similar to the "submeso" index of Acevedo et al. (2014) and the stationarity index proposed by Foken and Wichura (1996), and the relative meandering of the shear-stress vector by Mahrt (2007, Eq. 10).

R_τ, Eq. 2, quantifies the submeso effect on the magnitude of the shear stress. But submeso motions can also change the direction of the shear-stress vector without modifying appreciably its magnitude. A more restrictive parameter is thus

$$R^*_\tau \equiv \frac{\sqrt{(\langle uw \rangle_\mathrm{30min} - \langle uw \rangle_\mathrm{100s})^2 + (\langle vw \rangle_\mathrm{30min} - \langle vw \rangle_\mathrm{100s})^2}}{\tau_\mathrm{100s}}, \tag{3}$$

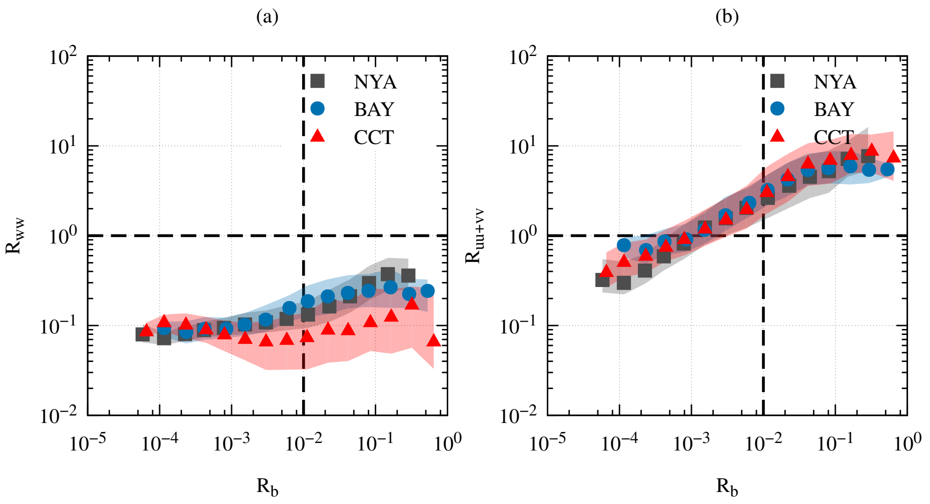

Figure 8: Dependence on R_b of the relative low-frequency contribution to (a) the vertical velocity variance, $\langle w^2\rangle$, and (b) the horizontal velocity variance, $\langle u^2\rangle + \langle v^2\rangle$, from Eq. (4): bin median and 25th–75th percentile range are shown for the three stations. The critical values $R_{ww} = R_{uu+vv} = 1$ and $R_\mathrm{b} = 10^{-2}$ are also indicated.

which takes into account also the low-frequency meandering of the shear-stress, like the index by Mahrt (2007). The impact of using R^*_τ instead of R_τ has been tested on some of the presented results and turned out to be small. Thus, R_τ is used to classify observations.

The definition of R_τ, Eq. 2, can be extended to any second-order moment $\langle\alpha\beta\rangle$:

$$R_{\alpha\beta} \equiv \left| \frac{\langle\alpha\beta\rangle_{30\mathrm{min}} - \langle\alpha\beta\rangle_{100\mathrm{s}}}{\langle\alpha\beta\rangle_{100\mathrm{s}}} \right|, \tag{4}$$

where α and β are, for instance, velocity and temperature fluctuations. Clearly, the physical interpretation of Eq. 4 as the relative submeso contribution to $\langle\alpha\beta\rangle$ is unreliable for those variables that do not have a spectral gap around 100 s, such as $\langle u^2\rangle$, $\langle v^2\rangle$, and $\langle\theta^2\rangle$ (Fig. 4b,d,f).

Figure 8 shows the relative low-frequency contribution, Eq. 4, to the vertical velocity variance, $\langle w^2\rangle$ and to the horizontal velocity variance, $\langle u^2\rangle + \langle v^2\rangle$, plotted against R_b. The low-frequency contribution to the vertical velocity variance, R_{ww}, is always negligible for $R_\mathrm{b} \lesssim 10^{-2}$ and $\ll 1$ also for $R_\mathrm{b} > 10^{-2}$: $R_{ww} = 0$, in first approximation. This is because the distance from the ground acts like a high-pass filter on vertical velocity fluctuations (Højstrup, 1982), greatly attenuating length scales $\gg z$. However, low-frequency (large-scale) fluctuations can contribute with no limitation to the horizontal velocity components, whose variances are indeed dominated by the low-frequency contribution (Fig. 8b). The two-dimensional nature is a distinctive feature of meandering motions in the surface-layer (Mortarini et al., 2016, 2019).

3 Near-Neutral Conditions

Because of the different surface characteristics, variations in $\tau/\langle w^2\rangle$ among stations and wind direction sectors are expected (Fortuniak et al., 2013; Babić et al., 2016a). Furthermore, when the low-frequency contribution to the shear stress is significant—which happens also for near-neutral conditions—$\tau/\langle w^2\rangle$ depends on the averaging time. It is well known that similarity relationships found in different experiments differ also in their neutral limit (de Franceschi et al., 2009). This variability may be explained in terms of different surface characteristics but also on different choices made by different authors: for instance the choice of the averaging time or the definition of the shear stress, i.e., $\tau \equiv \sqrt{\langle uw\rangle^2 + \langle vw\rangle^2}$ or $\tau \equiv \langle -uw\rangle$, (Wilson, 2008). The question is whether this variability is related also to the low-frequency contribution to τ.

Near-neutral conditions are selected by imposing $|R_\mathrm{b}| < 0.001$. However, similar results are obtained if $|z/\Lambda_{100\mathrm{s}}| \lesssim 0.01$ is considered, where

$$\Lambda_{100\mathrm{s}} \equiv -\frac{\tau_{100\mathrm{s}}^{3/2}}{\beta\kappa\langle w\theta\rangle_{100\mathrm{s}}} \tag{5}$$

is the local Obukhov length (e.g., Nieuwstadt, 1984a) calculated from 100-s fluxes (with von Kármán constant $\kappa = 0.4$). To restrict the analysis to well developed turbulence, $\tau_{100\mathrm{s}} > 0.01\,\mathrm{m^2\,s^{-2}}$ is also imposed.

3.1 Dependence on Wind Direction

Figure 9 shows the variation with wind direction in the near-neutral value of $\tau_{100\mathrm{s}}/\langle w^2\rangle_{100\mathrm{s}}$ at the three stations, for $R_\tau < 0.3$ and > 1, which, hereafter, identify cases with small and large low-frequency contribution, respectively.

The near-neutral value of $\tau_{100\mathrm{s}}/\langle w^2\rangle_{100\mathrm{s}}$ varies among stations and wind direction sectors. This variation is consistent with the complex topography of the area (Fig. 2) and, with the exception of particularly small values found at the CCT station (Fig. 9c), with the range of values reported in the literature (de Franceschi et al., 2009): for $R_\tau < 0.3$, $\tau_{100\mathrm{s}}/\langle w^2\rangle_{100\mathrm{s}} \approx 0.6$–1, 0.5–0.7, and 0.3–0.7 at the NYA, BAY, and CCT station, respectively (green shaded area in Fig. 9).

Observations suggest that larger $\tau_{100\mathrm{s}}/\langle w^2\rangle_{100\mathrm{s}}$ corresponds to more regular upwind fetch. This is particularly evident at the NYA station (Fig. 9a, green area), where $\tau_{100\mathrm{s}}/\langle w^2\rangle_{100\mathrm{s}} \approx 1$ in sectors with most regular fetch, such as 80°–100° and 340°–350°, and decreases to ≈ 0.6 in more disturbed sectors, such as around 150° and 320°, where there is the airport relief (Fig. 2). Furthermore, the smallest values of $\tau_{100\mathrm{s}}/\langle w^2\rangle_{100\mathrm{s}}$ are observed at the CCT station that, among the three stations, is located on the most heterogeneous terrain (Fig. 2). In particular, $\tau_{100\mathrm{s}}/\langle w^2\rangle_{100\mathrm{s}} \approx 0.3$ at this station for westerly wind (Fig. 9c), which is among the directions that correspond to the steepest slope of the CCT relief—the other, north-east, has few data. The CCT case is further discussed in Sect. 3.3, using results from experiments and numerical simulations of flow over hills.

The effect of R_τ on $\tau_{100\mathrm{s}}/\langle w^2\rangle_{100\mathrm{s}}$ depends on the station: is negligible at the BAY station, where the ratio has roughly the same value for $R_\tau < 0.3$ and > 1 (Fig. 9b); is large at the CCT station, where $\tau_{100\mathrm{s}}/\langle w^2\rangle_{100\mathrm{s}}$ is halved for

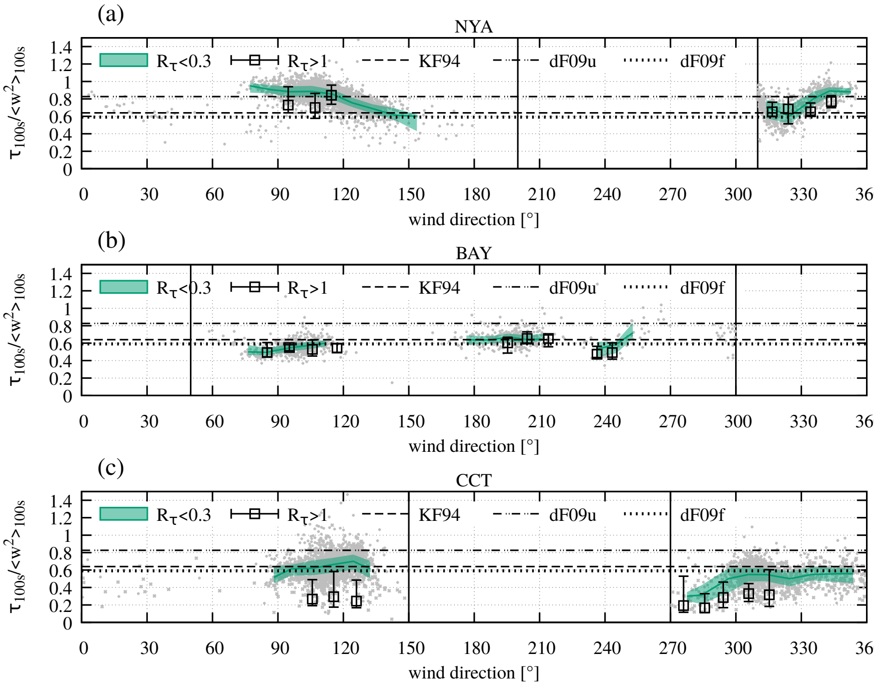

Figure 9: $\tau_{100\mathrm{s}}/\langle w^2\rangle_{100\mathrm{s}}$ vs wind direction for near-neutral conditions at the three stations: $|R_\mathrm{b}| < 10^{-3}$, $\tau_{100\mathrm{s}} > 0.01\,\mathrm{m}^2\,\mathrm{s}^{-2}$, and $R_\tau < 0.3$. All data points (corresponding to each 30-min record) are shown along with median values (green line) and 25th–75th percentile range (green shaded area) in wind-direction bins; neutral limits of similarity relationships from Kaimal and Finnigan (1994, KF94) and de Franceschi et al. (2009, along valley, unfiltered, dF09u, and filtered, dF09f) are reported; excluded sectors are also indicated.

$R_\tau > 1$ (Fig. 9c). This may be due to the characteristic position of the CCT station, which is placed on a small hill (Fig. 2) and the consequent topographic effect (Sect. 3.3): topography induces/enhances low-frequency fluctuations of horizontal velocity components (Sect. 3.3.2) and thus larger R_τ corresponds to larger topographic effect.

Since topography triggers submeso motions like gravity waves, inertial oscillations and wake vortices, the question raises whether R_τ is correlated with fetch characteristics: that is, whether larger R_τ corresponds to more irregular upwind fetch. However, a straightforward relation between the variation in R_τ with wind direction and the characteristics of the upwind fetch up to distances of $\sim 100\,\mathrm{m}$–$1\,\mathrm{km}$ from the station is not observed: but topography can enhance both the low- and the high-frequency contribution without producing a significant variation in R_τ. At the NYA station, however, the smallest values of R_τ correspond to the sectors with the most uniform fetch, such as north and east (Fig. 2). But R_τ at the CCT station is generally lower than at the other stations, despite the former presents the most irregular fetch.

Concerning the dependence of the relative low-frequency contribution on surface-roughness (Mahrt et al., 2013)—the low-frequency contribution being influenced by mesoscale topography, the high-frequency contribution, by surface roughness—only minor and not systematic variations in R_τ correspond to different surface types: i.e., snow-free vs snow-covered surface. This is why no distinction is made between cases of snow-free and snow-covered surface.

3.2 Dependence on the Averaging Time

Due to the low-frequency contribution to the shear stress, $\tau/\langle w^2\rangle$ depends on the averaging time. Figure 10 shows the near-neutral value of $\tau/\langle w^2\rangle$ at the three stations for 100-s and 30-min covariances; $\langle -uw\rangle/\langle w^2\rangle$ is also considered because, in general, $\tau \neq \langle -uw\rangle$ (Wilson, 2008).

When $R_\tau < 0.3$, the shear stress, and thus $\tau_T/\langle w^2\rangle_T$, do not depend on T if the averaging time is long enough, i.e., if $T \gtrsim 100\,\mathrm{s}$. Considering all wind directions together, the near-neutral value of $\tau_{100\mathrm{s}}/\langle w^2\rangle_{100\mathrm{s}}$ at the three stations is in the range reported in the literature (Fig. 10a): considering median values, $\tau_{100\mathrm{s}}/\langle w^2\rangle_{100\mathrm{s}} = 0.82$ at NYA, 0.59 at BAY, and 0.58 at CCT. NYA is the only station having unobstructed sectors with flat upwind fetch for distances $> 1\,\mathrm{km}$ (Fig. 2): this explains its particularly large $\tau_{100\mathrm{s}}/\langle w^2\rangle_{100\mathrm{s}}$ (Fig. 9a). Since the crosswind component of the 100-s shear stress is small but not always negligible, $\langle -uw\rangle_{100\mathrm{s}}/\langle w^2\rangle_{100\mathrm{s}} < \tau_{100\mathrm{s}}/\langle w^2\rangle_{100\mathrm{s}}$ (compare Fig. 10a and c): considering median values, $\langle -uw\rangle_{100\mathrm{s}}/\langle w^2\rangle_{100\mathrm{s}} = 0.81$ at NYA, 0.51 at BAY, and 0.55 at CCT.

When $R_\tau > 1$, the shear stress depends on the averaging time. In particular, τ_T increases with T also for $T > 100\,\mathrm{s}$ because of the low-frequency contribution to the cross-wind component (Fig. S1b,d,f), which is particularly large at the NYA and BAY stations. Since this low-frequency contribution augments the shear stress while leaving almost unaffected the vertical velocity variance, $\tau_{30\mathrm{min}}/\langle w^2\rangle_{30\mathrm{min}} > \tau_{100\mathrm{s}}/\langle w^2\rangle_{100\mathrm{s}}$ (Fig. 10b). This agrees with Babić et al. (2016b, their Figs. 3,4), who find an increase in the neutral limit of $\langle w^2\rangle_{30\mathrm{min}}/\tau_{30\mathrm{min}}$ as more stationary conditions are selected: which roughly corresponds to smaller R_τ in our case. However, no systematic variations are found when only the stream-wise component is considered: $\langle -uw\rangle_{30\mathrm{min}}/\langle w^2\rangle_{30\mathrm{min}} \approx$

$\langle -uw \rangle_{100\mathrm{s}}/\langle w^2 \rangle_{100\mathrm{s}}$, on average, and the scatter of the data increases (Fig. 10d).

As noted in the previous section, the effect of R_τ on $\tau_{100\mathrm{s}}/\langle w^2 \rangle_{100\mathrm{s}}$ depends on the station (compare Fig. 10a and b), being large at CCT and small at BAY. But, from $R_\tau < 0.3$ to $R_\tau > 1$, $\langle -uw \rangle_{100\mathrm{s}}/\langle w^2 \rangle_{100\mathrm{s}}$ decreases at all stations, although with different magnitudes (compare Fig. 10c and d).

As it will be shown in Sect. 4.3, a negative submeso contribution to $\langle -uw \rangle$ is observed at all stations for stable conditions. This negative submeso contribution erodes the positive contribution due to small-scale turbulence thus reducing $\langle -uw \rangle_{100\mathrm{s}}/\langle w^2 \rangle_{100\mathrm{s}}$ for $R_\tau > 1$. $\tau_{100\mathrm{s}}/\langle w^2 \rangle_{100\mathrm{s}}$ does not decrease to the same extent because of the submeso contribution to $\langle vw \rangle_{100\mathrm{s}}$, which balances the decreased $\langle -uw \rangle_{100\mathrm{s}}$. However, there are no evidences of a systematic, negative submeso contribution to $\langle -uw \rangle_{100\mathrm{s}}$ in this case—i.e., near-neutral conditions and $\tau > 0.01\,\mathrm{m}^2\,\mathrm{s}^{-2}$—although there is indeed a systematic submeso contribution to $\langle vw \rangle_{100\mathrm{s}}$ especially at the NYA and BAY stations (Fig. S1). Because of this, the 100-s shear stress is not aligned with the 30-min mean wind, $\langle -uw \rangle_{100\mathrm{s}}$ and $\langle vw \rangle_{100\mathrm{s}}$ having similar magnitudes (Fig. S1b,d,e).

Hence, the decrease $\langle -uw \rangle_{100\mathrm{s}}/\langle w^2 \rangle_{100\mathrm{s}}$ for increasing R_τ suggests an interaction of small-scale turbulence and submeso motions that originates additional terms in second-order moment budget equations for small-scale turbulence (Finnigan et al., 1984; Zilitinkevich et al., 2007). Even if evaluated for 100-s (co)variances, the flux-variance similarity relationships may change because of these additional terms.

The particularly small values of $\tau_{100\mathrm{s}}/\langle w^2 \rangle_{100\mathrm{s}}$ and $\langle -uw \rangle_{100\mathrm{s}}/\langle w^2 \rangle_{100\mathrm{s}}$ observed at the CCT station (Fig. 10b,d) are likely related to topographic effects (Sec. 3.3). Since orography enhances the low-frequency contribution to horizontal velocity components, larger R_τ should correspond to stronger topographic perturbation.

3.3 Topographic Effects at the CCT Station

The CCT station is placed at the top of a relief, with horizontal length scale $L \approx 500\,\mathrm{m}$ and height $H \approx 50\,\mathrm{m}$. Roughness is assumed uniform in the area of interest.

From literature (e.g., Zeman and Jensen 1987, Eqs. 13–17 and Ying and Canuto 2007, Eqs. 42–44) second-order moment equations written in streamline coordinates contain a term depending on the streamlines curvature, R. Moreover, terms related to horizontal inhomogeneity (i.e., $\partial/\partial x$) cannot be neglected. This means that, for instance, in steady and neutral conditions, the TKE budget contains—besides shear production and viscous dissipation—further terms related to $\partial E_\mathrm{K}/\partial x$, $\partial U/\partial x$, and $\langle uw \rangle U/R$, where the latter is the curvature term. At the hilltop, $R > 0$, and the curvature term has opposite sign with respect to shear production, thus acting as a sink of TKE (Zeman and Jensen, 1987, Eq. 16)—in this sense, the curvature effect is similar to the stability effect.

An important scale in this problem is the height of the inner layer, l_i. Taking $L \approx 500\,\mathrm{m}$ and $H \approx 50\,\mathrm{m}$ as representative values for the CCT case, $l_i \approx 20\,\mathrm{m}$ if the formula by Jackson and Hunt (1975) is used, or $\approx 7\,\mathrm{m}$ (i.e., $\approx 1/3$ of the Jackson and Hunt (1975) value), if results by Zeman and Jensen (1987) are considered. Most of the CCT data refer to $z = 7.5\,\mathrm{m}$ measurement levels, close to the latter estimate of l_i.

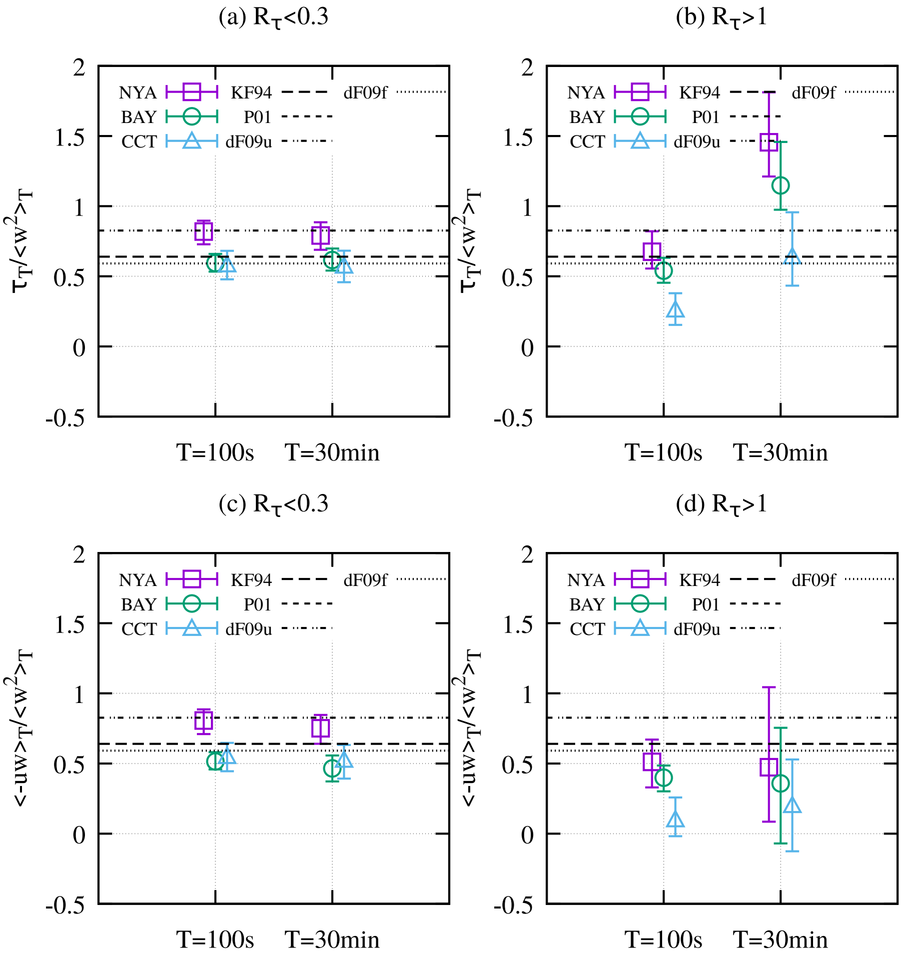

Figure 10: Near-neutral values of $\tau_T/\langle w^2\rangle_T$ (up) and $\langle -uw\rangle_T/\langle w^2\rangle_T$ (bottom) at the three stations, for $R_\tau < 0.3$ (left) and > 1 (right), and $T = 100\,\mathrm{s}$ and 30 min: median value and 25th–75th percentile range is shown for each station and averaging time (all wind directions); neutral limits of similarity relationships from Kaimal and Finnigan (1994, KF94), Pahlow et al. (2001, P01), and de Franceschi et al. (2009, along valley: filtered, dF09f, and unfiltered, dF09u) are also reported.

3.3.1 The Neutral Case

At $z < l_i$, shear production is important, the eddy time scale is smaller than the advection time, L/U, and the flow can be considered in local equilibrium. Observations and numerical simulations show that, in this layer, the increase in $\langle -uw \rangle$ with respect to the upstream value is larger than that in $\langle u^2 \rangle$ or $\langle w^2 \rangle$ (Zeman and Jensen 1987, Figs. 4, 5, and 6 and Ying and Canuto (2007, Figs. 5, 7, and 9)), and. Thus the ratios of the velocity variances to the shear stress should be smaller than over flat terrain.

At $z \simeq l_i$, the inviscid distortion of eddies drives second-order moment profiles, which show a minimum around this height. Considering that $\langle u^2 \rangle / \langle w^2 \rangle \simeq 4$ for the unperturbed upstream flow over flat terrain, the TKE should decrease at this level, but the velocity variances normalized over the local value of the shear stress should increase (Zeman and Jensen, 1987, Eq. 22).

In the lower part of the outer region, $z \gtrsim l_i$—characterized by inviscid perturbation, because the advection time is smaller than the eddy time scale—, the shear stress is reduced more than the velocity variances compared to upstream values, so that the variances normalised over the shear stress are expected to be larger than over flat terrain.

Thus, in neutral conditions, due to the pure topographic effect, $\langle u_i^2 \rangle / \langle -uw \rangle$ increases with height, from values that are smaller than over flat terrain, to values that are larger.

This is in qualitative agreement with the small values of $\langle -uw \rangle_{100\mathrm{s}} / \langle w^2 \rangle_{100\mathrm{s}}$ observed at the CCT station when $R_\tau > 1$ (which likely corresponds to stronger topographic perturbation), and to a measurement level close the height of the inner layer, l_i.

3.3.2 Spectra Modification

In general terms, topography induces/enhances large-scale (low-frequency) components in the spectra. Some spectra are shown by Gallagher et al. (1988) (upstream spectra are lacking).

Frank (1996) presents a spectral model accounting for the modification of large eddies—with amplitude proportional to the square of the mean wind speed—, rapid-distortion modification for intermediate-size eddies; local equilibrium near the surface (inner layer), and curvature effects.

A few spectra from Askervein hilltop are presented by Mann (2000), showing the presence of large amplitudes in the small wavenumber part of the spectrum (their Fig. 9, right panel) .

Spectra in neutral conditions at Inexpressible Island (Antarctica) are presented by Mammarella et al. (2005, their Figs. 13, 14 and 15), normalized over upstream friction velocity. The high-frequency amplitude increases for all the spectra, and a secondary peak appears in the vertical velocity spectrum. In the inertial subrange, the increase is consistent with that in the friction velocity (see their Eq. 11). Near the ground, the spectral peak shifts towards higher wavenumbers because of the increased wind shear that limits the scale.

From the Bolund experiment, Berg et al. (2011, Fig. 6, central panel; Fig. 11) also observe a shift of the spectral peak towards higher frequencies (but using as reference velocity the upstream value, which is smaller than the local one) and a general increase in amplitude with respect to the upstream values (but spectra are normalized with the upstream friction velocity).

Velocity spectra in near-neutral conditions on the hill-top (Black Mountain) are studied by Panofsky et al. (1982) (their Fig. 6)—note that, assuming $\epsilon = \langle -uw \rangle \partial U/\partial z$, spectra are normalized by $(u_* \langle -uw \rangle)^{3/2}$, where $u_* \equiv z\partial U/\partial z$ is the friction velocity from the wind profile and $\langle -uw \rangle$ is the local shear-stress. In terms of hill parameters, spectra on the hill top conform to Kansas spectra (Kaimal et al., 1972, neutral conditions from the unstable side) for wavelength $\lesssim$ the inner-layer thickness; while a low-frequency deficit, corresponding to wavelengths $\gtrsim$ 4 hill length scales, is observed for the stream-wise velocity components. Having most energy in the high-frequency range, vertical velocity spectra over complex terrain resemble those over uniform terrain.

Andreas (1987) observes that spectra and cospectra in the near-neutral and stable surface layer display the expected dependence in the inertial subrange, with the exception of the uw cospectra, and an excess of energy in the low-frequency range compared with neutral Kansas spectra.

Cava et al. (2001) find that the orographic perturbation shifts towards lower frequencies the maximum of the stream-wise velocity spectrum and eliminates the stability dependence of crosswind and vertical velocity spectra.

4 Stable Conditions

Because the magnitude of 100-s fluxes decreases with stability (Fig. 6a,c) while the low-frequency contribution is almost constant (Fig. 6b,d), on average, the relative low-frequency contribution increases with stability (Fig. 7a, Acevedo et al. 2014). Hence, MOST and Reynold's averaging assumptions are expected to be less fulfilled as more stable conditions are approached.

4.1 Choice of the Stability Parameter

Within the MOST framework, the natural stability parameter is z/Λ, where Λ is the local Obukhov length (cf. Eq. 5). However, self-correlation is an important issue when similarity relationships are evaluated using z/Λ as a stability parameter (e.g., Klipp and Mahrt, 2004; Baas et al., 2006; Grachev et al., 2007; Nadeau et al., 2013). It is thus appropriate to consider alternative stability parameters, such as the bulk Richardson number, R_b—the gradient- and the flux-Richardson-number require the wind shear, $\partial U/\partial z$, which is not available at the NYA and BAY stations because wind speed is measured at one level only.

Figure 11 shows the relation between R_b, Eq. 1, and z/Λ_100s, Eq. 5, at the three stations. 100-s fluxes are measured at the height z, the same where the 30-min mean wind is measured. Data are divided according to the relative low-frequency contribution to the shear stress ($R_\tau < 0.3$ and > 1) and to the magnitude of the 100-s shear stress (with threshold $\tau_\mathrm{100s} = 0.01\,\mathrm{m}^2\,\mathrm{s}^{-2}$). Also represented in Fig. 11 are the similarity relationships between R_b and z/Λ_100s obtained by substituting

$$U(z) = \frac{\tau_\mathrm{100s}^{1/2}}{\kappa}\left[\ln\frac{z}{z_0} + \Psi_U\left(\frac{z}{\Lambda_\mathrm{100s}}\right)\right] \tag{6}$$

and

$$\Delta\Theta(z_1, z_2) = -\frac{\langle w\theta\rangle_{100\mathrm{s}}}{\kappa\tau_{100\mathrm{s}}^{1/2}}\left[\ln\frac{z_2}{z_1} + \Psi_\Theta\left(\frac{z_2 - z_1}{\Lambda_{100\mathrm{s}}}\right)\right], \tag{7}$$

in Eq. (1), with $\Psi_U(x) \equiv \Psi_\Theta(x) \equiv 1 + 5x$ as a rough approximation of observed stability functions (Högström, 1996), and for two extreme values of z_0 representative for each station (Fig. S2). The dynamic roughness length, z_0, has been calculated from the log profile

$$U(z) = \frac{\tau_{100\mathrm{s}}^{1/2}}{\kappa}\ln\frac{z}{z_0} \tag{8}$$

using the 30-min mean wind speed, U, and 100-s shear stress, $\tau_{100\mathrm{s}}$, measured at the height z, and selecting only the 30-min records with $|R_\mathrm{b}| < 0.001$, $R_\tau < 0.3$, and $\tau_{100\mathrm{s}} > 0.01\,\mathrm{m}^2\,\mathrm{s}^{-2}$.

When $R_\tau < 0.3$, R_b and $z/\Lambda_{100\mathrm{s}}$ are well correlated (Fig. 11a,c,f), with most of the data laying between the two similarity relationships plotted in Fig. 11. Most of the points with $R_\tau < 0.3$ also correspond to $\tau_{100\mathrm{s}} \gtrsim 10^{-2}\,\mathrm{m}^2\,\mathrm{s}^{-2}$ (i.e., well-developed turbulence), $z/\Lambda_{100\mathrm{s}} \lesssim 1$ (which is approximately the upper limit for which the log-linear profile used in Eqs. (6) and (7) is reliable, e.g., Tampieri 2017), and $R_\mathrm{b} \lesssim 10^{-2}$.

When $R_\tau > 1$, R_b and $z/\Lambda_{100\mathrm{s}}$ are poorly correlated, especially for $R_\mathrm{b} \gtrsim 10^{-2}$ (Fig. 11b,d,f). The correlation is even worse if $z/\Lambda_{30\mathrm{min}}$ is considered (not shown) because of the non-gradient submeso contribution to the 30-min fluxes (Fig. 5). Most of the data points with $R_\tau > 1$ corresponds to $R_\mathrm{b} \gtrsim 10^{-2}$ and $\tau_{100\mathrm{s}} \lesssim 10^{-2}\,\mathrm{m}^2\,\mathrm{s}^{-2}$, which turns out to be critical conditions for MOST.

The drawback of using R_b as a stability parameter is that it is not universal, because it depends on z_1 and z_2 (through the temperature difference), and on z_0, through the wind speed. From this point of view, the gradient Richardson number,

$$Ri \equiv \frac{\beta\partial\Theta/\partial z}{(\partial U/\partial z)^2}, \tag{9}$$

or the flux Richardson number

$$(R_\mathrm{f})_{100\mathrm{s}} \equiv \frac{\beta\langle w\theta\rangle_{100\mathrm{s}}}{\langle uw\rangle_{100\mathrm{s}}\partial U/\partial z} \tag{10}$$

are preferable. For instance, Ri is the stability parameter used in Sorbjan's gradient-based similarity theory (Sorbjan, 2010; Sorbjan and Grachev, 2010). However, in practice, many authors use R_b instead of Ri: beside the fact that gradients can be unavailable or difficult to determine—because of complex shapes of velocity and temperature profiles—, observations seems to organize better when R_b is considered. This is consistent with $R_\mathrm{b} \propto U^{-2}$ and the key role of U in determining turbulence behaviour (Sun et al., 2012, 2016; Van de Wiel et al., 2012b; Mahrt et al., 2013, 2015; Acevedo et al., 2016; Schiavon et al., 2019).

Figure 12 shows the relation between R_b and the other two stability parameters, Ri and $(R_\mathrm{f})_{100\mathrm{s}}$, at the CCT station, where vertical gradients of wind speed are available. As in Fig. 11, data are classified according to R_τ and $\tau_{100\mathrm{s}}$. For $R_\tau < 0.3$ (Fig. 12a,c), R_b is well correlated with both Ri and $(R_\mathrm{f})_{100\mathrm{s}}$: $R_\mathrm{b} \approx 0.05Ri^{1.5}$ (an empirical relationship obtained fitting "by eye" the data);

$R_\mathrm{b} \approx 10^{-2}$ corresponds to $Ri \approx (R_\mathrm{f})_{100\mathrm{s}} \approx 0.2$–$0.3$, which are the values that identifies critical conditions for MOST applicability and collapse of Kolmogorov (Kolmogorov, 1941) "$-5/3$" power law in the inertial subrange (Grachev et al., 2013) . For $R_\tau > 1$ (Fig. 12b,d), the correlation between Ri and R_b is poorer, especially for increasing Ri (R_b), while R_b and $(R_\mathrm{f})_{100\mathrm{s}}$ are uncorrelated over the whole stability range. The tail observed in Fig. 12c for $(R_\mathrm{f})_{100\mathrm{s}} \to 0$, similar to that in Fig. 11e for $z/\Lambda_{100\mathrm{s}} \to 0$, is likely due to the poor correlation between the heat flux and the temperature gradient as neutral conditions are approached.

Because plots of $\tau_{100\mathrm{s}}/\langle w^2\rangle_{100\mathrm{s}}$ vs $z/\Lambda_{100\mathrm{s}}$ are affected by self-correlation, and because U is available only at one level at the NYA and BAY stations, R_b is considered as a stability parameter.

4.2 The Stability Dependence of $\tau/\langle w^2\rangle$

Both models and observations give different indications about the stability dependence of $\tau/\langle w^2\rangle$. According to the z-less paradigm, eddies become detached from the ground as very stable conditions are approached. Based on second-order moment budget equations, Nieuwstadt (1984b) and Zilitinkevich et al. (2013) both account for the z-less regime, but with different results: according to Nieuwstadt (1984b), $\tau/\langle w^2\rangle \approx 0.5$, independently of stability (see N84 in Fig. S3); according to Zilitinkevich et al. (2013, their Eqs. 50c and 60), $\tau/\langle w^2\rangle$ increses with stability, from ≈ 0.7 in the neutral limit to ≈ 2 in the z-less regime, which is approached for $z/\Lambda \approx 10$ (see Z13 in Fig. S3), $Ri \approx 1$. Experiments confirm that $\tau/\langle w^2\rangle \approx$ constant up to moderate stabilities (i.e., $z/\Lambda \approx 1$, $Ri \approx 0.1$) but disagree for larger stability, either supporting $\tau/\langle w^2\rangle \approx$ constant (Stiperski et al., 2019, up to $z/\Lambda \approx 100$) or $\tau/\langle w^2\rangle$ decreasing with z/Λ (de Franceschi et al., 2009; Acevedo et al., 2014) and Ri (Sorbjan, 2010; Sorbjan and Grachev, 2010). To further complicate the picure, is that the observed behaviour may depend on data processing and selection, as the choice of the averaging time and the application of stationarity tests (Basu et al., 2006; Stiperski et al., 2019). The fact that very-stable conditions do not correspond, generally, to well-developed turbulence (Van de Wiel et al., 2012b; Grachev et al., 2013) limits the validity of concepts that underlie turbulence-closure models such as MOST.

Figure 13 shows the stability dependence of $\tau_T/\langle w^2\rangle_T$ and $\langle -uw\rangle_T/\langle w^2\rangle_T$ at the three stations, for $T = 100\,\mathrm{s}$ and 30 min, $R_\tau < 0.3$ and > 1. R_b is considered as stability parameter, because plots of $\tau_T/\langle w^2\rangle_T$ vs z/Λ_T are affected by self correlation (plots as those in Fig. 13, but with z/Λ_T as stability parameter, are shown in the Supplementary Material, Fig. S3). The drawback of this choice is that R_b is not a universal parameter. Hence, the observed stability dependence can be compared only approximately among the three stations and no similarity relationships exist from the literature.

We recall that, at least for $R_\mathrm{b} \lesssim 10^{-2}$, the relative low-frequency contribution to the vertical velocity variance is negligible, i.e., $R_{ww} \ll 1$ (Fig. 8a). Hence, the low-frequency contribution affect the shear stress, while leaving almost unaffected $\langle w^2\rangle$.

When $R_\tau < 0.3$, $\tau_{100\mathrm{s}} \approx \tau_{30\mathrm{min}}$ and, at least up to $R_\mathrm{b} \approx 10^{-2}$ ($\tau_{100\mathrm{s}} \approx 10^{-2}\,\mathrm{m}^2\,\mathrm{s}^{-2}$, Fig. 6a), the shear stress is aligned with the 30-min mean wind, i.e., $\tau_{100\mathrm{s}} \approx \langle -uw\rangle_{100\mathrm{s}}$ (Fig. S4a,c,e) and $\tau_{30\mathrm{min}} \approx \langle -uw\rangle_{30\mathrm{min}}$ (Fig. S5a,c,e).

(a) R_τ<0.3 (b) R_τ>1

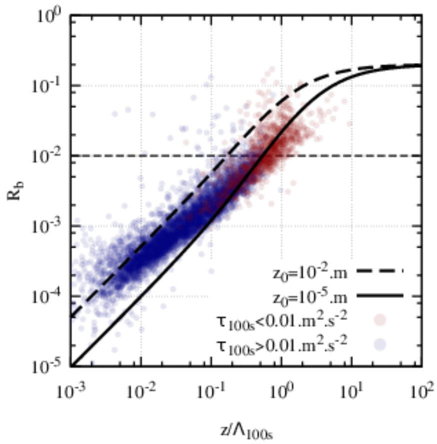

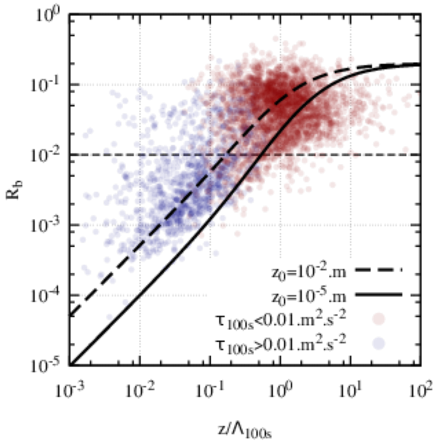

(c) BAY R_τ<0.3 (d) BAY R_τ>1

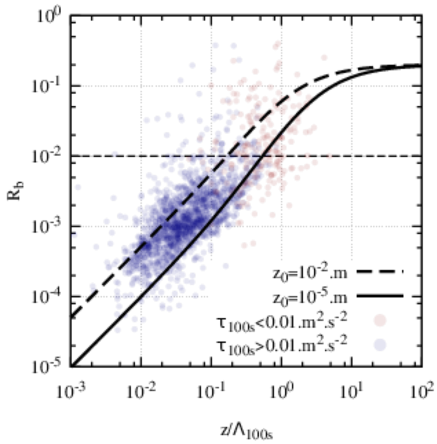

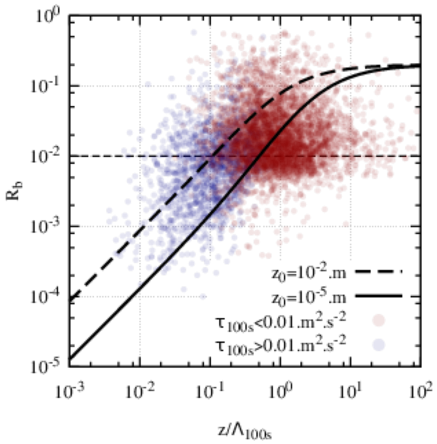

(e) CCT 7.5m R_τ<0.3 (f) CCT 7.5m R_τ>1

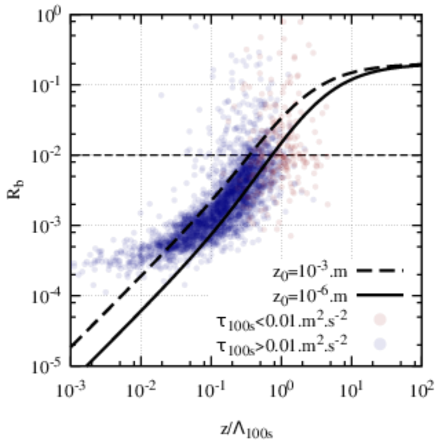

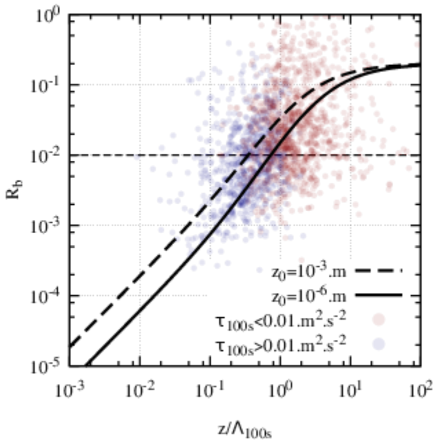

Figure 11: R_b vs $z/\Lambda_{100\mathrm{s}}$ at the three stations, for $R_\tau < 0.3$ and > 1: each point corresponds to a 30-min record. Blue and red points correspond to $\tau_{100\mathrm{s}}$ larger and smaller than $0.01\,\mathrm{m}^2\,\mathrm{s}^{-2}$, respectively. The similarity relationship obtained from Eqs. (6) and (7), for two extreme values of dynamic roughness length representative of each station, is also shown. The critical value $R_\mathrm{b} = 10^{-2}$ is also reported. CCT data refer to $z = 7.5\,\mathrm{m}$.

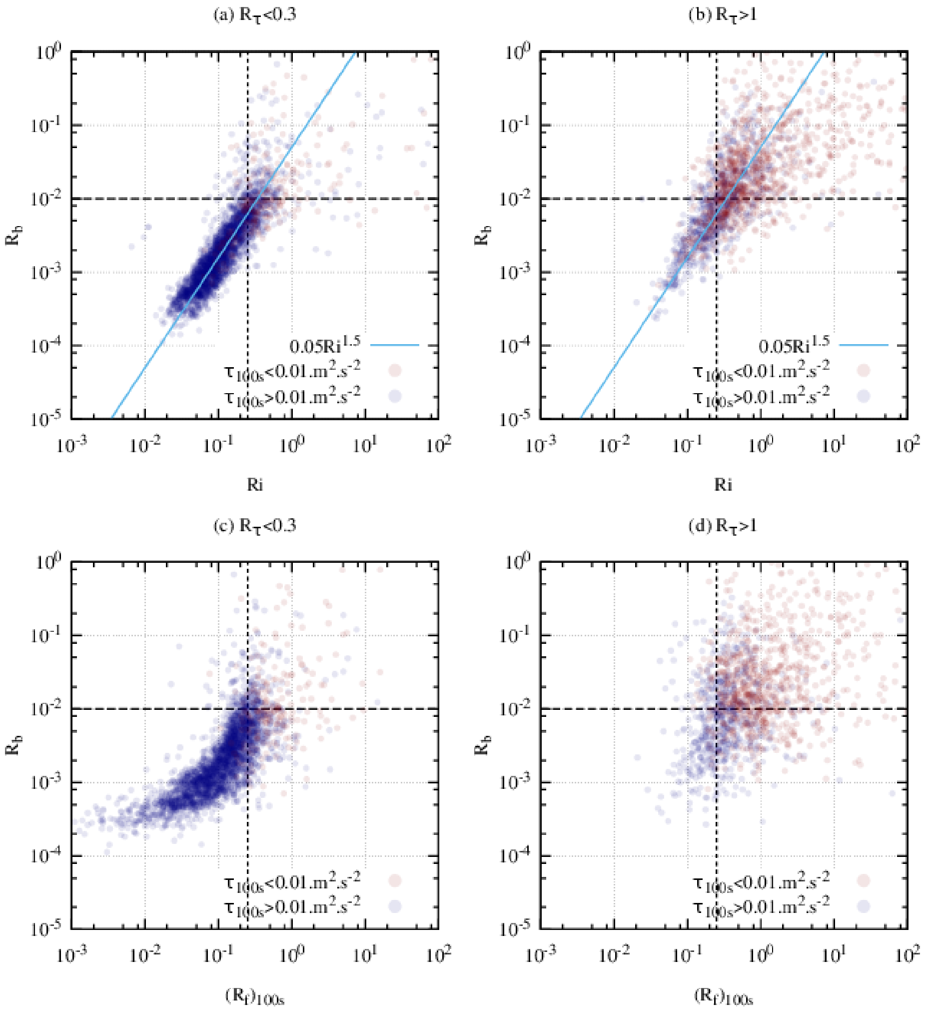

Figure 12: R_{b} vs Ri and $(R_{\mathrm{f}})_{100\mathrm{s}}$ at the CCT station ($z = 7.5\,\mathrm{m}$) for $R_\tau < 0.3$ and > 1; blue and red points refer, respectively, to $\tau_{100\mathrm{s}}$ larger and smaller than $0.01\,\mathrm{m}^2\,\mathrm{s}^{-2}$; data are the same of Figs. 11e and f. The "critical" values $R_{\mathrm{b}} = 10^{-2}$, $Ri = (R_{\mathrm{f}})_{100\mathrm{s}} = 0.25$ are also indicated, along with the empirical relationship $R_{\mathrm{b}} = 0.05Ri^{1.5}$.

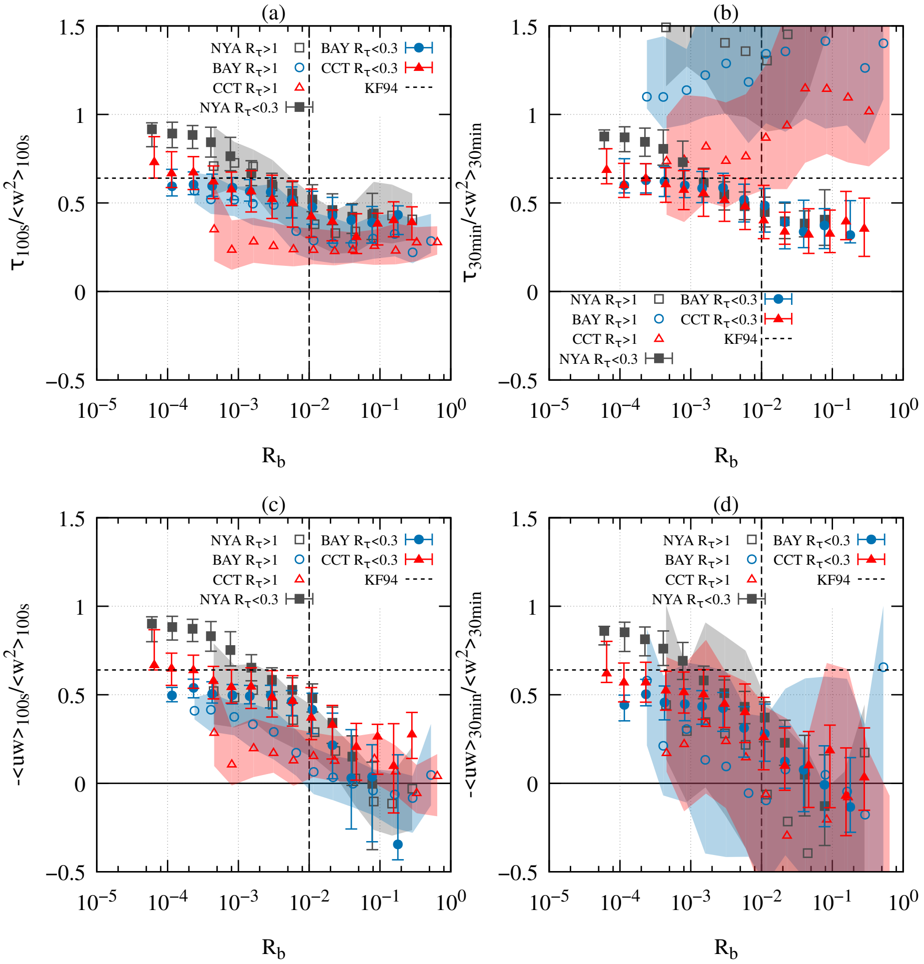

Figure 13: Dependence of $\tau_T/\langle w^2\rangle_T$ and $\langle -uw\rangle_T/\langle w^2\rangle_T$ on R_b, for $T = 100\,\mathrm{s}$ and 30 min, and $R_\tau < 0.3$ (filled symbols and errorbars) and > 1 (open symbols and shaded areas). Data are binned in R_b: median values and 25th-75th percentile range are shown for each station. The neutral limit of Kaimal and Finnigan (1994, KF94) similarity relationship and the value $R_\mathrm{b} = 10^{-2}$ are also indicated.

Thus, for $R_\tau < 0.3$ (points and errorbars in Fig. 10) and $R_\mathrm{b} \lesssim 10^{-2}$, the flux-variance relationship is the same for $T = 100\,\mathrm{s}$ and 30 min, and whether the modulus of the shear-stress or only its stream-wise component is considered: on average, $\tau_T/\langle w^2\rangle_T$ ($\langle -uw\rangle_T/\langle w^2\rangle_T$) decreases from ≈ 0.6–0.8 in near-neutral conditions (depending on the station) to ≈ 0.4–0.5, where the largest variation occurs at the NYA station. For $R_\mathrm{b} \gtrsim 10^{-2}$, $\tau_T/\langle w^2\rangle_T$ levels off (Fig. 10a,b; points and errorbars), while $\langle -uw\rangle_T/\langle w^2\rangle_T$ continues to decrease (Fig. 10c,d; points and errorbars), on average. This indicates that $\tau_T \neq \langle -uw\rangle_T$ for $R_\mathrm{b} \gtrsim 10^{-2}$ (confirmed by Fig. S4 and S5, for $\tau_{100\mathrm{s}} \lesssim 10^{-2}\,\mathrm{m}^2\,\mathrm{s}^{-2}$) and—as it will be discussed in Sect. 4.3— can be explained through a residual (negative) submeso contribution to $\langle -uw\rangle$, even if 100-s covariances are considered.

When $R_\tau > 1$, the shear stress depends on the averaging time and is generally not aligned with the 30-min mean wind, i.e., $\tau_T \neq \langle -uw\rangle_T$, especially for $R_\mathrm{b} \gtrsim 10^{-2}$ and $T = 30\,\mathrm{min}$ (Fig. S4 and S5, plots b,d,f). Because of the submeso contribution to the shear stress, whose relative magnitude increases, on average, with R_b (Fig. 7a), $\tau_{30\mathrm{min}}/\langle w^2\rangle_{30\mathrm{min}}$ increases with R_b (open symbols with shaded areas in Fig. 13b), while $\langle -uw\rangle_{30\mathrm{min}}/\langle w^2\rangle_{30\mathrm{min}}$ decreases, becoming negative for $R_\mathrm{b} \gtrsim 10^{-2}$: this is because the submeso contribution to $\langle -uw\rangle$ turns out to be negative at all stations (Sect. 4.3) and thus diminishes the positive contribution due to small-scale turbulence; while τ increases because the submeso contribution to $\langle vw\rangle$ overwhelms the former effect. When 30-min averages are considered, the scatter of the data increases for $R_\tau > 1$ (Fig. 13b,d), indicating a weaker relation between the 30-min shear stress and the vertical velocity variance. $\tau_{100\mathrm{s}}/\langle w^2\rangle_{100\mathrm{s}}$ and $\langle -uw\rangle_{100\mathrm{s}}/\langle w^2\rangle_{100\mathrm{s}}$ for $R_\tau > 1$ are smaller than for $R_\tau < 0.3$ (Fig. 13a,c). The characteristic behaviour observed at the CCT station in the near-neutral case (Sect. 3.2) is confirmed for stable conditions: $\tau_{100\mathrm{s}}/\langle w^2\rangle_{100\mathrm{s}} \approx 0.3$ when $R_\tau > 1$, independently of R_b, suggesting a strong topographic effect that dominates on stability (Sect. 3.3).

At the NYA station, stability is correlated with wind direction, generally increasing as wind turns from north-east to south-east. Hence, it is difficult to disentangle the stability dependence from that on wind direction (Fig. 9a), and this may play a role in the particularly large variation in $\tau_{100\mathrm{s}}/\langle w^2\rangle_{100\mathrm{s}}$ observed at this station. A similar but less pronounced effect is observed also at the other stations.

A stronger stability dependence is found when z/Λ is used as stability parameter (Fig. S3a,b), with $\tau_{100\mathrm{s}}/\langle w^2\rangle_{100\mathrm{s}}$ that decreases also for $z/\Lambda_{100\mathrm{s}} \gtrsim 1$ (roughly corresponding to $R_\mathrm{b} \gtrsim 10^{-2}$, Fig. 11) reaching values close to zero (Fig. S3). This decrease is due to self-correlation—because $z/\Lambda_{100\mathrm{s}}$ is driven by $\tau_{100\mathrm{s}}$—and by the weak dependence of the 100-s shear stress on the vertical velocity variance for small values of $\tau_{100\mathrm{s}}$. This is well demonstrated by Fig 14, which shows $\tau_{100\mathrm{s}}$ vs $\langle w^2\rangle_{100\mathrm{s}}$ for all the data points used to produce Fig. 13a, with the only distinction between R_b smaller and larger than 10^{-2}. When $R_\tau < 0.3$ (which corresponds mostly to $R_\mathrm{b} \lesssim 10^{-2}$ and $\tau_{100\mathrm{s}} \gtrsim 10^{-2}\,\mathrm{m}^2\,\mathrm{s}^{-2}$), the vertical velocity variance and the 100-s shear stress are well correlated: at the BAY and CCT stations (Fig. 14c,d), $\tau_{100\mathrm{s}}/\langle w^2\rangle_{100\mathrm{s}} \approx \text{constant} \approx 0.65$ (i.e., Kaimal and Finnigan 1994 neutral value) in first approximation; while a larger variation is observed at the NYA station. When $R_\tau > 1$, the correlation between $\tau_{100\mathrm{s}}$ and $\langle w^2\rangle_{100\mathrm{s}}$ is poor, especially for small $\tau_{100\mathrm{s}}$: this is particularly evident at the BAY station (Fig. 14d), for the cloud of points corresponding to $\tau_{100\mathrm{s}} \lesssim 10^{-2}\,\mathrm{m}^2\,\mathrm{s}^{-2}$: when data are ordered according to $\tau_{100\mathrm{s}}$ (as roughly occurs when $z/\Lambda_{100\mathrm{s}}$ is used as a stability parameter), $\tau_{100\mathrm{s}}/\langle w^2\rangle_{100\mathrm{s}}$ decreases for decreasing $\tau_{100\mathrm{s}}$ because of self-correlation. Furthermore, Fig. 14f confirms the characteristic behaviour observed at the CCT station, where the correlation is poor and data are below Kaimal and Finnigan (1994) neutral value independently of $\tau_{100\mathrm{s}}$ (or R_b).

4.3 Submeso Contribution to $\tau_{100\mathrm{s}}$

The physical significance of 100-s covariances—taken as representative of small-scale turbulence—depends on the existence of a spectral gap and, in this case, on its time scale compared with $T = 100\,\mathrm{s}$. Figure 15 shows MRD integrated cospectra of $-uw$, equivalent to $\langle -uw\rangle_T$, normalized by $\langle w^2\rangle_{100\mathrm{s}}$, for $R_\tau < 0.3$ and > 1, and different intervals of $\log_{10}(\tau_{100\mathrm{s}})$: $\tau_{100\mathrm{s}} \approx 10^{-2}\,\mathrm{m}^2\,\mathrm{s}^{-2}$ corresponds to the yellow lines. A gap in the cospectrum corresponds to a stationary point in the integrated cospectrum, i.e., a region where the (co)variance depends weakly on the averaging time. In Fig. 15, stationary points are maxima.

For $R_\tau < 0.3$ (Fig. 15a,c,e) a wide gap exists in $-uw$ cospectra for $T \gtrsim 100\,\mathrm{s}$, and hence $\langle -uw\rangle_T$ converges for any $T \gtrsim 100\,\mathrm{s}$, at least if $\tau_{100\mathrm{s}} \gtrsim 10^{-2}\,\mathrm{m}^2\,\mathrm{s}^{-2}$; for $\tau_{100\mathrm{s}} \lesssim 10^{-2}\,\mathrm{m}^2\,\mathrm{s}^{-2}$ the gap is narrower and the flat region in integrated cospectra becomes a maximum after which $\langle -uw\rangle_T/\langle w^2\rangle_{100\mathrm{s}}$ decreases with T (indicating a negative submeso contribution to $\langle -uw\rangle$).

When $R_\tau > 1$ (Fig. 15b,d,f), the cospectral gap is narrow, corresponding to the maximum in $\langle -uw\rangle_T/\langle w^2\rangle_{100\mathrm{s}}$. After this maximum, $\langle -uw\rangle_T$ decreases, on average, at all stations, indicating a negative submeso contribution to $\langle -uw\rangle$. The time scale of the maximum (i.e., of the cospectral gap) shifts towards shorter times as $\tau_{100\mathrm{s}}$ decreases (Fig. 15b,d,f), eventually becoming $\lesssim 100\,\mathrm{s}$ as $\tau_{100\mathrm{s}} \lesssim 10^{-2}\,\mathrm{m}^2\,\mathrm{s}^{-2}$. Thus, $\langle -uw\rangle_{100\mathrm{s}}$ (and hence $\tau_{100\mathrm{s}}$) likely contains a (negative) residual submeso contribution when $R_\tau \gtrsim 1$ and $\tau_{100\mathrm{s}} \lesssim 10^{-2}\,\mathrm{m}^2\,\mathrm{s}^{-2}$. The fact that the time scale of the maximum (the gap) is $\gtrsim 100\,\mathrm{s}$ for $\tau_{100\mathrm{s}} \gtrsim 10^{-2}\,\mathrm{m}^2\,\mathrm{s}^{-2}$ (Fig. 15b,d,f) does not guarantee that, in this case, 100-s fluxes are free from any submeso contribution. Indeed, when $R_\tau \gtrsim 1$, a wide separation of submeso motions and small-scale turbulence never occurs: the narrow spectral gap may not correspond to a real separation, but only to the time scale where the positive and negative contributions due to small-scale turbulence and submeso motions, respectively, sum to zero.

A systematic submeso contribution affects also $\langle vw\rangle$, with positive or negative sign depending on the station (Fig. S6b,d,f): as occurs for the negative contribution to $\langle -uw\rangle$ (Fig. 15b,d,f), the magnitude of the submeso contribution to $\langle vw\rangle$ normalized by $\langle w^2\rangle_{100\mathrm{s}}$ is particularly large at the NYA and BAY stations. Concerning the magnitude of the shear stress, when $R_\tau > 1$, τ_T increases monotonically with T when the submeso contribution to $\langle vw\rangle$ overwhelms the decreasing trend due to the negative submeso contribution to $\langle -uw\rangle$ (Fig. S7b,d,f). But τ_T may also decrease around $T = 100\,\mathrm{s}$ if the trend due to the negative submeso contribution to $\langle -uw\rangle$ dominates (minimum in $\tau_T/\langle w^2\rangle_{100\mathrm{s}}$ around $T = 100\,\mathrm{s}$ in Fig. S7b,d,f).

Figure 15 confirms the down-gradient nature of the small-scale momentum flux (i.e., gradient production, $-\langle w^2\rangle\partial U/\partial z$, with $\langle w^2\rangle$ dominated by small scales, is the primary source of small-scale turbulence) and the non-gradient origin of the submeso contribution. Beside pressure-redistribution, the non-gradient term in the simplified budget equation for $\langle uw\rangle$ is the buoyancy term,

(a) NYA R_τ<0.3 (b) NYA R_τ>1

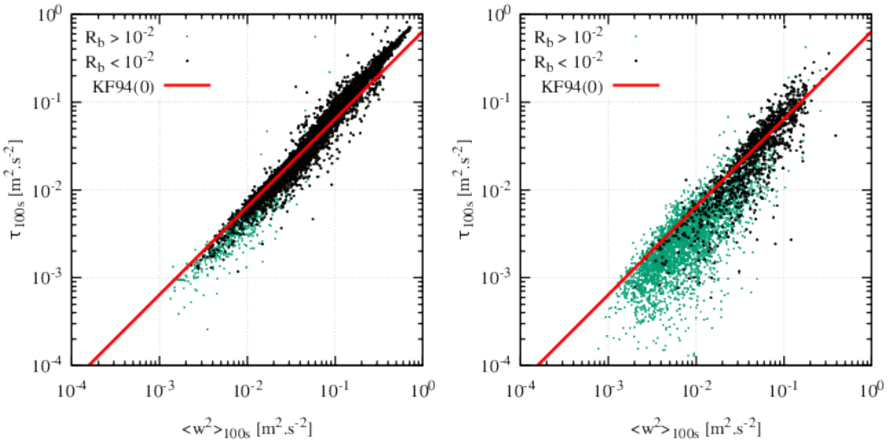

(c) BAY R_τ<0.3 (d) BAY R_τ>1

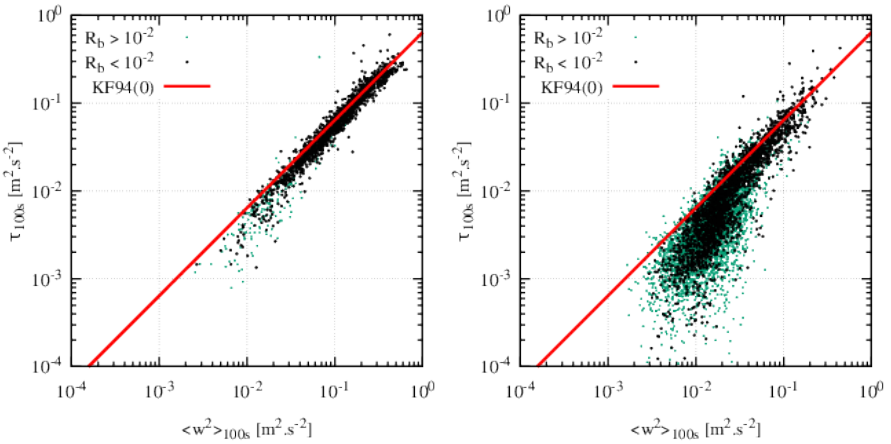

(e) CCT R_τ<0.3 (f) CCT R_τ>1

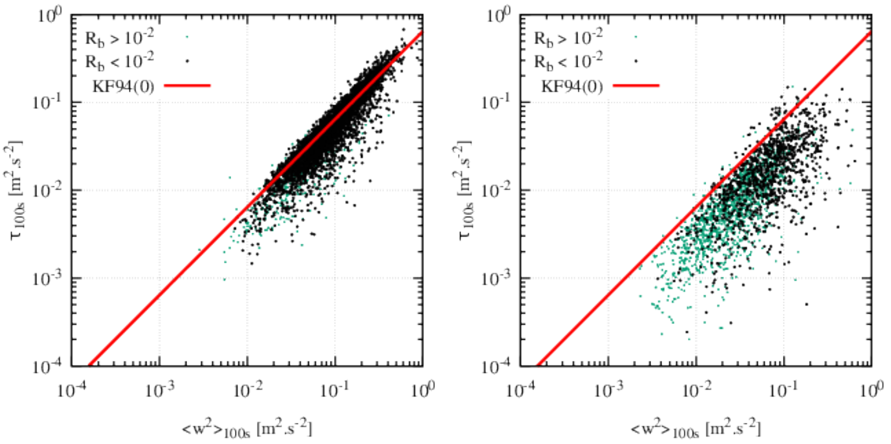

Figure 14: $\tau_{100\mathrm{s}}$ vs $\langle w^2\rangle_{100\mathrm{s}}$ for $R_\tau < 0.3$ (left) and > 1 (right). Each point corresponds to a 30-min record: black and green for R_b below and above 0.01, respectively. The neutral limit of Kaimal and Finnigan (1994, KF94) similarity relationship is also indicated (red line).

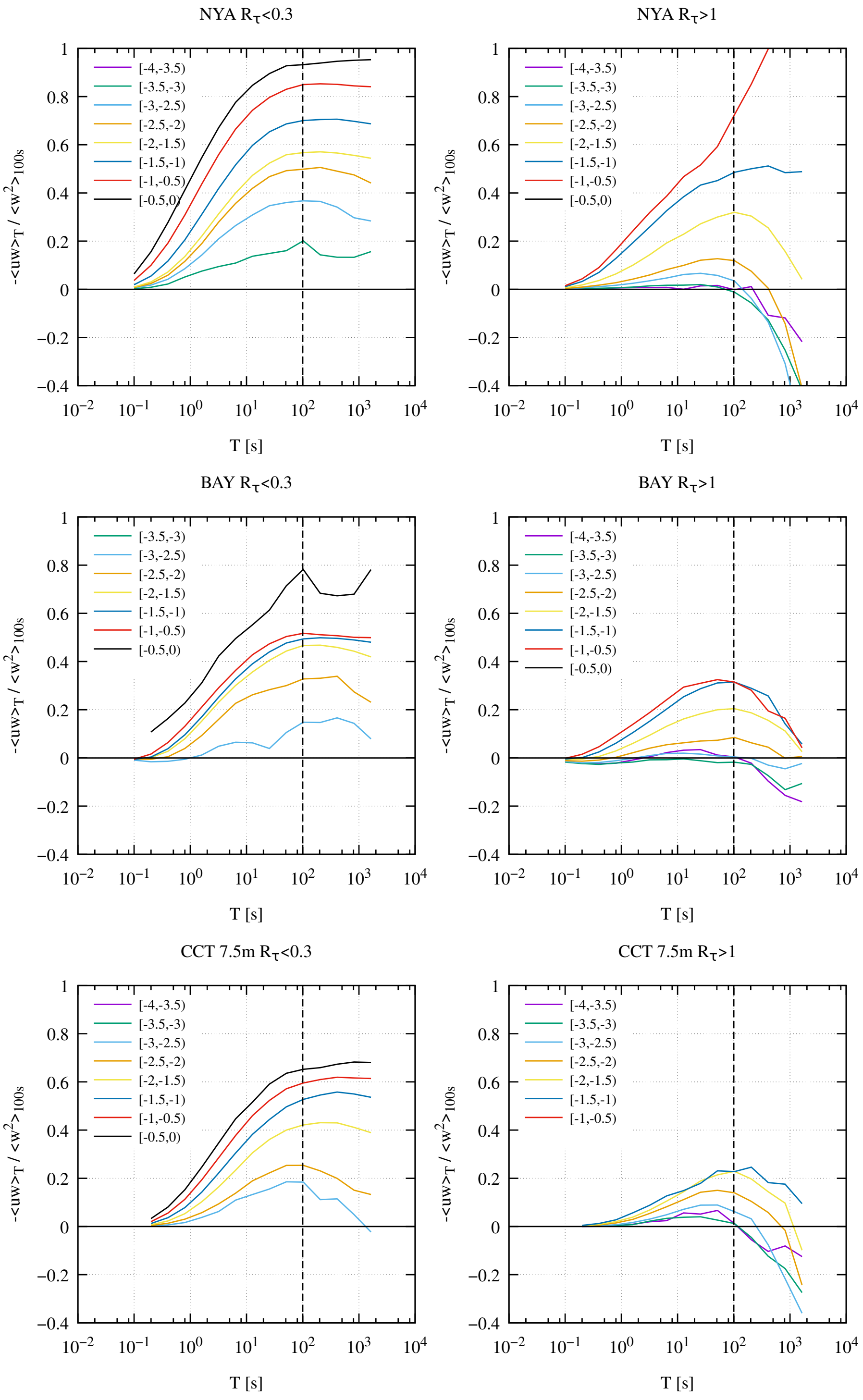

Figure 15: $\langle -uw \rangle_T / \langle w^2 \rangle$ vs T (from MRD integrated cospectra) for different intervals of $\log_{10}(\tau_{100\mathrm{s}})$, $R_\tau < 0.3$ and > 1. Curves refer to median cospectra in each $\log_{10}(\tau_{100\mathrm{s}})$ interval ($\log_{10}(\tau_{100\mathrm{s}})$ increases from purple to black). $T = 100\,\mathrm{s}$ is also indicated. CCT data refer to $z = 7.5\,\mathrm{m}$.

$\beta\langle u\theta\rangle$. Hence, the question raises whether the submeso contribution to the horizontal heat flux, $\langle u\theta\rangle$ ($\langle v\theta\rangle$), is consistent with the submeso contribution to the vertical momentum flux, $\langle uw\rangle$ ($\langle vw\rangle$). Figure 16 is analogous to Fig. 15, but for $-\langle u\theta\rangle_T$ normalized by $z\beta/\langle w^2\rangle_{100\mathrm{s}}^{3/2}$: the minus sign is to compare Fig. 16 with Fig. 15. Generally, $-\langle u\theta\rangle$ is negative both for small and large scales, and its magnitude increases with the averaging time also for $T > 100\,\mathrm{s}$: negative $\langle u\theta\rangle$ is expected in the SBL, at least for small-scale turbulence (Tampieri, 2017) and the contribution for large T is because both u and θ are dominated by low-frequency fluctuations (Fig. 4b,d,f). The negative submeso contribution to $-\langle u\theta\rangle$ and its increasing relative magnitude for decreasing $\log_{10}(\tau_{100\mathrm{s}})$ (Fig. 16b,d,f) are qualitatively consistent with the negative submeso contribution to $\langle -uw\rangle$ (with some exceptions, such as NYA, $R_\tau > 1$, $-4 \leq \log_{10}(\tau_{100\mathrm{s}}) < 3$, Fig. 16b). The submeso contribution to $\langle v\theta\rangle$ is even more systematic (Fig. S8) and, as it occurs for the stream-wise component, has the same sign of the submeso contribution to $\langle vw\rangle$ (Fig. S6).

Gravity waves irradiating from the top of the considered layer, which is likely, close to the ground (i.e., at $z \approx 1$–$10\,\mathrm{m}$), may also be responsible for a negative low-frequency contribution to $\langle -uw\rangle$ (Sect. 6.4.3). $R_\tau > 1$ indicates significant submeso effect, while small shear stress is related to weak or calm wind, i.e., conditions that favour the presence of gravity waves.

4.4 Dependence on the Averaging Time

Considered that, when $R_\tau > 1$, 100-s averages likely contain a residual submeso contribution (Fig. 15b,d,f), a shorter averaging time could be more appropriate in this case, especially as the strength of small-scale turbulence decreases (i.e., as $\tau_{100\mathrm{s}}$ decreases, R_b increases).

Figure 17 shows the ratio between τ_T ($\langle -uw\rangle_T$) and $\langle w^2\rangle_T$ vs the averaging time, T, for different intervals of R_b. As expected, $\tau_T/\langle w^2\rangle_T$ ($\langle -uw\rangle_T/\langle w^2\rangle_T$) increases with T in the high-frequency range because, as the (time) scale increases, eddies become less isotropic and more efficient in transporting momentum. Similar considerations are valid when $\tau_T/\langle w^2\rangle_T$ ($\langle -uw\rangle_T/\langle w^2\rangle_T$) is plotted vs TU/z, except that this improves self-similarity in the small-scale range (Fig. S9).

When $R_\tau > 1$ (Fig. 17b,d), the increase in $\tau_T/\langle w^2\rangle_T$ (decrease in $\langle -uw\rangle_T/\langle w^2\rangle_T$) continues also for $T > 100\,\mathrm{s}$, because of the positive (negative) submeso contribution to τ_T ($\langle -uw\rangle_T$). The maximum in $\langle -uw\rangle_T/\langle w^2\rangle_T$ occurs, generally, at time scales $< 100\,\mathrm{s}$ (Fig. 17d), but its value is close to $\langle -uw\rangle_{100\mathrm{s}}/\langle w^2\rangle_{100\mathrm{s}}$. At all stations and for each R_b interval, $\langle -uw\rangle/\langle w^2\rangle$ is smaller for $R_\tau > 1$ than for $R < 0.3$ even if the maximum value in Fig. 17d is considered. Especially at the NYA and BAY stations, there are no stationary points in $\tau_T/\langle w^2\rangle_T$ (Fig. 17b): $\tau_T/\langle w^2\rangle_T$ for T corresponding to the maximum in $\langle -uw\rangle_T/\langle w^2\rangle_T$ is $< \tau_{100\mathrm{s}}/\langle w^2\rangle_{100\mathrm{s}}$. Hence, although 100 s may not be the ideal averaging time when $R_\tau > 1$, results do not change significantly if shorter averaging times are considered. This demonstrates that the effect due to the averaging time is secondary and alternative explanations must be searched for the decrease in $\tau_{100\mathrm{s}}/\langle w^2\rangle_{100\mathrm{s}}$ and $\langle -uw\rangle_{100\mathrm{s}}/\langle w^2\rangle_{100\mathrm{s}}$, as R_τ increases. For instance:

- it is not possible to separate small-scale turbulence and submeso motions (intended as two phenomena with different origin and driving mechanism):

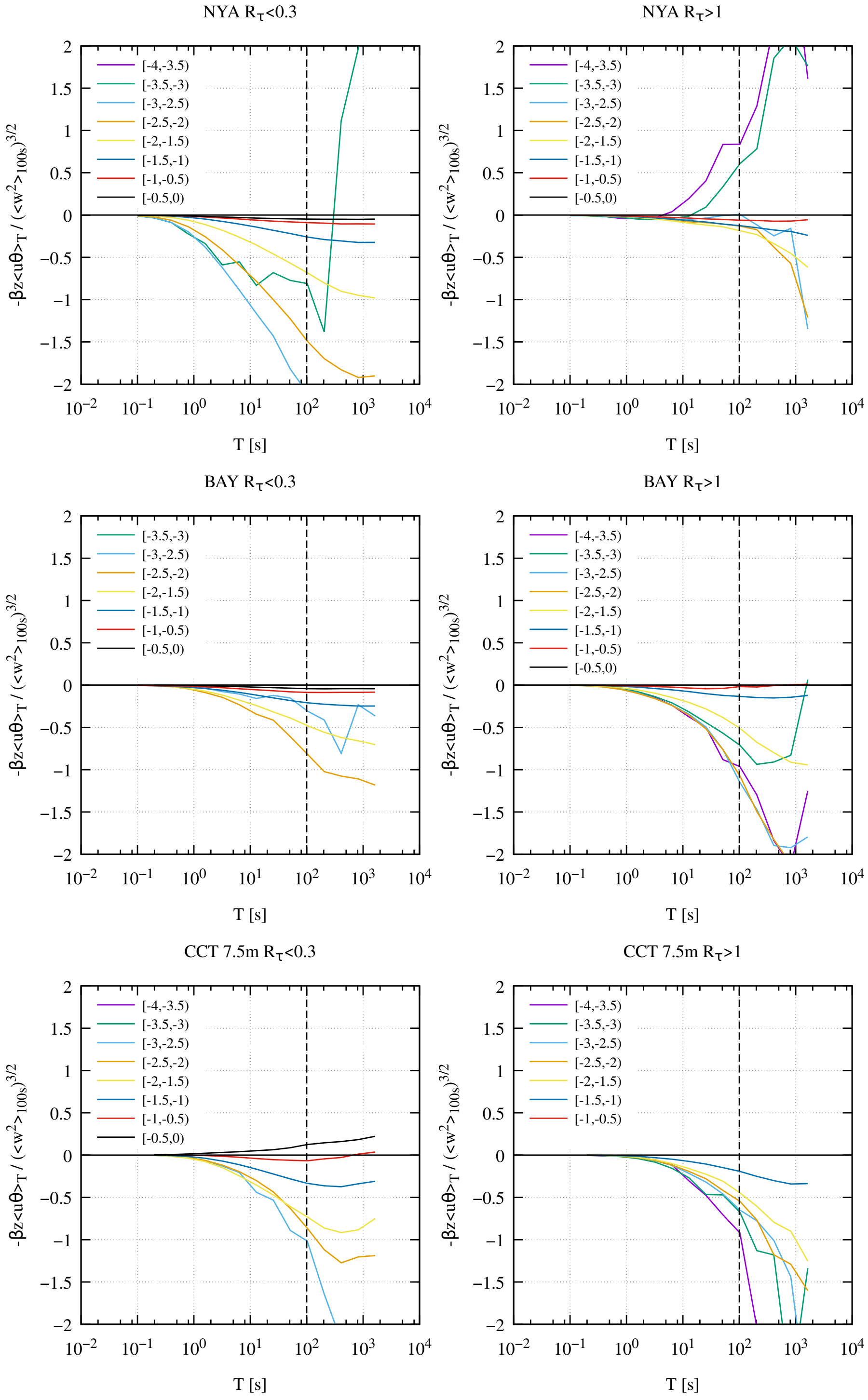

Figure 16: As in Fig. 15, but for (minus) the stream-wise heat flux, $-\langle u\theta\rangle_T$, multiplied by $z\beta(\langle w^2\rangle_{100\mathrm{s}})^{-3/2}$.

the spectral gap observed in Fig. 15b,d,f (i.e., the scale where the contribution to $\langle uw \rangle$ is ≈ 0) is not a true separation between small-scale turbulence and submeso motions, but only the scale where the two opposite contributions balance. In this case, the high-frequency tail of the submeso contribution erodes the positive small-scale contribution also for time scales $\ll$ the "gap" time scale.

- Even if the separation is possible, additional terms must be retained in small-scale turbulence second-order moment budget equations because of the interaction of small-scale turbulence and submeso motions (Sect. 6.4): thus $\langle uw \rangle / \langle w^2 \rangle$ for small-scale turbulence ($\approx \langle uw \rangle_{100\mathrm{s}} / \langle w^2 \rangle_{100\mathrm{s}}$) changes.

4.5 The Length Scale of Small-Scale Turbulence

The spectral distribution of the vertical velocity variance is self-similar and weakly affected by the submeso contribution: spectra collapse on the same curve when normalized by $\langle w^2 \rangle_{100\mathrm{s}}$ and plotted vs TU/z (Fig. S10). The stability effect is small and small differences occur for both small and large R_τ: when $R_\tau > 1$, w^2 spectra show more energy at the large-scale end (Fig. S10b,d,f).

Since it is always dominated by high-frequencies, $\langle w^2 \rangle_T^{1/2}$—with $T \approx 100\,\mathrm{s}$ or longer— can be considered as the velocity scale for small-scale turbulence; while the turbulent length scale may be related to the peak length scale of the w^2 spectra. For steady, homogeneous turbulence over flat terrain, this length scale is expected to be $\sim z$ for near-neutral conditions and to shift towards smaller values as stability increases, eventually becoming independent of z (z-less paradigm) for very stable conditions (Kaimal and Finnigan, 1994).

Figure 18 shows the observed stability dependence of the peak length scale of vertical velocity spectra, λ_m, obtained from the peak time scale of MRD w^2 spectra, T_m, as $\lambda_\mathrm{m} \equiv T_\mathrm{m} U$—i.e., adopting Taylor's frozen-turbulence hypothesis (e.g., Stull, 1988) to switch from time to length scales. 30-min records with very small T_m (i.e., $T_\mathrm{m} < 0.2\,\mathrm{s}$) were discarded because of unphysical origin: spectra dominated by high-frequency noise. Records with very large T_m (i.e.,$T_\mathrm{m} > 400\,\mathrm{s}$) are also excluded from the analysis, being not representative of small-scale turbulence: these cases, occurring mainly when $R_\tau > 1$, are shown as red points in Fig. 18 and are likely related to gravity waves.

At all stations, $\lambda_\mathrm{m}/z \approx 2$ independently of R_b and R_τ (Fig. 18), and close to the neutral value found over flat terrain (Kaimal and Finnigan, 1994)—the estimation of λ_m is sensitive to the spectral technique (cf. Howell and Mahrt, 1997): if Fourier spectra are considered, the same behaviour of Fig. 18 is found but $\lambda_\mathrm{m}/z \approx 3$ (not shown). The stability independence of λ_m, observed also by Cava et al. (2001) on complex terrain, suggests that other (dynamical) effects dominate on stability. Such effects may be of topographic origin (Sect. 3.3) or, for instance, related to the interaction between small-scale turbulence and submeso motions (such as gravity waves, Sect. 6.4). More stable conditions correspond, on average, to larger R_τ (Figs. 18,S11 and 7), i.e., stronger submeso activity.

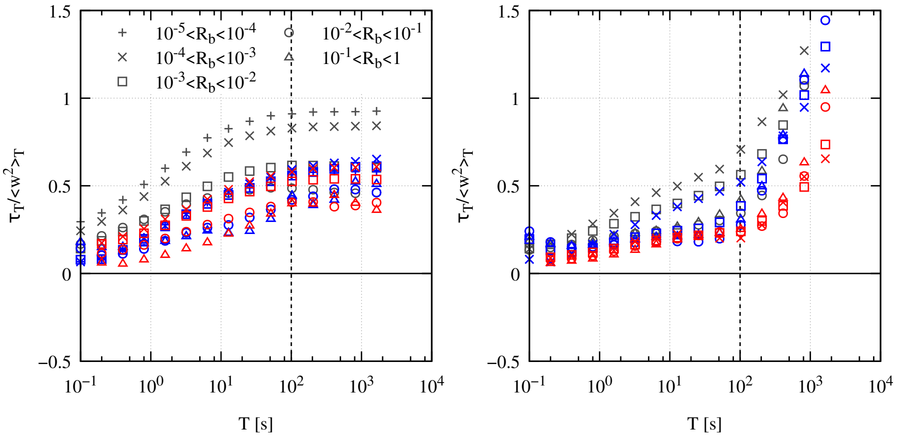

(a) $R_\tau < 0.3$

(b) $R_\tau > 1$

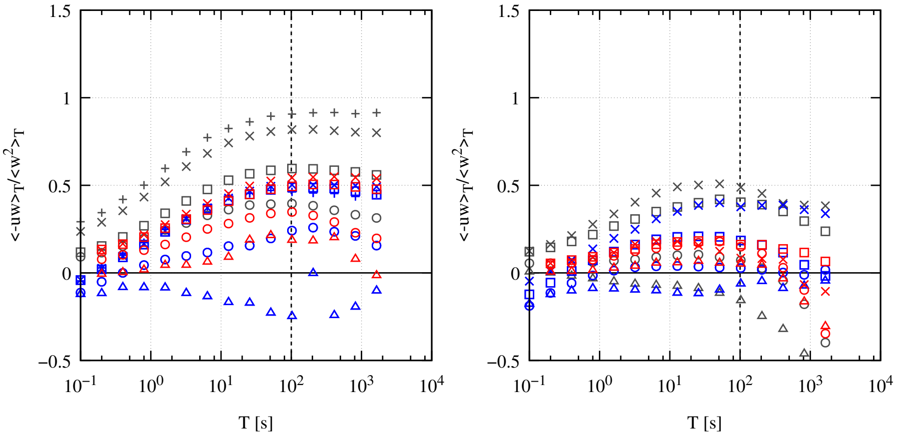

(c) $R_\tau < 0.3$

(d) $R_\tau > 1$

Figure 17: $\tau_T/\langle w^2\rangle_T$ and $\langle -uw\rangle_T/\langle w^2\rangle_T$ vs T (from MRD integrated (co)spectra) for different intervals of R_b, and for $R_\tau < 0.3$ and > 1. Median values for each R_b interval are reported (different symbols). Colours refer to different stations: black, NYA; blue, BAY; red, CCT ($z = 7.5\,\mathrm{m}$ only).

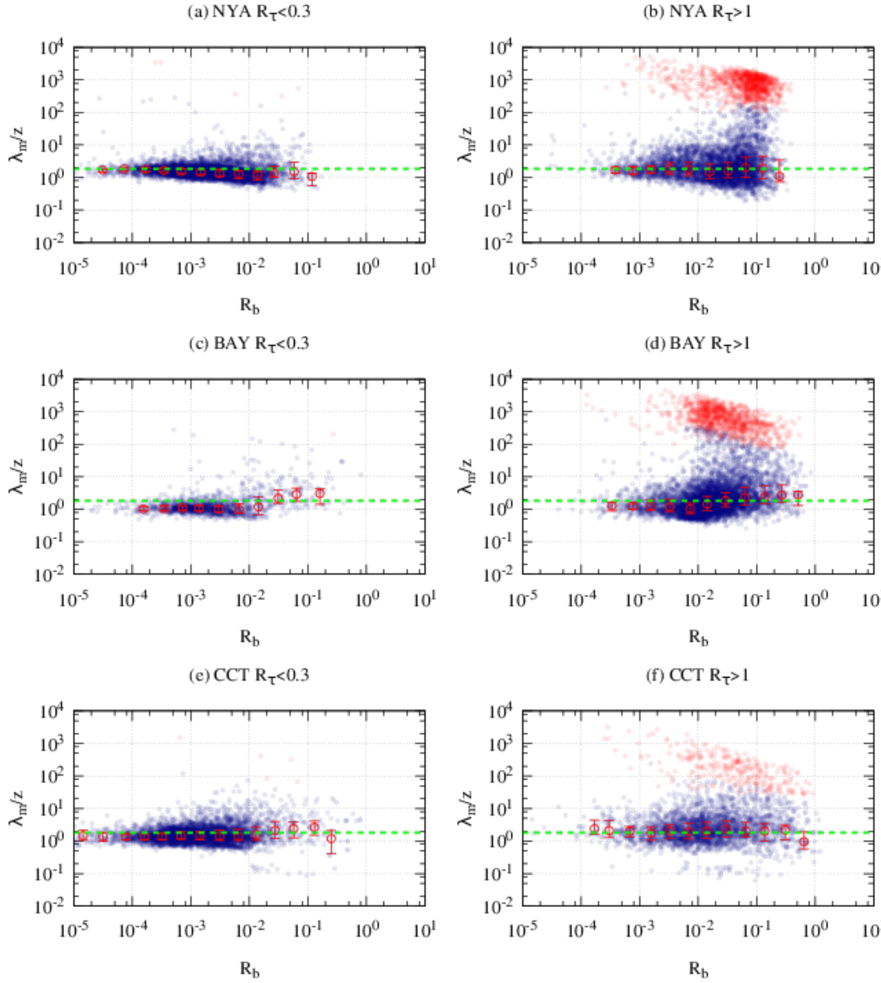

Figure 18: Peak wavelength of the w^2 MRD spectrum, $\lambda_\mathrm{m} \equiv UT_\mathrm{m}$, normalized by z, vs R_b, for $R_\tau < 0.3$ and > 1. Points correspond to 30-min records: blue, $T_\mathrm{m} < 400\,\mathrm{s}$; red, $T_\mathrm{m} > 400\,\mathrm{s}$. Open circles and errorbars are median values and 25th–75th percentile range of blue points binned in R_b. The green dashed line is the neutral limit of Kaimal and Finnigan (1994) similarity relationship.

5 Unstable Conditions

For unstable conditions, the heat flux and the vertical velocity variance have similar spectral distributions (Fig. 4a,c,d)—small contribution from time scales $\gtrsim 100\,\mathrm{s}$, well defined peak at $T \approx 10\,\mathrm{s}$—, suggesting a close relationship between them. The footprint area, where most of the contribution to the measured fluxes comes, is expected to be closer to the station than in near-neutral and stable conditions (Horst and Weil, 1994), thus requiring a shorter uniform fetch for measured fluxes to be representative of the local surface fluxes. Unstable conditions prevent the formation of submeso phenomena that rely on the stable temperature stratification—such as gravity waves, Kelvin-Helmholtz billows or drainage flows—but favour the onset of large convective eddies, which are an alternative source of low-frequency contribution. As free-convection conditions are approached (Kader and Yaglom, 1990), velocity fluctuations are driven by the vertical heat flux at the surface: buoyancy generated small-scale turbulence.

To select unstable conditions, negative $\Delta\Theta$ ($R_\mathrm{b} < 0$) or a positive heat flux at small scales, e.g., $\langle w\theta\rangle_{100\mathrm{s}} > 0$ ($z/\Lambda_{100\mathrm{s}} < 0$), must be imposed. Indeed, positive $\langle w\theta\rangle_{30\mathrm{min}}$ ($z/\Lambda_{30\mathrm{min}} < 0$) may correspond to stable cases (i.e., positive $\Delta\Theta$, negative $\langle w\theta\rangle_{100\mathrm{s}}$) because of the non-gradient low-frequency contribution to 30-min averages (Fig. 5a,c), and is thus an inappropriate criterion. However, once unstable conditions are correctly selected, for instance by imposing negative $\Delta\Theta$, the heat flux does not depend significantly on the averaging time: $\langle w\theta\rangle_{30\mathrm{min}} \approx \langle w\theta\rangle_{100\mathrm{s}}$, well correlated with the vertical gradient of temperature (Fig. 5, compare plots a and b, and c and d, for $\Delta\Theta < 0$).

Up to $-z/\Lambda \lesssim 10^{-1}$ ($-R_\mathrm{b} \lesssim 10^{-3}$) considerations made for near-neutral conditions apply (Sect. 3): the relation between the shear stress and the vertical velocity variance is affected by the low-frequency contribution to the former. According to Kader and Yaglom (1990), for $-z/\Lambda \gtrsim 10^{-1}$, the vertical velocity variance already follows the free convection scaling, with $\langle w^2\rangle \sim w_*^2$, where $w_* \equiv [-\beta z\langle w\theta\rangle]^{1/3}$ is the free-convection velocity scale (in the surface layer). This turns out to be a robust result, both from theoretical and empirical evidences, with observations that show a remarkably small scatter and good agreement among sites (e.g., Kader and Yaglom, 1990; de Franceschi et al., 2009; Stiperski et al., 2019). In these conditions, R_τ is not an important parameter.

Figure 19 shows the vertical velocity standard deviation, $(\sigma_w)_T \equiv \langle w^2\rangle_T^{1/2}$, vs the surface-layer free-convection velocity scale, $(w_*)_T \equiv (\beta z\langle w\theta\rangle_T)^{1/3}$, at the three stations, for $T = 100\,\mathrm{s}$ (Fig. 19a) and 30 min (Fig. 19b), considering all 30-min records with $-z/\Lambda_{100\mathrm{s}} > 0.3$ (without selection on R_τ or wind direction, which are not determinant on the observed behaviour). Observations follow the free-convection scaling $\sigma_w = 1.3 w_*$ (Kaimal and Finnigan, 1994) with remarkably small scatter and small differences among stations, both for 100-s and 30-min averages. This confirms that

- the similar shapes of the spectral distributions of the heat flux and the vertical velocity variance (Fig. 4a,c,e)—both dominated by high frequencies—underlies a close relationship between them;
- when vertical velocity fluctuations are driven by the heat flux they are in local equilibrium despite the complex terrain.

Figure 20 shows the stability dependence of the peak length scale of the

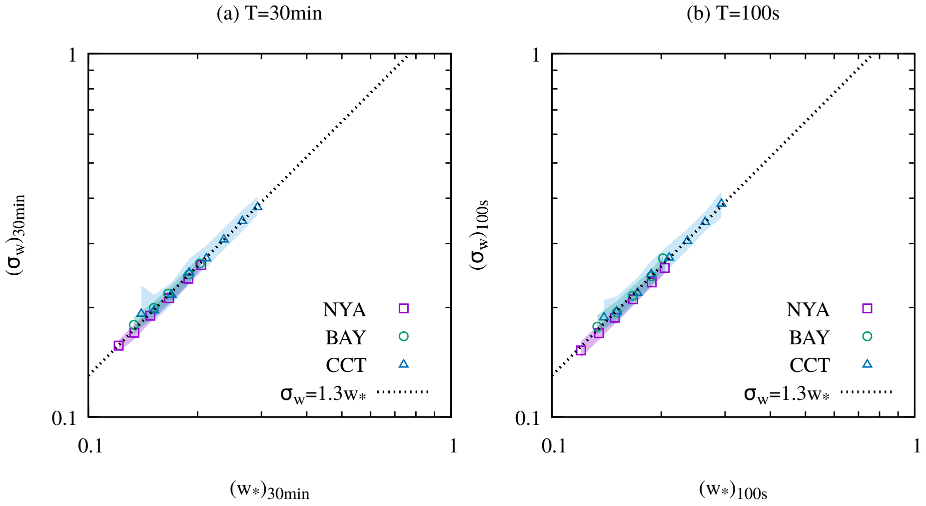

Figure 19: Standard deviation of the vertical velocity fluctuations, $(\sigma_w)_T \equiv \langle w^2 \rangle_T^{1/2}$, vs local free-convection velocity scale, $(w_*)_T \equiv (\beta z \langle w\theta \rangle_T)^{1/3}$, at the three stations, for (a) $T = 30\,\text{min}$ and (b) $T = 100\,\text{s}$. Data correspond to $z/\Lambda_T < -0.3$ and are binned in $(w_*)_T$: median values (points) and 25th–75th percentile range (shaded areas) are shown for each station. The free-convection relationship $\sigma_w = 1.3 w_*$ (Kaimal and Finnigan, 1994) is also reported.

w^2 MRD spectrum for unstable conditions, using $z/\Lambda_{30\text{min}}$ and R_b as stability parameters. As noted in Sect. 4.5 for stable conditions, the observed behaviour does not depend on the considered stability parameter—although, as expected, a better similarity among stations is achieved for z/Λ, because of the non-universality of R_b. However, contrary to what observed for stable conditions, for unstable conditions the peak length scale depends on stability, with λ_m/z that follows Kaimal et al. (1972) similarity relationship (Fig. 20a), approaching the free-convection scaling, $\lambda_\text{m} \approx 6z$, for $-z/\Lambda_{30\text{min}} \gtrsim 0.5$.

6 Modelling Implications

Results presented in Sects. 3 and 4 have implications on second-order moment budget equations and their closure assumptions, which may be valid for small-scale turbulence but are questionable for submeso motions.

6.1 Second-Order Moment Budget Equations

In a reference system aligned with the mean wind, i.e., $\vec{U} \equiv (U, 0, 0)$, assuming horizontal homogeneity, isotropy at small scales (thus neglecting viscous dissipation in flux budgets and taking the same viscous dissipation rate for the variances of three velocity components), no directional shear of the wind vector (i.e. $\partial V/\partial z = 0$), and neglecting the Coriolis effect, the budget equations for the variance of the three velocity components ($\langle u^2 \rangle$, $\langle v^2 \rangle$, and $\langle w^2 \rangle$), the kinematic fluxes of momentum ($\langle uv \rangle$, $\langle uw \rangle$, and $\langle vw \rangle$), the temperature variance ($\langle \theta^2 \rangle$), and the kinematic fluxes of heat ($\langle u\theta \rangle$, $\langle v\theta \rangle$, $\langle w\theta \rangle$) are, respectively, (e.g. Stull,

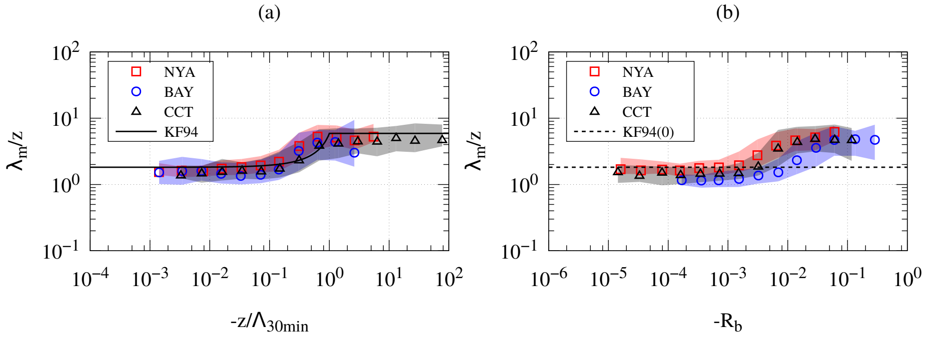

Figure 20: Stability dependence of the peak length scale of the w^2 MRD spectrum for unstable conditions: i.e., λ_{m}/z vs (a) $-z/\Lambda_{30\mathrm{min}}$ and (b) $-R_{\mathrm{b}}$. Data are binned in $z/\Lambda_{30\mathrm{min}}$ and R_{b}: median values (points) and 25th–75th percentile range (shaded areas) are shown for each station. Kaimal and Finnigan (1994, KF) similarity relationship and its neutral limit [KF94(0)] are also reported in (a) and (b), respectively.

1988)

$$Z_{uu} = -2\langle uw\rangle \frac{\partial U}{\partial z} + Q_{uu} - \frac{2}{3}\epsilon, \tag{11}$$

$$Z_{vv} = Q_{vv} - \frac{2}{3}\epsilon, \tag{12}$$

$$Z_{ww} = 2\beta\langle w\theta\rangle + Q_{ww} - \frac{2}{3}\epsilon, \tag{13}$$

$$Z_{uv} = -\langle vw\rangle \frac{\partial U}{\partial z} + Q_{uv}, \tag{14}$$

$$Z_{uw} = -\langle ww\rangle \frac{\partial U}{\partial z} + \beta\langle u\theta\rangle + Q_{uw}, \tag{15}$$

$$Z_{vw} = \beta\langle v\theta\rangle + Q_{vw}, \tag{16}$$

$$Z_{\theta\theta} = -2\langle w\theta\rangle \frac{\partial \Theta}{\partial z} - 2\epsilon_\theta, \tag{17}$$

$$Z_{u\theta} = -\langle uw\rangle \frac{\partial \Theta}{\partial z} - \langle w\theta\rangle \frac{\partial U}{\partial z} - Q_{u\theta}, \tag{18}$$

$$Z_{v\theta} = -\langle vw\rangle \frac{\partial \Theta}{\partial z} - Q_{v\theta}, \tag{19}$$

and

$$Z_{w\theta} = \beta\langle \theta^2\rangle - \langle ww\rangle \frac{\partial \Theta}{\partial z} + Q_{w\theta}; \tag{20}$$

where

$$Z_{\alpha\beta} \equiv \frac{\partial\langle\alpha\beta\rangle}{\partial t} + \frac{\partial \Phi_{\alpha\beta}}{\partial z} \tag{21}$$

is the sum of the time derivative and the vertical divergence of third-order moments , $\Phi_{\alpha\beta}$, such as turbulent transport; $Q_{\alpha\beta}$ is the “pressure-redistribution” or “return-to-isotropy” term, with $Q_{uu} + Q_{vv} + Q_{ww} = 0$ from the continuity equation; ϵ and ϵ_θ are the viscous dissipation rate of TKE and half the temperature variance, respectively.

The equation for the TKE, i.e., $E_\mathrm{K} \equiv (\langle u^2 \rangle + \langle v^2 \rangle + \langle w^2 \rangle)/2$, is obtained by summing Eqs. (11)–(13) and reads

$$Z_\mathrm{K} = -\langle uw \rangle \frac{\partial U}{\partial z} + \beta \langle w\theta \rangle - \epsilon, \tag{22}$$

where $Z_\mathrm{K} \equiv Z_{uu} + Z_{vv} + Z_{ww}$.

In principle, angle brackets in Eqs. (11)–(22) indicate ensemble averages. In practice, ensemble averages must be substituted with time (or space) averages. Variables are separated into a "mean" component and a "turbulent" fluctuation. Time averages converge to ensemble averages if (large) scales responsible for the mean component are separated from (small) scales responsible for the "turbulent" fluctuation, i.e., if a spectral gap exists and the averaging time is chosen in this gap. If this condition is satisfied—along with the assumptions stated above (i.e., horizontal homogeneity, etc.)—Eqs. (11)–(22) are valid independently of the spectral distribution of second-order moments, i.e., in our case, independently of the submeso contribution to them. But closures, such as MOST, are not independent of the type (i.e., the scales) of motions. For this reason, variables are separated into three contributions: mean, submeso motions, and small-scale turbulence. In our case, the mean flow corresponds to time scales longer than the record length, i.e., 30 min, and U and Θ are 30-min averages; small-scale turbulence corresponds to time scales shorter than 100-s, and $\langle \alpha\beta \rangle_\mathrm{100s}$ are the relative (co)variances; submeso motions correspond to the scales in between, and the submeso contribution to $\langle \alpha\beta \rangle$ is evaluated as $\langle \alpha\beta \rangle_\mathrm{30min} - \langle \alpha\beta \rangle_\mathrm{100s}$ (Sect. 2.5). With this decomposition, Eqs. (11)–(22) evaluated for small-scale turbulence, i.e., for 100-s (co)variances, should contain additional terms related to the interaction with submeso motions (Sect 6.4). The limitation of this approach is that a clear separation between submeso motions and small scale turbulence (and between submeso motions and mean flow) often does not exist.

6.2 Closures

Also in the simplified case where $Z_{\alpha\beta} = 0$, to solve Eqs. (11)–(22), closures are needed for the pressure redistribution and viscous dissipation terms. Closures developed for small-scale turbulence may non be valid in presence of significant submeso contribution.

6.2.1 Viscous Dissipation Rate

For modelling purposes, the viscous dissipation rate of TKE is written as

$$\epsilon = \frac{u_\epsilon^2}{t_\epsilon} \equiv \frac{u_\epsilon^{3/2}}{\ell_\epsilon}, \tag{23}$$

where u_ϵ, t_ϵ, and $\ell_\epsilon \equiv u_\epsilon t_\epsilon$ are a velocity-, time-, and length-scale, respectively. A common choice is $u_\epsilon \propto E_\mathrm{K}$ (see e.g., Yamada and Mellor, 1975; Nieuwstadt, 1984b; Nakanishi, 2001; Zilitinkevich et al., 2013), and $l_\epsilon \propto z$ for near-neutral conditions. However, horizontal velocity variances (and thus E_K) are affected by a significant submeso contribution (Figs. 4 and 8b), whose relative amount may depend on wind speed (Schiavon et al., 2019) and stability (Fig. 8b). Since dissipation is related to small scales and $\langle w^2 \rangle$ is a "small-scale" statistic (Figs. 4, 8a and S10), a proper choice is $u_\epsilon \propto \langle w^2 \rangle^{1/2}$. Accordingly, the dissipation rate is written as

$$\epsilon = \frac{\sigma_w^2}{t_\epsilon}. \tag{24}$$

A similar parametrization was adopted by Hunt et al. (1987). For near neutral and stable conditions, Fig. 18 suggests $\ell_\epsilon \propto z$ independent of stability, and thus $t_\epsilon = c_\epsilon z / \langle w^2 \rangle^{1/2}$. Previous analysis at the CCT station indicates $c_\epsilon \approx 1$ (Schiavon et al., 2019).

Analogously, the viscous dissipation rate of temperature variance is written as

$$\epsilon_\theta = c_\theta \frac{\theta_\epsilon^2}{t_\epsilon}, \tag{25}$$

where θ_ϵ is a temperature scale, t_ϵ is the time scale defined above, and c_θ is a parameter, which may depend on stability. A common choice is $\theta_\epsilon = \langle \theta^2 \rangle^{1/2}$ (e.g. Yamada and Mellor, 1975; Nieuwstadt, 1984b; Nakanishi, 2001; Zilitinkevich et al., 2013), but the significant submeso contribution to the temperature variance (Fig. 4b,d,f) would suggest an alternative temperature scale. Since there is no spectral gap in the distribution of $\langle \theta^2 \rangle$ (Fig. 4b,d,f), even $\theta_\epsilon = \langle \theta^2 \rangle_{100\mathrm{s}}^{1/2}$ may be inappropriate. This point is left for future research.

6.2.2 Pressure redistribution

The pressure-redistribution terms, $Q_{\alpha\beta}$, are traditionally parametrized using the "return-to-isotropy" hypothesis (Rotta, 1951). For the three velocity variances we have

$$Q_{\alpha\alpha} = -\frac{1}{c_{\alpha\alpha} t_\epsilon} \left(\langle \alpha^2 \rangle - \frac{2}{3} E_\mathrm{K} \right), \tag{26}$$

for $\alpha = u, v, w$; and where $c_{\alpha\alpha}$, taken equal for the three velocity components (i.e., $c_{uu} = c_{vv} = c_{ww} \equiv c_\mathrm{K}$), is treated as a universal dimensionless constant expressing the ratio between the pressure-redistribution time scale and the energy-dissipation time scale, t_ϵ. Eq. 26 produces unrealistic results for stable conditions (Zilitinkevich et al., 2013, who propose an alternative parametrization), weak wind (Schiavon et al., 2019), and in presence of meandering motions (Mortarini et al., 2019, who take c_K dependent on stability and different for meandering and non-meandering conditions). The fact that Eq. 26 depends on E_K makes it sensitive to the submeso contribution. Alternative parametrizations depend also on the wind shear, $\partial U / \partial z$ (e.g., Yamada and Mellor, 1975; Nieuwstadt, 1984b).

The Rotta-type closure for heat and momentum fluxes is

$$Q_{\alpha\beta} = -\frac{\langle \alpha\beta \rangle}{c_{\alpha\beta} t_\epsilon}, \tag{27}$$

for $\alpha, \beta = u, v, w, \theta$ and $\alpha \neq \beta$. Using the "effective-dissipation" hypothesis (Zilitinkevich and Esau, 2007), supported by large-eddy simulation (LES) data, Zilitinkevich et al. (2013) write

$$Q_{\alpha w} + \beta \langle \alpha\theta \rangle = -\frac{\langle \alpha w \rangle}{c_{\alpha w}^* t_\epsilon}, \tag{28}$$

for $\alpha = u, v$, and where $c^*_{\alpha w}$ is the effective-dissipation time-scale constant. Because t_ϵ is a time scale for small-scale turbulence, Eqs. (27) and (28) may become questionable for significant submeso contribution to $\langle \alpha\beta \rangle$.

6.3 The Flux-Gradient Relationship for $\langle uw \rangle$

Because presented results focused mainly on the relation between the shear stress and the vertical velocity variance (Sects. 3 and 4) here we consider the budget equation for $\langle uw \rangle$, Eq. (15). We assume $Z_{uw} = 0$, i.e., negligible divergence of third-order moments and steady conditions. Substituting, from Eq. (27),

$$Q_{uw} = -\frac{\langle uw \rangle}{c_{uw} t_\epsilon} \tag{29}$$

in Eq. (15), it becomes

$$-\langle w^2 \rangle \frac{\partial U}{\partial z} + \beta \langle u\theta \rangle - \frac{\langle uw \rangle}{c_{uw} t_\epsilon} = 0. \tag{30}$$

The buoyancy term, $\beta \langle u\theta \rangle$, is obtained from Eq. (18), assuming $Z_{u\theta} = 0$ and taking

$$Q_{u\theta} = -\frac{\langle u\theta \rangle}{c_{u\theta} t_\epsilon} \tag{31}$$

from Eq. (27). Substituted in Eq. (30), it results

$$\langle -uw \rangle \left(1 + \beta c_{uw} c_{u\theta} t_\epsilon^2 \frac{\partial \Theta}{\partial z} \right) = c_{uw} t_\epsilon \left(\langle w^2 \rangle + \beta c_{u\theta} t_\epsilon \langle w\theta \rangle \right) \frac{\partial U}{\partial z} \tag{32}$$

which is a flux-gradient relationship with eddy diffusion coefficient dependent on the vertical heat flux and the mean temperature gradient.

For neutral conditions, Eq. 32 reduces to

$$\langle -uw \rangle = c_{uw} t_\epsilon \langle w^2 \rangle \frac{\partial U}{\partial z}. \tag{33}$$

Using $t_\epsilon = c_\epsilon z / \langle w^2 \rangle^{1/2}$ (Sect. 6.2.1) and the law of the wall for the velocity profile,

$$\frac{\partial U}{\partial z} = \frac{\langle -uw \rangle^{1/2}}{\kappa z}, \tag{34}$$

Eq. (33) becomes

$$\left(\frac{\langle -uw \rangle}{\langle w^2 \rangle} \right)^{1/2} = \frac{c_{uw} c_\epsilon}{\kappa}, \tag{35}$$

which relates the neutral value of the flux-variance ratio to the value of c_{uw}.

Starting again from Eq. (15), with $Z_{uw} = 0$, but using the effective-dissipation closure for the pressure redistribution term, i.e., Eq. (28), we have

$$\langle -uw \rangle = \langle w^2 \rangle c^*_{uw} t_\epsilon \frac{\partial U}{\partial z}, \tag{36}$$

which looks simpler than Eq. (32) and is equivalent to Eq. (33) for near-neutral conditions, where $c_{uw} = c^*_{uw}$.

6.4 Waves and Wave-Turbulence Interactions

In presence of submeso motions, a set of equations like Eqs.(11)–(22) may still be used for small-scale turbulence—i.e., for $\langle\alpha\beta\rangle$ evaluated over averaging times longer than the turbulence time scale but shorter than the submeso time scale—, but with additional terms due to the interaction with submeso motions.

Among submeso motions that play an important role in the SBL are waves (Sun et al., 2015). Examples of waves are buoyancy-generated gravity waves, such as internal gravity waves (IGW), and transverse-vorticity generated waves, such as Kelvin-Helmholtz (KH) billows. Buoyancy waves are initiated by vertical displacement of streamlines (e.g., flow over hills) and transport momentum but not heat. Vorticity waves are a result of shear instability and overturning of the stably stratified flow, and they produce a non-zero heat flux. Concerning wave-turbulence interaction, IGW can increase/decrease local shear stability and thus enhance/reduce existing turbulence: waves break generating turbulence that in turns has an impact on the waves evolution. Wave-turbulence interaction can affect heat transfer at wave frequency and modify wave amplitude.

6.4.1 Finnigan and Einaudi (1981), Finnigan et al. (1984)

Each variable is decomposed into a mean, a wavelike fluctuation, and a turbulent fluctuation (see Finnigan and Einaudi, 1981, Eqs. 3a,b,c): the averaging rules are reported in Finnigan et al. (1984, Eq. 2.4). The resulting second-order moment equations for small-scale turbulence and waves contain coupling terms.

For the kinetic energy of waves and turbulence the averaged equations are reported by Finnigan et al. (1984, Eqs. 2.15 and 2.16). The TKE equation for waves written for steady, horizontally homogeneous conditions, and zero vertical divergence of third-order terms is

$$0 = -\overline{\tilde{u}\tilde{w}}\frac{\partial U}{\partial z} + \Pi + \beta\overline{\tilde{\theta}\tilde{w}} - \epsilon_{\mathrm{W}} \tag{37}$$

where tilde indicates wavelike fluctuations while the overbar indicates averaging over a time much longer than the wave period; ϵ_W is the viscous dissipation of wave kinetic energy. Under the same conditions, the TKE equation for turbulence is

$$0 = -\overline{uw}\frac{\partial U}{\partial z} - \Pi + \beta\overline{\theta w} - \epsilon_{\mathrm{T}} \tag{38}$$

where ϵ_{T} is the viscous dissipation rate of turbulence TKE and

$$\Pi = \overline{\tilde{r}_{uw}\frac{\partial \tilde{u}}{\partial z}} + \overline{\tilde{r}_{vw}\frac{\partial \tilde{v}}{\partial z}} \tag{39}$$

is the wave-turbulence interaction term, with (Finnigan et al., 1984, Eq. 2.12)

$$\tilde{r}_{\alpha w} = [\alpha w] - \overline{\alpha w} \tag{40}$$

for $\alpha = u, v$; square brackets denote phase averaging, and $\overline{\alpha w}$ roughly corresponds to $\langle\alpha w\rangle_{100\mathrm{s}}$, in our notation, and $\tilde{r}_{\alpha w}$ expresses the wavelike modulation of the "instantaneous" turbulent flux.

For a discussion of the different terms in Eqs. (37) and (38), see Finnigan and Einaudi (1981, pag. 823 and 824 and Fig. 14). In particular, it turns out that

$\Pi < 0$, i.e., waves feed turbulence: although this occurs mainly at $z \gtrsim 100\,\mathrm{m}$, while below $\Pi \approx 0$ (see their Fig. 15 and comment at pag. 825). A consistent result is found by Zilitinkevich et al. (2009) (their Π^{W}, Sect. 6.4.3).

6.4.2 Baumert and Peters (2009)

Using an E_{K}-ϵ closure and an energy budget equation for IGWs, Baumert and Peters (2009) write a TKE budget equation for turbulence that contains a wave interaction term, with waves that can both feed turbulence or extract energy from it. In particular, they define a saturation index, f_S: $f_S = 0$ if there is no external source of energy for waves that, hence, extract energy from turbulence; $f_S = 1$ if there is an important source of energy for waves that, hence, feed turbulence. Specifically, their Eq. 34 is for purely wave-generated turbulence in absence of mean shear, i.e., $\partial U/\partial z = 0$.

6.4.3 Zilitinkevich et al. (2009)

Zilitinkevich et al. (2009) describe wave-turbulence interaction based on second-order moment equations, tacking into account explicitly the wave motion. Like Finnigan and Einaudi (1981), variables are decomposed into a mean, a wave fluctuation, and a turbulent fluctuation, but with different averaging rules. Second-order moment equations for small-scale turbulence contain wave-turbulence interaction terms, $\Pi^{\mathrm{W}}_{\alpha\beta}$, which must be added to Eqs. (11)–(22), written for $\langle\alpha\beta\rangle_{100\mathrm{s}}$. In particular, the IGW contribution to the production of

- stream-wise velocity variance, $\langle u^2\rangle$:

  $$\Pi^{\mathrm{W}}_{uu} = -2\left(\left\langle \langle u^2\rangle^{\mathrm{W}} \frac{\partial U^{\mathrm{W}}}{\partial x}\right\rangle_{\mathrm{W}} + \left\langle \langle uv\rangle^{\mathrm{W}} \frac{\partial U^{\mathrm{W}}}{\partial y}\right\rangle_{\mathrm{W}} + \left\langle \langle uw\rangle^{\mathrm{W}} \frac{\partial U^{\mathrm{W}}}{\partial z}\right\rangle_{\mathrm{W}}\right), \tag{41}$$

  which is expected to be positive;

- crosswind velocity variance, $\langle v^2\rangle$:

  $$\Pi^{\mathrm{W}}_{vv} = -2\left(\left\langle \langle uv\rangle^{\mathrm{W}} \frac{\partial V^{\mathrm{W}}}{\partial x}\right\rangle_{\mathrm{W}} + \left\langle \langle v^2\rangle^{\mathrm{W}} \frac{\partial V^{\mathrm{W}}}{\partial y}\right\rangle_{\mathrm{W}} + \left\langle \langle vw\rangle^{\mathrm{W}} \frac{\partial V^{\mathrm{W}}}{\partial z}\right\rangle_{\mathrm{W}}\right), \tag{42}$$

  which is expected to be positive;

- vertical velocity variance, $\langle w^2\rangle$:

  $$\Pi^{\mathrm{W}}_{ww} = -2\left(\left\langle \langle uw\rangle^{\mathrm{W}} \frac{\partial W^{\mathrm{W}}}{\partial x}\right\rangle_{\mathrm{W}} + \left\langle \langle vw\rangle^{\mathrm{W}} \frac{\partial W^{\mathrm{W}}}{\partial y}\right\rangle_{\mathrm{W}} + \left\langle \langle w^2\rangle^{\mathrm{W}} \frac{\partial W^{\mathrm{W}}}{\partial z}\right\rangle_{\mathrm{W}}\right), \tag{43}$$

  which is positive if $\langle w^2\rangle/(2E_{\mathrm{K}}) < 1/3$ (Zilitinkevich et al., 2009, Eq. 52), as it is in ABL flows;

- temperature variance, $\langle \theta^2\rangle$:

  $$\Pi^{\mathrm{W}}_{\theta\theta} = -2\left(\left\langle \langle u\theta\rangle^{\mathrm{W}} \frac{\partial \Theta^{\mathrm{W}}}{\partial x}\right\rangle_{\mathrm{W}} + \left\langle \langle v\theta\rangle^{\mathrm{W}} \frac{\partial \Theta^{\mathrm{W}}}{\partial y}\right\rangle_{\mathrm{W}} + \left\langle \langle w\theta\rangle^{\mathrm{W}} \frac{\partial \Theta^{\mathrm{W}}}{\partial z}\right\rangle_{\mathrm{W}}\right), \tag{44}$$

  which is positive (Zilitinkevich et al., 2009, Eqs. 56 and 57);

- vertical heat flux, $\langle w\theta\rangle$:

$$\Pi^{\mathrm{W}}_{w\theta} = -\left(\left\langle \langle u\theta\rangle^{\mathrm{W}} \frac{\partial W^{\mathrm{W}}}{\partial x}\right\rangle_{\mathrm{W}} + \left\langle \langle v\theta\rangle^{\mathrm{W}} \frac{\partial W^{\mathrm{W}}}{\partial y}\right\rangle_{\mathrm{W}} + \left\langle \langle w\theta\rangle^{\mathrm{W}} \frac{\partial W^{\mathrm{W}}}{\partial z}\right\rangle_{\mathrm{W}}\right), \tag{45}$$

which is positive (Zilitinkevich et al., 2009, Eq. 58);

- the vertical flux of stream-wise momentum, $\langle uw\rangle$:

$$\begin{aligned}\Pi^{\mathrm{W}}_{uw} = &-\left\langle \langle u^2\rangle^{\mathrm{W}} \frac{\partial W^{\mathrm{W}}}{\partial x}\right\rangle_{\mathrm{W}} - \left\langle \langle uv\rangle^{\mathrm{W}} \frac{\partial W^{\mathrm{W}}}{\partial y}\right\rangle_{\mathrm{W}} - \left\langle \langle uw\rangle^{\mathrm{W}} \frac{\partial W^{\mathrm{W}}}{\partial z}\right\rangle_{\mathrm{W}}\\ &-\left\langle \langle uw\rangle^{\mathrm{W}} \frac{\partial U^{\mathrm{W}}}{\partial x}\right\rangle_{\mathrm{W}} - \left\langle \langle vw\rangle^{\mathrm{W}} \frac{\partial U^{\mathrm{W}}}{\partial y}\right\rangle_{\mathrm{W}} - \left\langle \langle w^2\rangle^{\mathrm{W}} \frac{\partial U^{\mathrm{W}}}{\partial z}\right\rangle_{\mathrm{W}};\end{aligned} \tag{46}$$

- the vertical flux of crosswind momentum, $\langle vw\rangle$:

$$\begin{aligned}\Pi^{\mathrm{W}}_{vw} = &-\left\langle \langle uv\rangle^{\mathrm{W}} \frac{\partial W^{\mathrm{W}}}{\partial x}\right\rangle_{\mathrm{W}} - \left\langle \langle v^2\rangle^{\mathrm{W}} \frac{\partial W^{\mathrm{W}}}{\partial y}\right\rangle_{\mathrm{W}} - \left\langle \langle vw\rangle^{\mathrm{W}} \frac{\partial W^{\mathrm{W}}}{\partial z}\right\rangle_{\mathrm{W}}\\ &-\left\langle \langle uw\rangle^{\mathrm{W}} \frac{\partial V^{\mathrm{W}}}{\partial x}\right\rangle_{\mathrm{W}} - \left\langle \langle vw\rangle^{\mathrm{W}} \frac{\partial V^{\mathrm{W}}}{\partial y}\right\rangle_{\mathrm{W}} - \left\langle \langle w^2\rangle^{\mathrm{W}} \frac{\partial V^{\mathrm{W}}}{\partial z}\right\rangle_{\mathrm{W}};\end{aligned} \tag{47}$$

where $\langle\alpha\beta\rangle^{\mathrm{W}}$ ($\alpha, \beta = u, v, w, \theta$) are the instantaneous (co)variances caused by IGWs (i.e., modulation of tubulent fluxes by IGWs); U^{W}, V^{W}, W^{W}, Θ^{W} are velocity and temperature wavelike fluctuations; $\langle\ldots\rangle_{\mathrm{W}}$ indicates averaging over a wave period. The IGW contribution to turbulence-TKE is $\Pi^{\mathrm{W}} \equiv \Pi^{\mathrm{W}}_{uu} + \Pi^{\mathrm{W}}_{vv} + \Pi^{\mathrm{W}}_{ww}$ (Zilitinkevich et al., 2009, Eq. 49) and is always > 0, in agreement with Finnigan et al. (1984) (Sect. 6.4.1).

IGWs contribute to the total vertical flux of momentum (i.e., waves + turbulence), i.e. $\langle uw\rangle + \langle U^{\mathrm{W}}W^{\mathrm{W}}\rangle_{\mathrm{W}}$, which roughly corresponds to our $\langle uw\rangle_{30\mathrm{min}}$, while $\langle uw\rangle$ to $\langle uw\rangle_{100\mathrm{s}}$. $\langle U^{\mathrm{W}}W^{\mathrm{W}}\rangle_{\mathrm{W}} < 0$, thus enhancing the vertical transport, if IGWs irradiate from ground (for instance, hilly terrain); $\langle U^{\mathrm{W}}W^{\mathrm{W}}\rangle_{\mathrm{W}} > 0$, if IGWs irradiate from the top of the interested layer (for instance, presence of a critical layer at the ABL top). We observe positive low-frequency contribution to $\langle uw\rangle_{30\mathrm{min}}$ at all stations (Sect. 4.3), which is consistent with IGWs irradiating from the top of the layer.

6.5 The Budget of $\langle uw\rangle$ at the CCT Station

We now consider the $\langle uw\rangle$ budget, Eq. 30, at the CCT station, where $\partial U/\partial z$ is available, and how is affected by the averaging time and R_τ.

The $\langle uw\rangle$ relaxation-time constant, c_{uw}, is determined from Eq. 33: taking $\kappa = 0.37$ (Fig. S12a,c), $c_\epsilon = 1$ (Schiavon et al., 2019), and $(\langle -uw\rangle/\langle w^2\rangle)^{1/2} = 0.8$ in the neutral limit (Fig. 13c,d; $R_\tau < 0.3$), it results $c_{uw} = 0.3$. We use $c_{uw} = 0.3$ independent of stability.

Figure 21 shows the terms composing the $\langle uw\rangle$ budget, Eq. 30, normalized by $\left\langle w^2\right\rangle^{3/2}/z$, vs R_{b}, for 100-s and 30-min (co)variances, and $R_\tau < 0.3$ and > 1.

For $R_\tau < 0.3$, both for 100-s and 30-min covariances, there is an approximate balance among shear production, buoyancy, and pressure redistribution (parametrized as in Eq. (29)), at least up to $R_\mathrm{b} \approx 10^{-2}$. For larger stability, the residual is larger and increases with R_b. If the further constraint $R_{u\theta} < 0.3$ (Eq. 4) is imposed on the horizontal heat flux, i.e. a small low-frequency contribution is imposed to all second-order moments composing the $\langle uw \rangle$ budget (the low-frequency contribution to $\langle w^2 \rangle$ is always small, Fig. 8a), few data remains for $R_\mathrm{b} \gtrsim 10^{-2}$ (Fig. S13a). The fact that, despite $R_\tau < 0.3$, $R_\mathrm{b} \gtrsim 10^{-2}$ corresponds to large low-frequency contribution to the heat flux, is also visible in Fig. 21c: using 30-min fluxes, the buoyancy term is large and erratic for $R_\mathrm{b} \gtrsim 10^{-2}$, thus producing a large and erratic residual—considering mean values (full symbols), which differ from median values (open symbols) because of the large spread.

When $R_\tau > 1$, if 100-s (co)variances are considered (Fig. 21b), a negative residual ≈ -1 occurs also for $R_\mathrm{b} < 10^{-2}$. The large R_τ affects mainly the pressure redistribution term (blue triangles in Fig. 21b), which is much smaller compared to $R_\tau < 0.3$ (i.e., ≈ 0.5 vs ≈ 2): this explains most of the negative residual. If 30-min (co)variances are considered (Fig. 21d), the low-frequency contribution to $\langle uw \rangle$ and $\langle u\theta \rangle$ destroys the budget: note the large spread of the buoyancy and pressure-redistribution terms (and thus of the residual) compared with the relatively narrow distribution of the shear-production term, which, as expected, is negligibly affected by the averaging time (compare green circles in Figs. 21b and d).

Assuming that the budget Eq. 30 is valid also for $R_\tau > 1$, a smaller c_{uw} must be used to account for the negative residual: i.e., compared to viscous dissipation, pressure redistribution is more efficient (the characteristic time is smaller) when R_τ is larger. Alternatively, the budget Eq. 30 must be extended—$Z_{uw} \neq 0$ and/or additional terms must be considered due to topographic effects (Sect. 3.3, recall the characteristic behaviour at the CCT station: Fig. 13a,c for $R_\tau > 1$; Fig. 14f) or the interaction between small-scale turbulence and submeso motions (Sect. 6.4)—or the Rotta-type closure Eq. 29 is inappropriate—recall that a residual submeso contribution can affect 100-s fluxes when $R_\tau > 1$ (Fig. 4.3).

7 Conclusions

Two years of observations from three Arctic stations located in Ny-Ålesund (Svalbard) has been considered. The turbulent exchange in the atmospheric surface-layer has been studied focusing mainly on the similarity relationship between the shear stress, τ, and the vertical velocity variance, $\langle w^2 \rangle$. In particular, besides the stability effect predicted by MOST and the topographic influence, the effect of submeso motions on the $\tau/\langle w^2 \rangle$ similarity relationship has been investigated. This has been done by defining a parameter, R_τ, which quantifies the relative low-frequency contribution to the shear stress and thus the strength of the submeso effect. Results confirm that submeso motions affect small-scale-turbulence thus modifying the $\tau/\langle w^2 \rangle$ similarity relationship, which, besides stability and surface characteristics, depends on R_τ. This connects MOST applicability with profound characteristics of the turbulent flow—i.e., the different time scales of the flow and the interplay among them—giving an alternative interpretation of MOST applicability limits found by other authors.

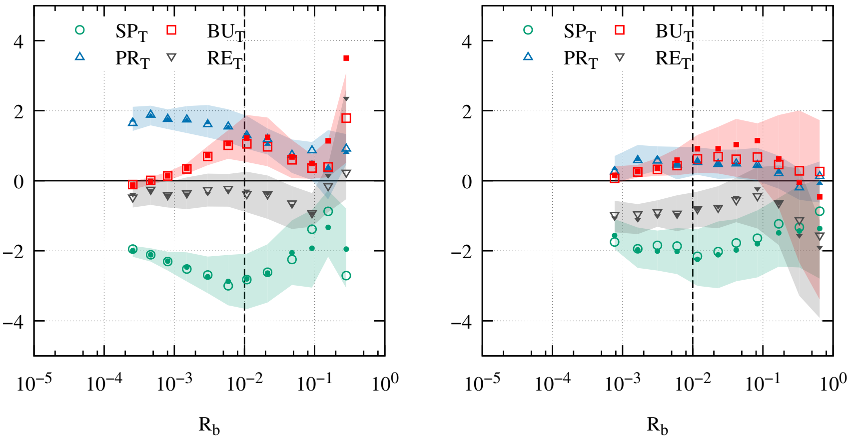

(a) T=100s R_τ<0.3

(b) T=100s R_τ>1

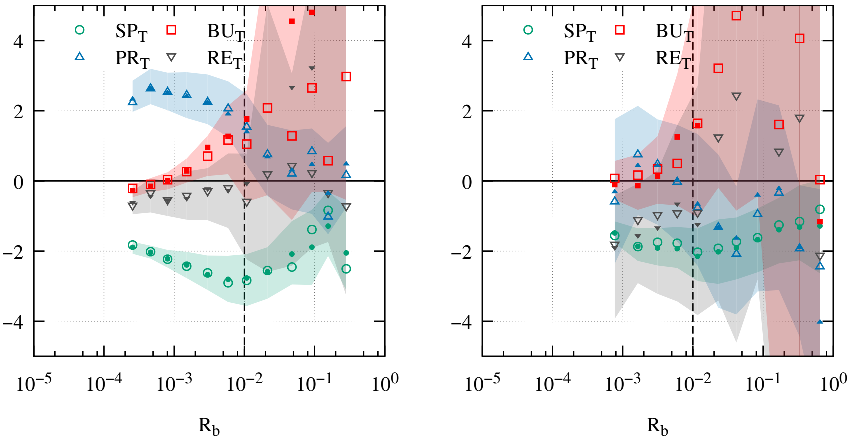

(c) T=30min R_τ<0.3

(d) T=30min R_τ>1

Figure 21: Dependence on R_b of the terms composing the $\langle uw\rangle_T$ budget, Eq. 30, normalized by $\langle w^2\rangle_T^{3/2}/z$, for $R_\tau < 0.3$ and > 1, and for $T = 100\,\mathrm{s}$ and $30\,\mathrm{min}$, at the CCT station ($z = 7.5\,\mathrm{m}$): shear production, $\mathrm{SP}_T \equiv -(z\partial U/\partial z)/\langle w^2\rangle_T^{1/2}$; buoyancy, $\mathrm{BU}_T \equiv z\beta\langle u\theta\rangle_T/\left\langle w^2\right\rangle_T^{3/2}$; pressure redistribution, $\mathrm{PR}_T \equiv -(1/c_{uw})\langle uw\rangle_T/\langle w^2\rangle_T$, with $c_{uw} = 0.3$; residual, RE_T, evaluated as the sum of the former terms. Data are binned in R_b: median values (open symbols), mean values (filled symbols) and 25th–75th percentile range (shaded areas) are reported.

In evaluating similarity relationships, the averaging time is crucial. For near-neutral and stable conditions, an averaging time $\approx 100\,\mathrm{s}$ is recommended at this site to exclude the submeso contribution to the vertical fluxes of heat and momentum. Compared with longer averaging times (e.g., 30 min), $T = 100\,\mathrm{s}$ improves similarity: among observations at a given station, among different stations, and between these results and those from other experiments. However, 100-s fluxes may still contain a residual submeso contribution when small-scale turbulence is weak ($\tau_{100\mathrm{s}} \lesssim 10^{-2}\,\mathrm{m}^2\,\mathrm{s}^{-2}$). This residual submeso contribution demands for (i) a more refined choice of the averaging time, in relation to the variable time scale of the spectral gap, and (ii) a deeper understanding of the physical significance of the gap—i.e., whether it corresponds to a real separation between small-scale turbulence and submeso motions or it is only the time scale where the two contributions sum to zero. For unstable conditions, 30-min averages are appropriate, as far as the vertical velocity variance, the vertical heat flux, and the temperature variance are considered.

As discussed above, submeso motions are not "inactive" in the surface layer (in the meaning of Townsend 1961 and Bradshaw 1967) and they contribute to the vertical fluxes of heat and momentum. For this reason, $\langle w^2 \rangle^{1/2}$, which is negligibly affected by the submeso contribution, is a better small-scale-turbulence velocity scale than $\tau^{1/2}$. The systematic submeso contribution to $\langle uw \rangle$ (which is positive at all stations) and $\langle vw \rangle$ deserves further investigation concerning, for instance, its relation with topography or with the presence of particular submeso motions such as gravity waves.

The main result of the study is that, like stability, the increasing submeso effect reduces the efficiency of the small-scale-turbulence vertical transport: i.e., $\tau/\langle w^2 \rangle$ evaluated for short averaging times (i.e. $< 100\,\mathrm{s}$) decreases for increasing R_τ. Larger R_τ is related to stronger interaction between small-scale turbulence and submeso motions and erosion of the positive small-scale contribution to $\langle -uw \rangle$ by the high-frequency tail of the negative submeso contribution. At the CCT station, larger R_τ corresponds also to stronger topographic effect.

Further research is required to better understand the topographic effect at the CCT station, concerning the interaction of the flow with the CCT relief, the existence of an internal boundary layer and, eventually, its height. Smaller topographic effects at the other stations are mainly related to the variation of the upwind fetch characteristics (homogeneous vs irregular), which determines the variability in the near-neutral value of $\tau/\langle w^2 \rangle$ among stations and wind directions.

For stable conditions, dynamical effects dominate on stability in determining turbulence behaviour: the shape of the vertical velocity spectrum and the length scale of small-scale turbulence are stability independent. This supports the important role of R_τ in stable conditions and suggests alternative roots for small-scale-turbulence production—of topographic or submeso origin—overwhelming buoyancy destruction. Furthermore, at least at this site, variations in the bulk Richardson number and the Obukhov length are mainly driven by the wind speed and the shear stress, respectively, thus confirming the secondary role of the temperature stratification and the vertical heat flux. For unstable conditions, as free-convection is approached, small-scale turbulence is driven by the vertical heat flux, universal relationships hold, and R_τ is no longer an important parameter.

Because of the complexity of the problem, it is unlikely that MOST applicability can be defined in terms of only one parameter. It is thus reasonable that different authors use different parameters and that $R_\tau \ll 1$ is not sufficient for MOST applicability but $R_\mathrm{b} \lesssim 10^{-2}$ (corresponding to $Ri, R_\mathrm{f} \lesssim 0.2$–$0.3$) is also necessary. In general, extending the analysis to other statistics and considering the multidimensional space of the R parameters associated to each of them (e.g., R_{uu}, R_{vv}, R_{ww}, $R_{w\theta}$, etc.), the hypothesis is that MOST applicability corresponds to the subspace where all the R parameters are $\ll 1$. To support this we recall that the simple $\langle uw \rangle$ budget— from which the $\tau/\langle w^2 \rangle$ relationship stems—holds for $R_\tau \ll 1$ and $R_\mathrm{b} \lesssim 10^{-2}$, which is equivalent to $R\tau \ll 1$ and $R_{u\theta} \ll 1$: i.e. the stability limit is related to the R parameter for the horizontal heat flux, and the budget holds when all the R parameters for its terms are small.

The effect of submeso motions on small-scale-turbulence has impacts on modelling closures and on the form of second-order moment equations. In particular, considering the budget of $\langle uw \rangle$ (i.e., the stream-wise component of the shear stress), a simple balance among shear production, buoyancy, and pressure redistribution (parametrized with a Rotta-type closure) does not hold when the submeso effect is significant: i.e., $R_\tau \gtrsim 1$ and $R_{u\theta} \gtrsim 1$. This demands for a modification of the closures (such as the pressure-redistribution time scale) and/or for an extension of the budget, with additional terms accounting for unsteadiness, vertical transport of third-order moments, and interaction of submeso motions with small-scale turbulence (similar to those used by Finnigan et al. 1984, Baumert and Peters 2009, and Zilitinkevich et al. 2009, to model wave-turbulence interactions).

Because RANS equations lumps all scales together, but the physics is sensitive to the involved scales and the interplay among them, spectral equations may represent an alternative approach to the problem.

Acknowledgements

I would like to thank the Atmo group of the Alfred Wegener Institute (Potsdam) that hosted me during part of my work, and, in particular, C. Ritter and A. Schulz, who also provided the data of the NYA station; the CCT Integrated Project group of the ISAC-CNR, and, in particular, A. Viola and M. Mazzola, who provided CCT data; my co-supervisor, S. Di Sabatino; my supervisor, O. Drofa. Finally, I thank F. Tampieri (ISAC-CNR), for his suggestions, discussions, and support.

References

Acevedo, O. C., F. D. Costa, P. E. Oliveira, F. S. Puhales, G. A. Degrazia, and D. Roberti, 2014: The influence of submeso processes on stable boundary layer similarity relationships. *Journal of the Atmospheric Sciences*, **71**, 207–225.

Acevedo, O. C. and L. Mahrt, 2010: Systematic vertical variation of mesoscale fluxes in the nocturnal boundary layer. *Boundary-layer meteorology*, **135**, 19–30.

Acevedo, O. C., L. Mahrt, F. S. Puhales, F. D. Costa, L. E. Medeiros, and G. A. Degrazia, 2016: Contrasting structures between the decoupled and coupled states of the stable boundary layer. *Quarterly Journal of the Royal Meteorological Society*, **142**, 693–702.

Andreas, E. L., 1987: Spectral measurements in a disturbed boundary layer over snow. *Journal of the atmospheric sciences*, **44**, 1912–1939.

Anfossi, D., D. Oettl, G. Degrazia, E. Ferrero, and A. Goulart, 2005: An analysis of sonic anemometer observations in low wind speed conditions. *Boundary-Layer Meteorol.*, **114**, 179–203.

Argentini, S., A. Viola, A. Maurizi, G. Mastrantonio, T. Georgiadis, and M. Nardino, 2003: Characteristics of the boundary layer at Ny-Ålesund in the Arctic during the ARTIST field experiment. *Annals of Geophysics*, **46**, 185–196.

Baas, P., G. J. Steeneveld, B. J. H. van de Wiel, and A. A. M. Holtslag, 2006: Exploring Self-Correlation in Flux–Gradient Relationships for Stably Stratified Conditions. *Journal Atmospheric Sciences*, **63**, 3045–3054.

Babić, K., M. W. Rotach, and Z. B. Klaić, 2016a: Evaluation of local similarity theory in the wintertime nocturnal boundary layer over heterogeneous surface. *Agricultural and Forest Meteorology*, **228**, 164–179.

Babić, N., Ž. Večenaj, and S. F. De Wekker, 2016b: Flux–variance similarity in complex terrain and its sensitivity to different methods of treating non-stationarity. *Boundary-layer meteorology*, **159**, 123–145.

Basu, S., F. Porte-Agel, E. Foufoula-Georgiou, J.-F. Vinuesa, and M. Pahlow, 2006: Revisiting the local scaling hypothesis in stably stratified atmospheric boundary-layer turbulence: an integration of field and laboratory measurements with large-eddy simulations. *Boundary-Layer Meteorology*, **119**, 473–500.

Baumert, H. Z. and H. Peters, 2009: Turbulence closure: turbulence, waves and the wave-turbulence transition – Part 1: Vanishing mean shear. *Ocean Science*, **5**, 47 – 58.

Beine, H. J., S. Argentini, A. Maurizi, G. Mastrantonio, and A. Viola, 2001: The local wind field at Ny-Ålesund and the Zeppelin mountain at Svalbard. *Meteorol. Atmos. Phys.*, **78**, 107–113.

Berg, J., J. Mann, A. Beckmann, M. Courtney, and H. E. Jorgensen, 2011: The Bolund Experiment, Part I: Flow Over a Steep, Three-Dimensional Hill. *Boundary-Layer Meteorology*, **141**, 219–243.

Bradshaw, P., 1967: "Inactive" motion and pressure fluctuations in turbulent boundary layers. *Journal of Fluid Mechanics*, **30**, 241–258.

Cava, D., U. Giostra, and M. Tagliazucca, 2001: Spectral maxima in a perturbed stable boundary layer. *Boundary-layer meteorology*, **100**, 421–437.

Cheng, Y. and W. Brutsaert, 2005: Flux–profile relationships for wind speed and temperature in the stable atmospheric boundary layer. *Boundary-Layer Meteorol.*, **114**, 519–538.

de Franceschi, M., D. Zardi, M. Tagliazucca, and F. Tampieri, 2009: Analysis of second order moments in surface layer turbulence in an alpine valley. *Quarterly Journal of the Royal Meteorological Society*, **135**, 1750–1765.

Falocchi, M., L. Giovannini, M. de Franceschi, and D. Zardi, 2019: A method to determine the characteristic time-scales of quasi-isotropic surface-layer turbulence over complex terrain: A case-study in the Adige Valley (Italian Alps). *Quarterly Journal of the Royal Meteorological Society*, **145**, 495–512.

Finnigan, J. J. and F. Einaudi, 1981: The interaction between an internal gravity wave and the planetary boundary layer. Part II: effect of the wave on the turbulence structure. *Quart. J. R. Met. Soc.*, **107**, 802–832.

Finnigan, J. J., F. Einaudi, and D. Fua, 1984: The interaction between an internal gravity wave and turbulence in the stably stratified nocturnal boundary layer. *J. Atmos. Sci.*, **41**, 2409–2436.

Foken, T. and B. Wichura, 1996: Tools for quality assessment of surface-based flux measurements. *Agricultural and forest meteorology*, **78**, 83–105.

Fortuniak, K., W. Pawlak, and M. Siedlecki, 2013: Integral turbulence statistics over a central european city centre. *Boundary-layer meteorology*, **146**, 257–276.

Frank, H. P., 1996: A simple spectral model for the modification of turbulence in flow over gentle hills. *Boundary-Layer Meteorology*, **79**, 345–373.

Fritts, D. C., L. Wang, J. Werne, T. Lund, and K. Wan, 2009: Gravity wave instability dynamics at high reynolds numbers. part i: Wave field evolution at large amplitudes and high frequencies. *Journal of the Atmospheric Sciences*, **66**, 1126–1148.

Gallagher, M. W., T. W. Choularton, and M. K. Hill, 1988: Some observations of airflow over a large hill of moderate slope. *Boundary-Layer Meteorology*, **42**, 229–250.

Grachev, A. A., E. L. Andreas, C. W. Fairall, P. S. Guest, and P. O. G. Persson, 2007: SHEBA flux-profile relationships in stable atmospheric boundary layer. *Boundary-Layer Meteorol*, **124**, 315–333.

Grachev, A. A., E. L. Andreas, C. W. Fairall, P. S. Guest, and P. O. G. Persson, 2013: The Critical Richardson Number and Limits of Applicability of Local Similarity Theory in the Stable Boundary Layer. *Boundary-Layer Meteorol*, **147**, 51–82.

Högström, U., 1996: Review of some basic characteristics of the atmospheric surface layer. *Boundary-Layer Meteorol*, **78**, 215–246.

Højstrup, J., 1982: Velocity spectra in the unstable planetary boundary layer. *Journal of the Atmospheric Sciences*, **39**, 2239–2248.

Horst, T. and J. C. Weil, 1994: How far is far enough?: the fetch requirements for micrometeorological measurement of surface fluxes. *J. Atmos. Ocean. Tech.*, **11**, 1018–1025.

Howell, J. F. and L. Mahrt, 1997: Multiresolution flux decomposition. *Boundary-Layer Meteorol*, 117–137.

Howell, J. F. and J. Sun, 1999: Surface-layer fluxes in stable conditions. *Boundary-Layer Meteorol*, 495–520.

Hunt, J., P. Spalart, and N. Mansour, 1987: A general form for the dissipation length scale in turbulent shear flows, *Studying Turbulence Using Numerical Simulation Databases. Proceedings of the 1987 Summer Program*, Stanford University.

Jackson, P. S. and J. C. R. Hunt, 1975: Turbulent wind flow over low hills. *Quart. J. Roy. Meteor. Soc.*, **101**, 929–956.

Jocher, G., F. Karner, C. Ritter, R. Neuber, K. Dethloff, F. Obleitner, J. Reuder, and T. Foken, 2012: The near-surface small-scale spatial and temporal variability of sensible and latent heat exchange in the Svalbard region: a case study. *ISRN Meteorology*, **2012**.

Kader, B. A. and A. M. Yaglom, 1990: Mean fields and fluctuation moments in unstably stratified turbulent boundary layers. *J. Fluid Mech.*, **212**, 637–662.

Kaimal, J., 1978: Horizontal velocity spectra in an unstable surface layer. *Journal of the Atmospheric Sciences*, **35**, 18–24.

Kaimal, J. C. and J. J. Finnigan, 1994: *Atmospheric boundary layer flows. Their structure and measurement.*, Oxford University Press.

Kaimal, J. C., J. C. Wyngaard, Y. Izumi, and O. R. Coté, 1972: Spectral characteristics of surface-layer turbulence. *Quart. J. Roy. Meteor. Soc.*, **98**, 563–589.

Klipp, C. L. and L. Mahrt, 2004: Flux-gradient relationship, self-correlation and intermittency in the stable boundary layer. *Quarterly J. Royal Meteorol. Soc.*, **130**, 2087–2103.

Kolmogorov, A. N., 1941: The local structure of turbulence in incompressible viscous fluid for very large Reynolds numbers. *Dokl. Akad. Nauk SSSR*, **30**, 301.

Liang, J., L. Zhang, Y. Wang, X. Cao, Q. Zhang, H. Wang, and B. Zhang, 2014: Turbulence regimes and the validity of similarity theory in the stable boundary layer over complex terrain of the Loess Plateau, China. *Journal of Geophysical Research: Atmospheres*, **119**, 6009–6021.

Mahrt, L., 2007: Weak-wind mesoscale meandering in the nocturnal boundary layer. *Environmental Fluid Mechanics*, **7**, 331–347.

Mahrt, L., 2014: Stably stratified atmospheric boundary layers. *Annu. Rev. Fluid Mech.*, **46**, 23–45.

Mahrt, L., J. Sun, and D. R. Stauffer, 2015: Dependence of Turbulent Velocities on Wind Speed and Stratification. *Boundary-Layer Meteorology*, **155**, 55–71.

Mahrt, L., C. Thomas, S. Richardson, N. Seaman, D. R. Stauffer, and M. Zeeman, 2013: Non-stationary generation of weak turbulence for very stable and weak-wind conditions. *Boundary-Layer Meteorology*, **147**, 179–199.

Mammarella, I., F. Tampieri, M. Tagliazucca, and M. Nardino, 2005: Turbulence perturbations in the neutrally stratified surface layer due to the interaction of a katabatic flow with a steep ridge. *Environmental Fluid Mechanics*, **5**, 227–246.

Mann, J., 2000: The spectral velocity tensor in moderately complex terrain. *Journal Wind Engineering Industrial Aerodynamics*, **88**, 153–169.

Maturilli, M., A. Herber, and G. König-Langlo, 2013: Climatology and time series of surface meteorology in ny-ålesund, svalbard. *Earth System Science Data*, **5**, 155.

Maturilli, M. and M. Kayser, 2017: Arctic warming, moisture increase and circulation changes observed in the Ny-Ålesund homogenized radiosonde record. *Theoretical and Applied Climatology*, **130**, 1–17.

Mauritsen, T., G. Svensson, S. S. Zilitinkevich, I. N. Esau, L. Enger, and B. Grisogono, 2007: A total turbulent energy closure model for neutrally and stably stratified atmospheric boundary layers. *Journal Atmospheric Sciences*, **64**, 4113–4126.

Mazzola, M., A. P. Viola, C. Lanconelli, and V. Vitale, 2016: Atmospheric observations at the Amundsen-Nobile Climate Change Tower in Ny-Ålesund, Svalbard. *Rendiconti Lincei*, **27**, 7–18.

Monin, A. and A. Obukhov, 1954: Basic laws of turbulent mixing in the surface layer of the atmosphere. *Contrib. Geophys. Inst. Acad. Sci. USSR*, **151**, e187.

Monin, A. S. and A. M. Yaglom, 1971: *Statistical fluid mechanics*, vol. I, MIT Press, Cambridge, 769 pp.

Mortarini, L., D. Cava, U. Giostra, F. D. Costa, G. Degrazia, D. Anfossi, and O. Acevedo, 2019: Horizontal meandering as a distinctive feature of the stable boundary layer. *Journal of the Atmospheric Sciences*.

Mortarini, L., M. Stefanello, G. Degrazia, D. Roberti, S. T. Castelli, and D. Anfossi, 2016: Characterization of wind meandering in low-wind-speed conditions. *Boundary-Layer Meteorology*, **161**, 165–182.

Nadeau, D. F., E. R. Pardyjak, C. W. Higgins, and M. B. Parlange, 2013: Similarity scaling over a steep alpine slope. *Boundary-layer meteorology*, **147**, 401–419.

Nakanishi, M., 2001: Improvement of the mellor–yamada turbulence closure model based on large-eddy simulation data. *Boundary-layer meteorology*, **99**, 349–378.

Nieuwstadt, F. T. M., 1984a: Some aspects of the turbulent stable boundary layer. *Boundary-Layer Meteorol*, **30**, 31–55.

Nieuwstadt, F. T. M., 1984b: The turbulent structure of the stable, nocturnal boundary layer. *J. Atmos. Sci.*, **41**, 2202–2216.

Obukhov, A., 1971: Turbulence in an atmosphere with a non-uniform temperature. *Boundary-layer meteorology*, **2**, 7–29.

Pahlow, M., M. Parlange, and F. Porte-Agel, 2001: On Monin-Obukhov similarity in the stable atmospheric boundary layer. *Boundary-Layer Meteorol.*, **99**, 225–248.

Panofsky, H., D. Larko, R. Lipschutz, G. Stone, E. F. Bradley, A. J. Bowen, and J. Hojstrup, 1982: Spectra of velocity components over complex terrain. *Quarterly Journal Royal Meteorological Society*, **108**, 215–230.

Rotta, J. C., 1951: Statisthe Theorie nichthomogener Turbulenz. *Z. Phys.*, **129**, 547–572.

Schiavon, M., F. Tampieri, F. Bosveld, M. Mazzola, S. T. Castelli, A. Viola, and C. Yagüe, 2019: The Share of the Mean Turbulent Kinetic Energy in the Near-Neutral Surface Layer for High and Low Wind Speeds. *Boundary-Layer Meteorology*, **172**, 81–106.

Sfyri, E., M. W. Rotach, I. Stiperski, F. C. Bosveld, M. Lehner, and F. Obleitner, 2018: Scalar-flux similarity in the layer near the surface over mountainous terrain. *Boundary-Layer Meteorology*, **169**, 11–46.

Sorbjan, Z., 2010: Gradient-based scales and similarity laws in the stable boundary layer. *Q J R Meteorol Soc*, **136**, 1243–1254.

Sorbjan, Z. and A. A. Grachev, 2010: An evaluation of the flux–gradient relationship in the stable boundary layer. *Boundary-Layer Meteorol.*, **135**, 385–405.

Stiperski, I. and M. Calaf, 2018: Dependence of near-surface similarity scaling on the anisotropy of atmospheric turbulence. *Quarterly Journal of the Royal Meteorological Society*, **144**, 641–657.

Stiperski, I., M. Calaf, and M. W. Rotach, 2019: Scaling, anisotropy, and complexity in near-surface atmospheric turbulence. *Journal of Geophysical Research: Atmospheres*, **124**, 1428–1448.

Stull, R. B., 1988: *An introduction to boundary layer meteorology*, Kluwer Academic Publishers.

Sun, J., D. H. Lenschow, M. A. LeMone, and L. Mahrt, 2016: The role of large-coherent-eddy transport in the atmospheric surface layer based on cases-99 observations. *Boundary-layer meteorology*, **160**, 83–111.

Sun, J., L. Mahrt, R. M. Banta, and Y. L. Pichugina, 2012: Turbulence regimes and turbulence intermittency in the stable boundary layer during cases-99. *Journal of the Atmospheric Sciences*, **69**, 338–351.

Sun, J., C. J. Nappo, L. Mahrt, D. Belusic, B. Grisogono, D. R. Stauffer, M. Pulido, C. Staquet, Q. Jiang, A. Pouquet, et al., 2015: Review of wave-turbulence interactions in the stable atmospheric boundary layer. *Reviews of geophysics*, **53**, 956–993.

Tampieri, F., 2017: *Turbulence and dispersion in the planetary boundary layer*, Springer International.

Townsend, A., 1961: Equilibrium layers and wall turbulence. *Journal of Fluid Mechanics*, **11**, 97–120.

Van de Wiel, B., A. Moene, H. Jonker, P. Baas, S. Basu, J. Donda, J. Sun, and A. Holtslag, 2012a: The minimum wind speed for sustainable turbulence in the nocturnal boundary layer. *Journal of the Atmospheric Sciences*, **69**, 3116–3127.

Van de Wiel, B., A. Moene, H. Jonker, P. Baas, S. Basu, J. Donda, J. Sun, and A. Holtslag, 2012b: The minimum wind speed for sustainable turbulence in the nocturnal boundary layer. *Journal of the Atmospheric Sciences*, **69**, 3116–3127.

Vercauteren, N., V. Boyko, D. Faranda, and I. Stiperski, 2019: Scale interactions and anisotropy in stable boundary layers. *Quarterly Journal of the Royal Meteorological Society*.

Vercauteren, N., L. Mahrt, and R. Klein, 2016: Investigation of interactions between scales of motion in the stable boundary layer. *Quarterly Journal of the Royal Meteorological Society*, **142**, 2424–2433.

Vickers, D. and L. Mahrt, 2003: The cospectral gap and turbulent flux calculations. *Journal of Atmospheric and Oceanic Technology*, **20**, 660–672.

Vickers, D. and L. Mahrt, 2006: A solution for flux contamination by mesoscale motions with very weak turbulence. *Boundary-layer meteorology*, **118**, 431–447.

Vickers, D. and L. Mahrt, 2007: observations of the cross-wind velocity variance in the stable boundary layer. *Environmental Fluid Mechanics*, **7**, 55–71.

Wilson, J. D., 2008: Monin-obukhov functions for standard deviations of velocity. *Boundary-Layer Meteorology*, **129**, 353–369.

Yamada, T. and G. Mellor, 1975: A simulation of the Wangara atmospheric boundary layer data. *Journal of the Atmospheric sciences*, **32**, 2309–2329.

Ying, R. and V. M. Canuto, 2007: Numerical simulation of flow over two-dimensional hills using a second-order turbulence closure model. *Boundary-Layer Meteorol.*, **85**, 447–474.

Zeman, O. and N. O. Jensen, 1987: Modification of turbulence characteristics in flow over hills. *Quart. J. Roy. Meteor. Soc.*, **113**, 55–80.

Zilitinkevich, S. S., T. Elperin, N. Kleeorin, V. L'vov, and I. Rogachevskii, 2009: Energy- and Flux-Budget Turbulence Closure Model for Stably Stratified Flows. Part II: The Role of Internal Gravity Waves. *Boundary-Layer Meteorology*, **133**, 139–164.

Zilitinkevich, S. S., T. Elperin, N. Kleeorin, and I. Rogachevskii, 2007: Energy- and flux-budget (EFB) turbulence closure model for stably stratified flows. Part I: steady-state, homogeneous regimes. *Boundary-Layer Meteorology*, **125**, 167–191.

Zilitinkevich, S. S., T. Elperin, N. Kleeorin, I. Rogachevskii, and I. N. Esau, 2013: A Hierarchy of Energy- and Flux-Budget (EFB) Turbulence Closure Models for Stably-Stratified Geophysical Flows. *Boundary-Layer Meteorol*, **146**, 341–373.

Zilitinkevich, S. S. and I. N. Esau, 2007: Similarity theory and calculation of turbulent fluxes at the surface for the stably stratified atmospheric boundary layer. *Boundary-Layer Meteorol*, **125**, 193–205.

Supplementary Material

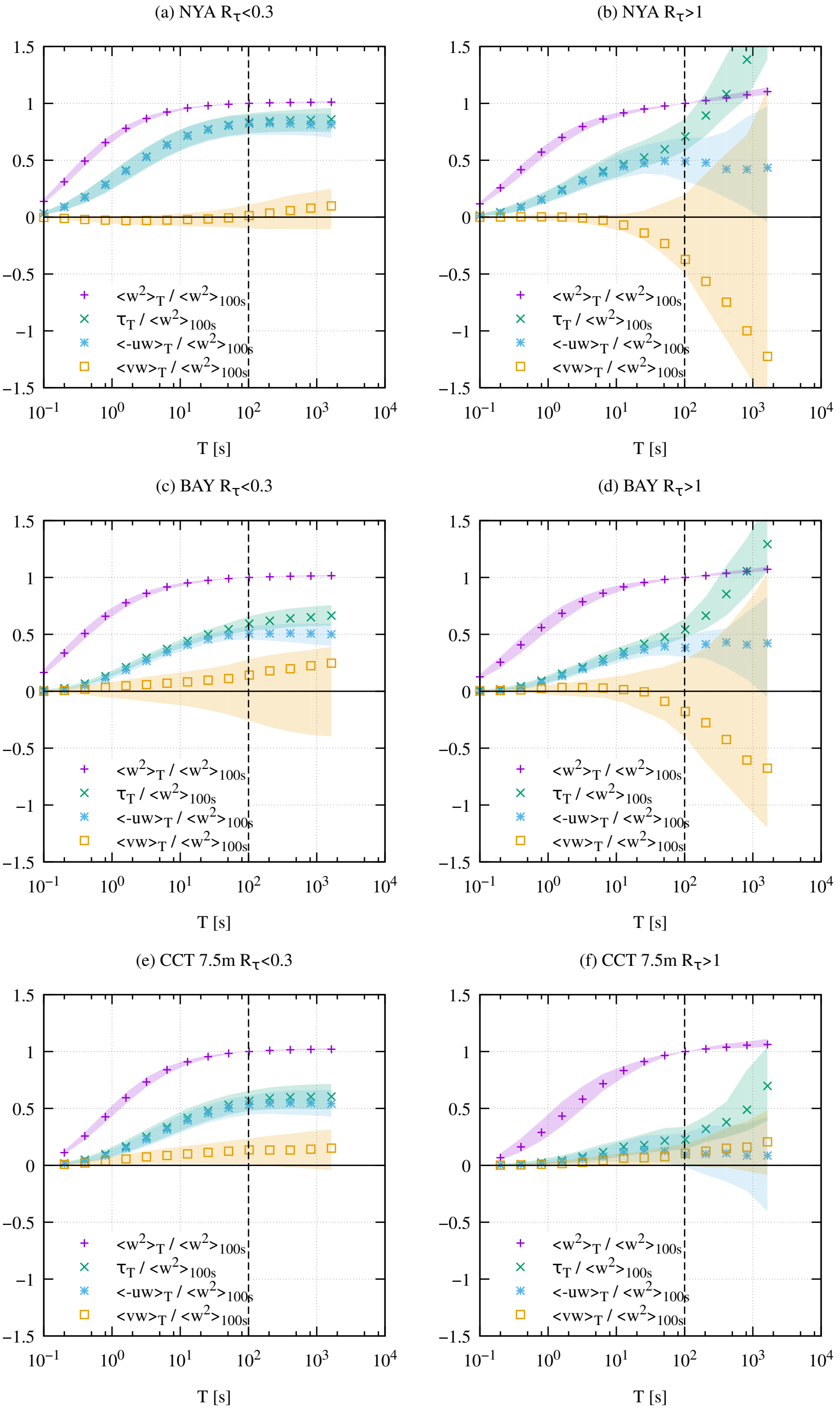

Figure S1: MRD integrated (co)spectra normalized over $\langle w^2\rangle_{100\mathrm{s}}$—i.e., $\langle w^2\rangle_T/\langle w^2\rangle_{100\mathrm{s}}$, $\tau_T/\langle w^2\rangle_{100\mathrm{s}}$, $\langle -uw\rangle_T/\langle w^2\rangle_{100\mathrm{s}}$, and $\langle vw\rangle_T/\langle w^2\rangle_{100\mathrm{s}}$ vs T—for $R_\tau < 0.3$ and > 1, near-neutral conditions ($|R_\mathrm{b}| < 0.001$), $\tau_{100\mathrm{s}} > 0.01\,\mathrm{m^2\,s^{-2}}$, all wind directions: median values (points) and 25th–75th percentile range (shaded areas); CCT (co)spectra refer to $z = 7.5\,\mathrm{m}$.

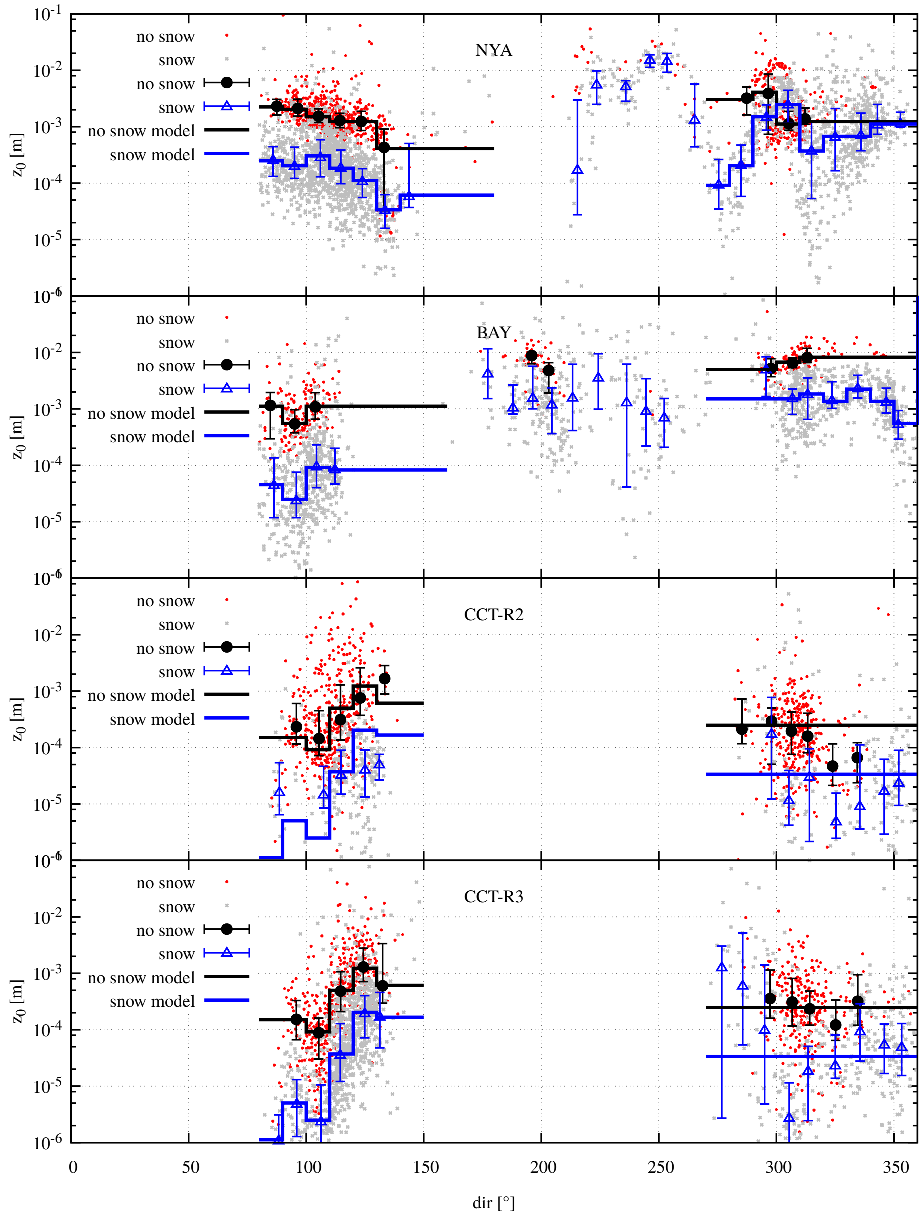

Figure S2: Dynamic roughness length, z_0, from Eq. 8, vs wind direction, for snow-free and snow-covered surface. Each point corresponds to a 30-min record; median values and 25th–75th percentile range in wind-direction bins are also reported.

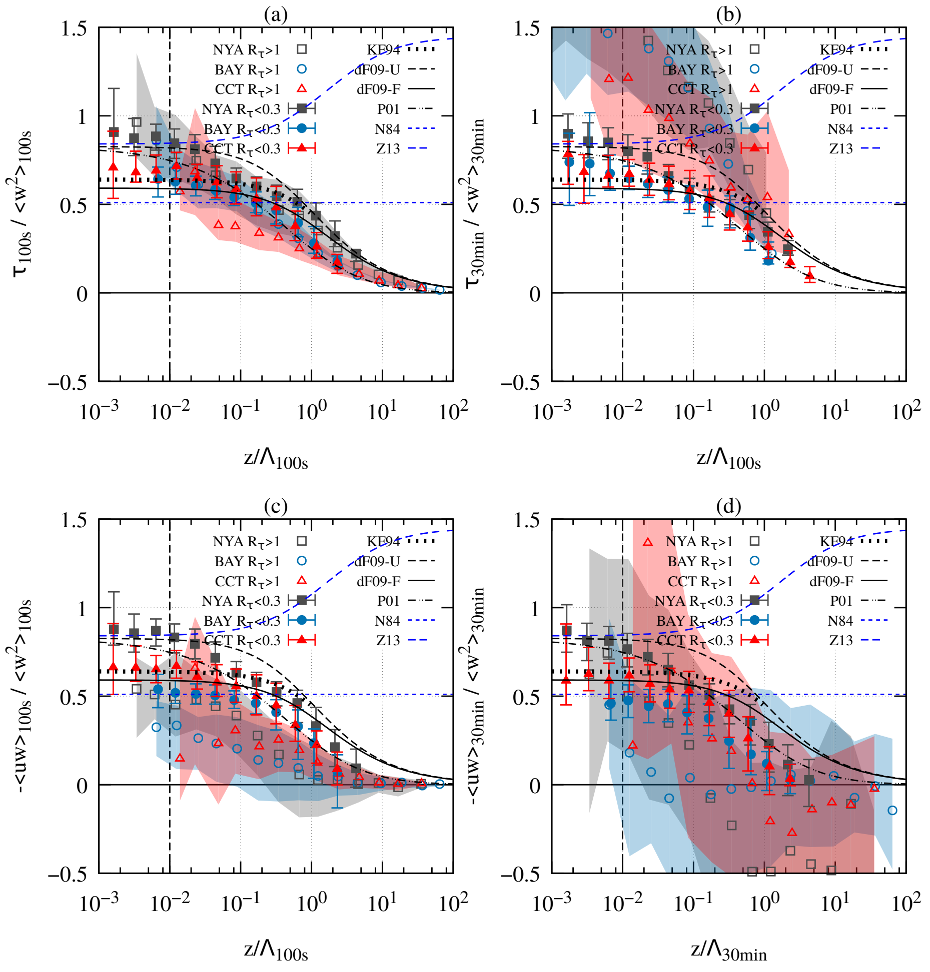

Figure S3: As in Fig. 13 but with z/Λ_T as stability parameter.

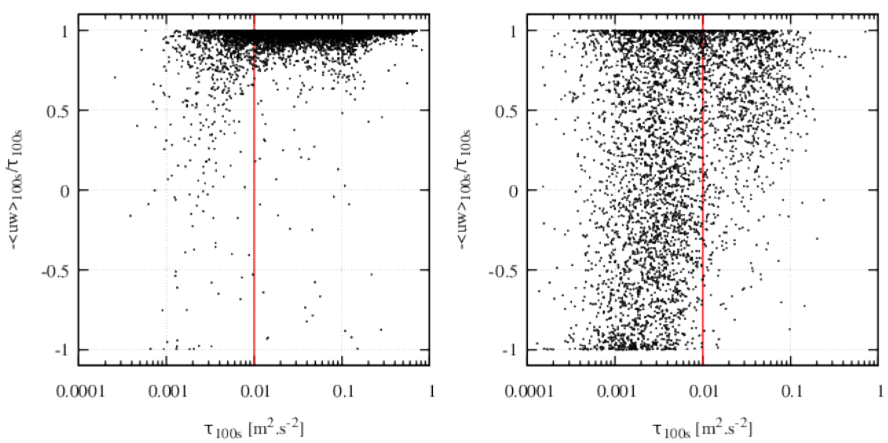
(a) NYA $R_\tau<0.3$ (b) NYA $R_\tau>1$

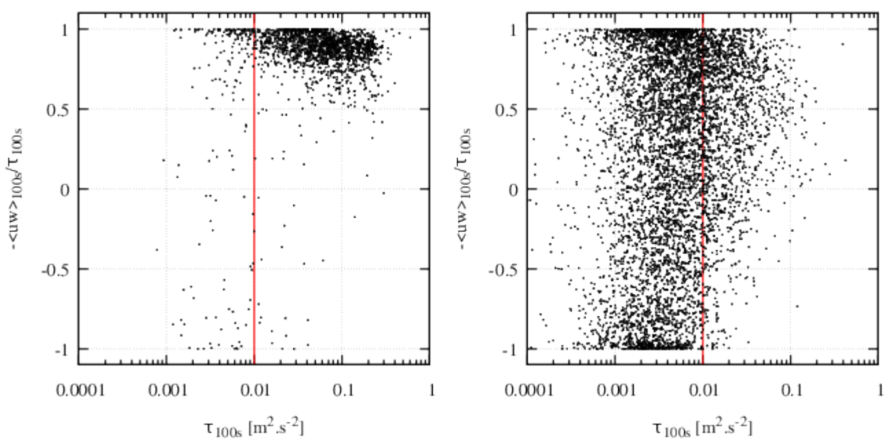
(c) BAY $R_\tau<0.3$ (d) BAY $R_\tau>1$

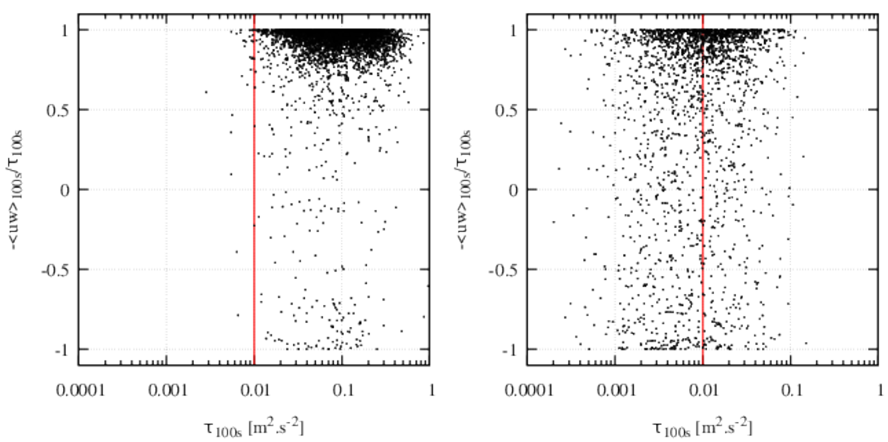
(e) CCT R2+R3 $R_\tau<0.3$ (f) CCT R2+R3 $R_\tau>1$

Figure S4: $\langle -uw\rangle_{100\mathrm{s}}/\tau_{100\mathrm{s}}$ vs $\tau_{100\mathrm{s}}$: each point corresponds to a 30-min record; $\tau_{100\mathrm{s}} = 10^{-2}\,\mathrm{m}^2\,\mathrm{s}^{-2}$ is also indicated.

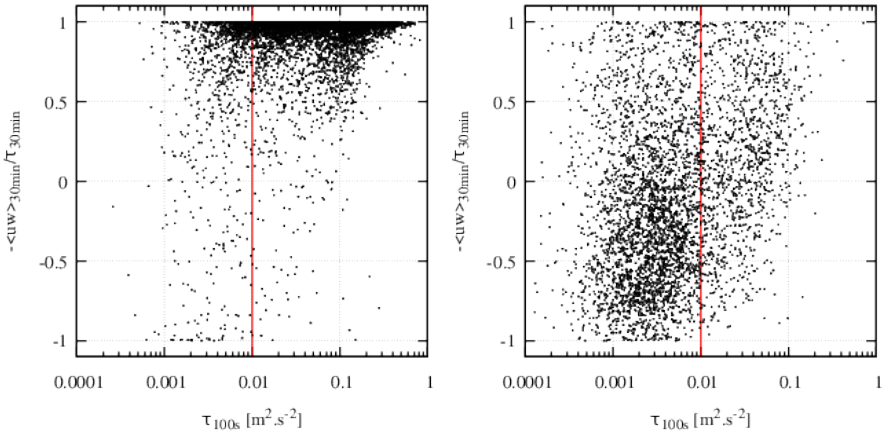

(a) NYA R_τ<0.3

(b) NYA R_τ>1

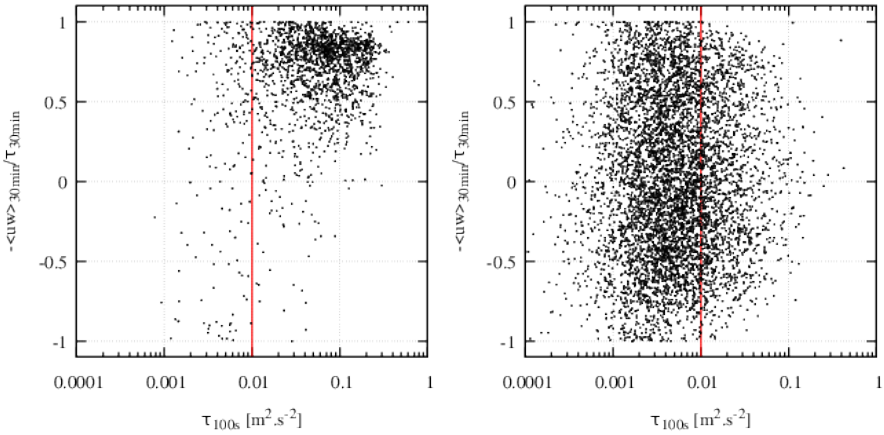

(c) BAY R_τ<0.3

(d) BAY R_τ>1

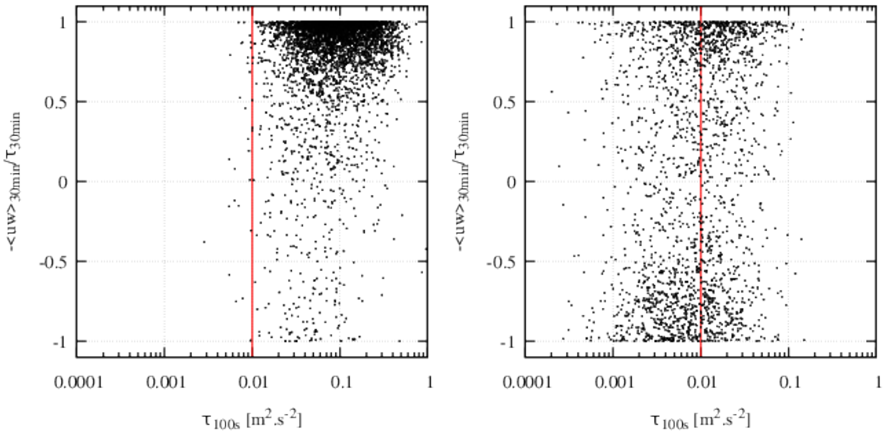

(e) CCT R2+R3 R_τ<0.3

(f) CCT R2+R3 R_τ>1

Figure S5: As in Fig. S4, but for $\langle -uw \rangle_{30\mathrm{min}} / \tau_{30\mathrm{min}}$.

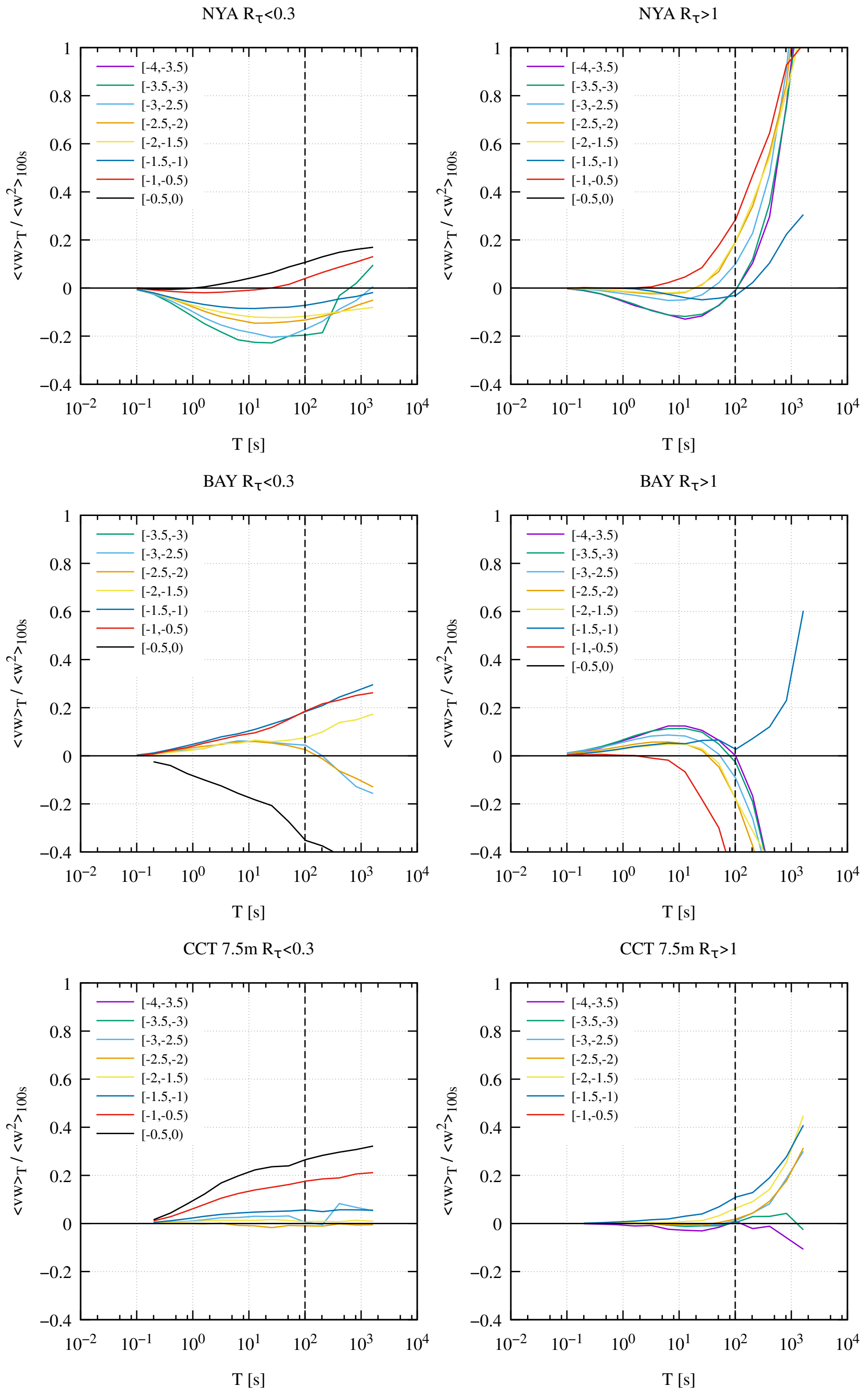

Figure S6: As in Fig. 15, but for the crosswind component of the shear stress, $\langle vw\rangle_T$.

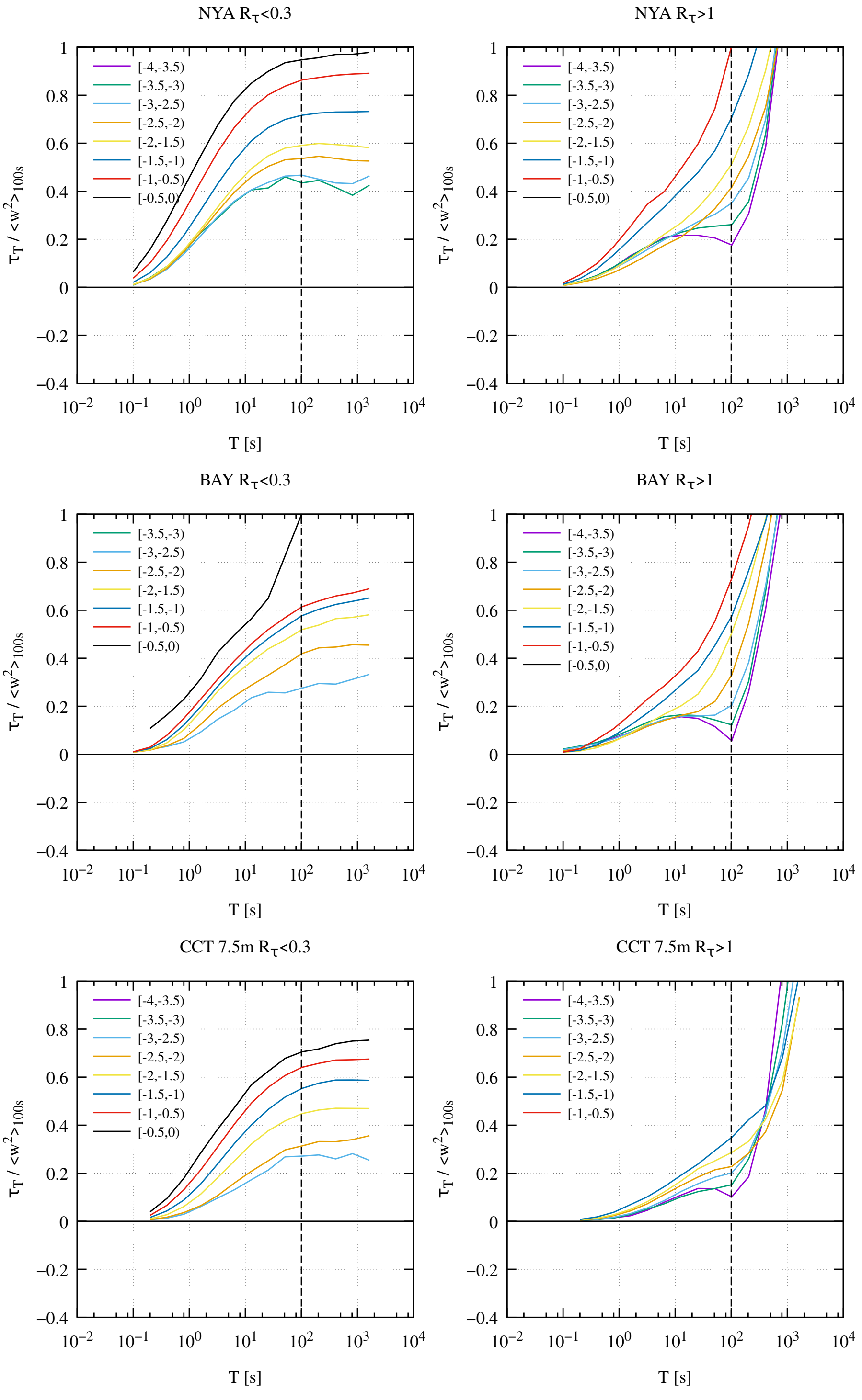

Figure S7: As in Fig. 15, but for the modulus of the shear stress, τ_T

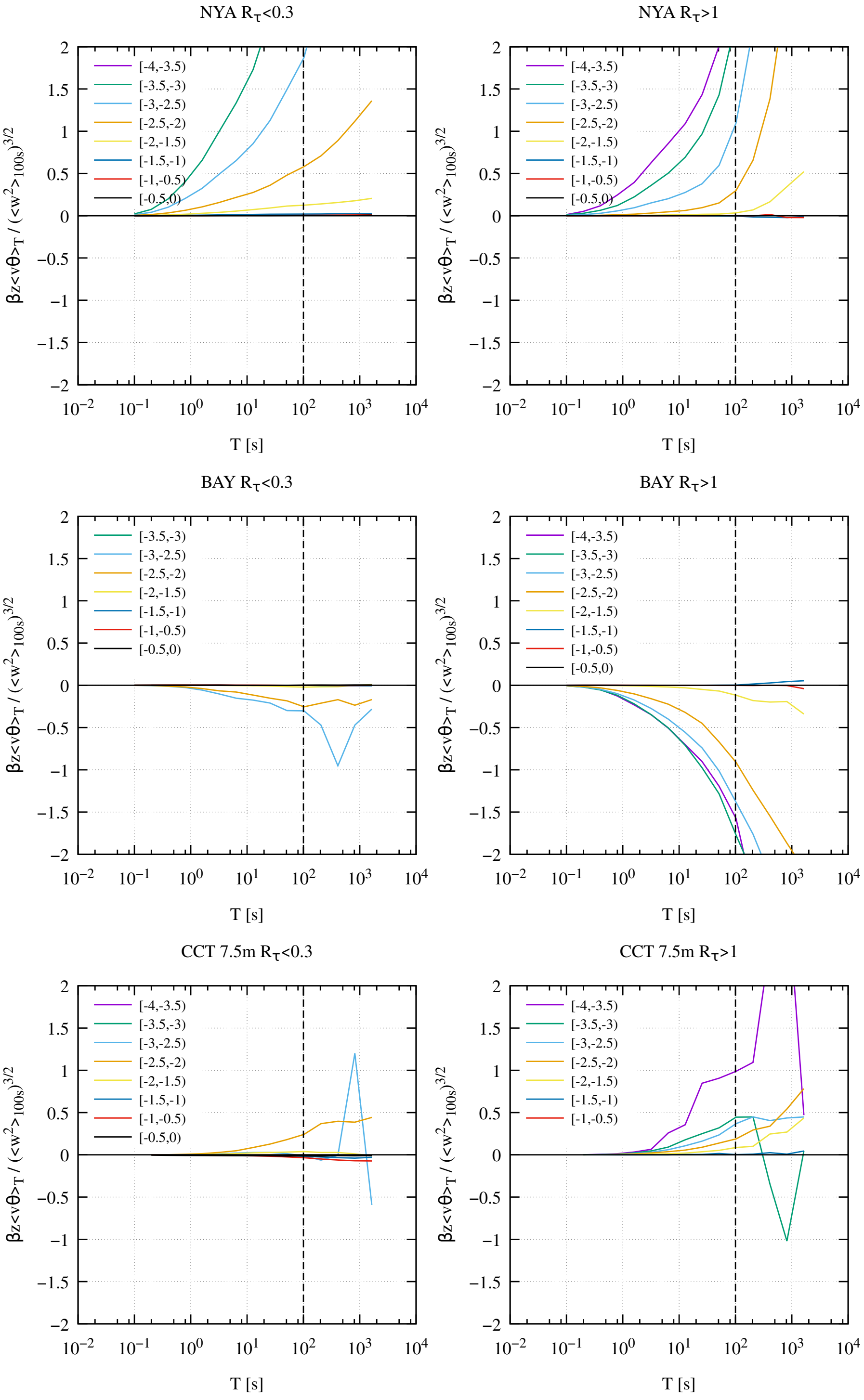

Figure S8: As in Fig. 16, but for the stream-wise heat flux, $\langle v\theta\rangle_T$.

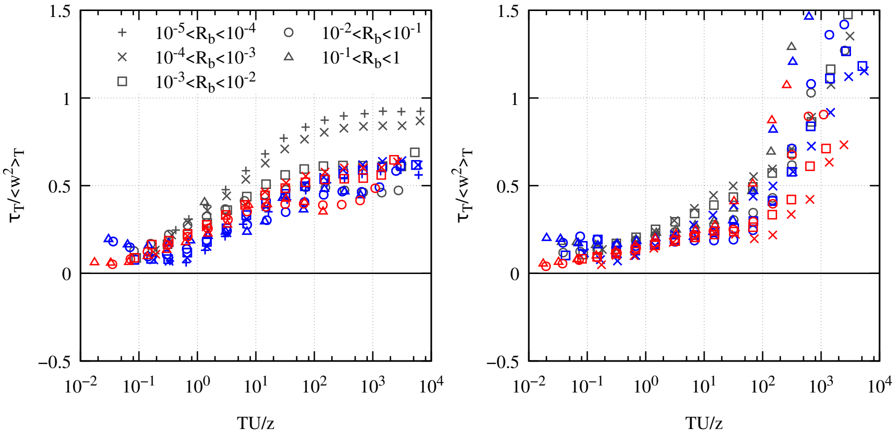
(a) $R_\tau < 0.3$

(b) $R_\tau > 1$

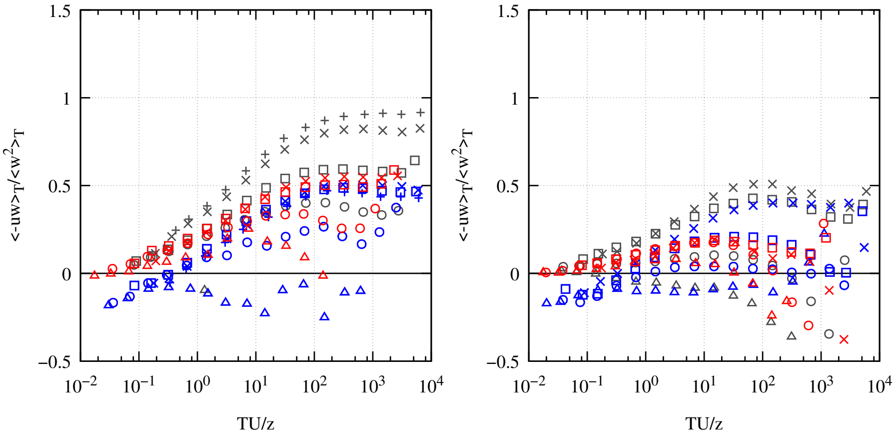
(c) $R_\tau < 0.3$

(d) $R_\tau > 1$

Figure S9: As in Fig. 17, but vs TU/z

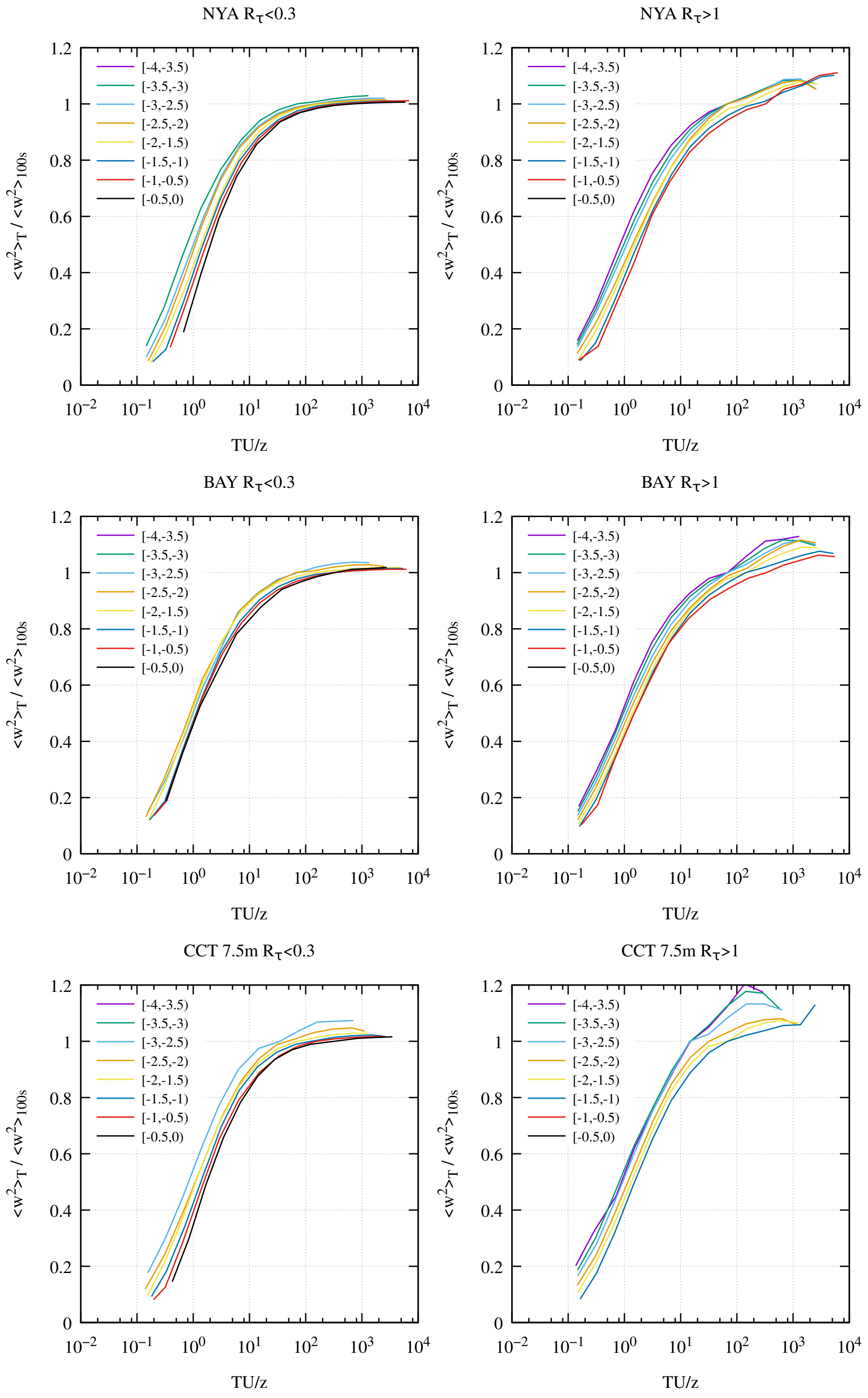

Figure S10: As in Fig. 15, but for the vertical velocity variance, $\langle w^2 \rangle_T$, and vs the non-dimensional averaging time TU/z.

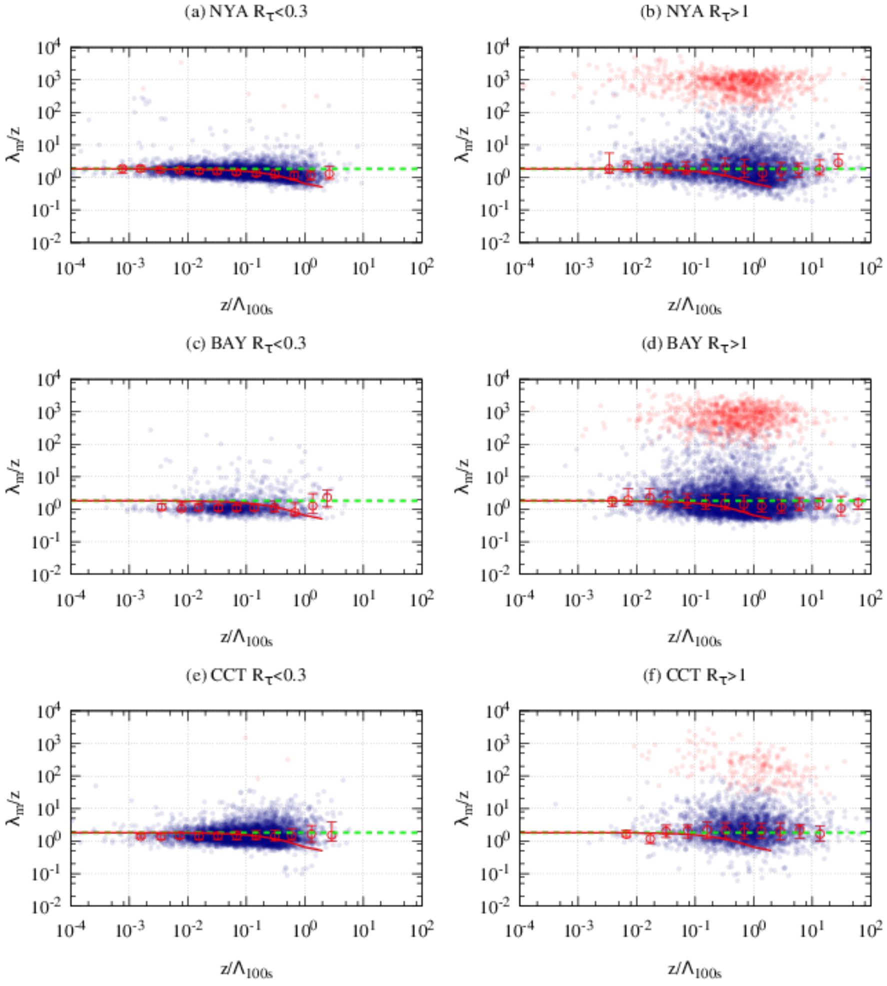

Figure S11: As in Fig. 18, but with $z/\Lambda_{100\mathrm{s}}$ as stability parameter. The red curve is the similarity relationship from Kaimal and Finnigan (1994); the green dashed line, its neutral limit.

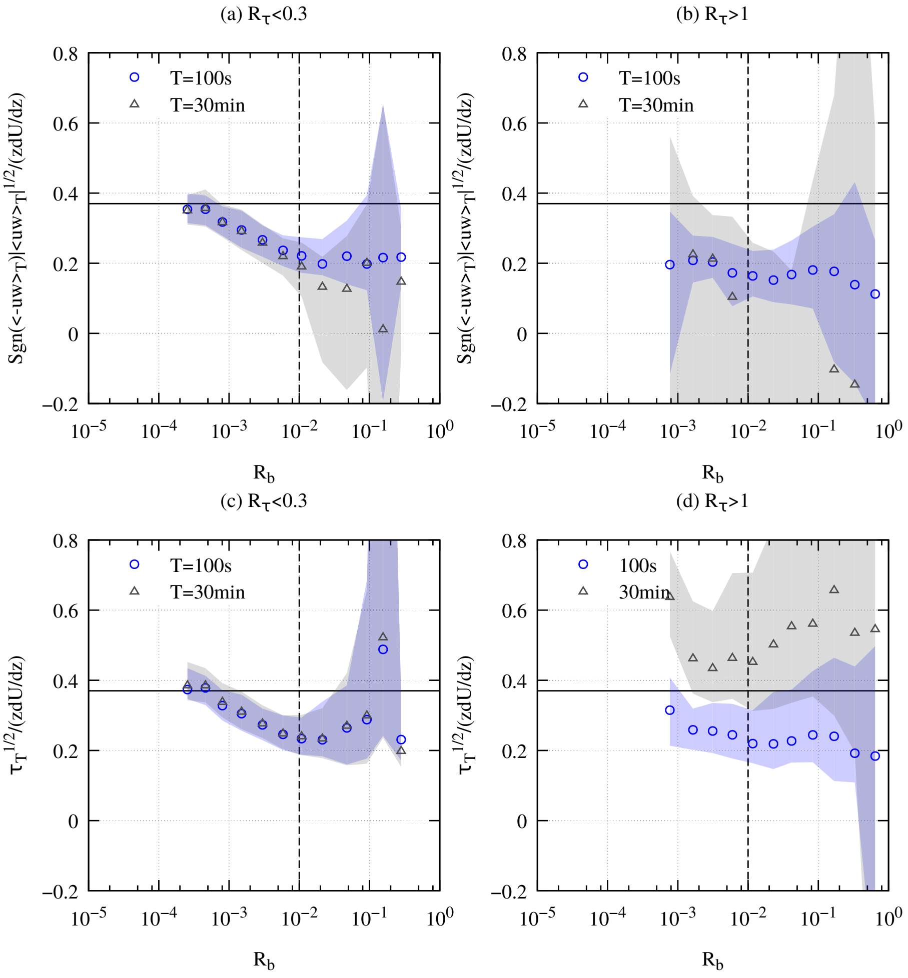

Figure S12: Flux-gradient relationship, i.e. $(u_*)_T/(z\partial U/\partial z)$, with $(u_*)_T = \mathrm{Sgn}(-\langle uw\rangle_T)| - \langle uw\rangle|^{1/2}$ and $(u_*)_T = \tau_T^{1/2}$, vs R_b, for $T = 100\,\mathrm{s}$ and $30\,\mathrm{min}$, and for $R_\tau < 0.3$ and > 1. Data are binned in R_b: median values (open symbols) and 25th–75th percentile range (shaded areas) are reported. The value 0.37 (i.e., the von Karman constant for $R_\tau < 0.3$) is also reported. Data refer to CCT $z = 7.5\,\mathrm{m}$.

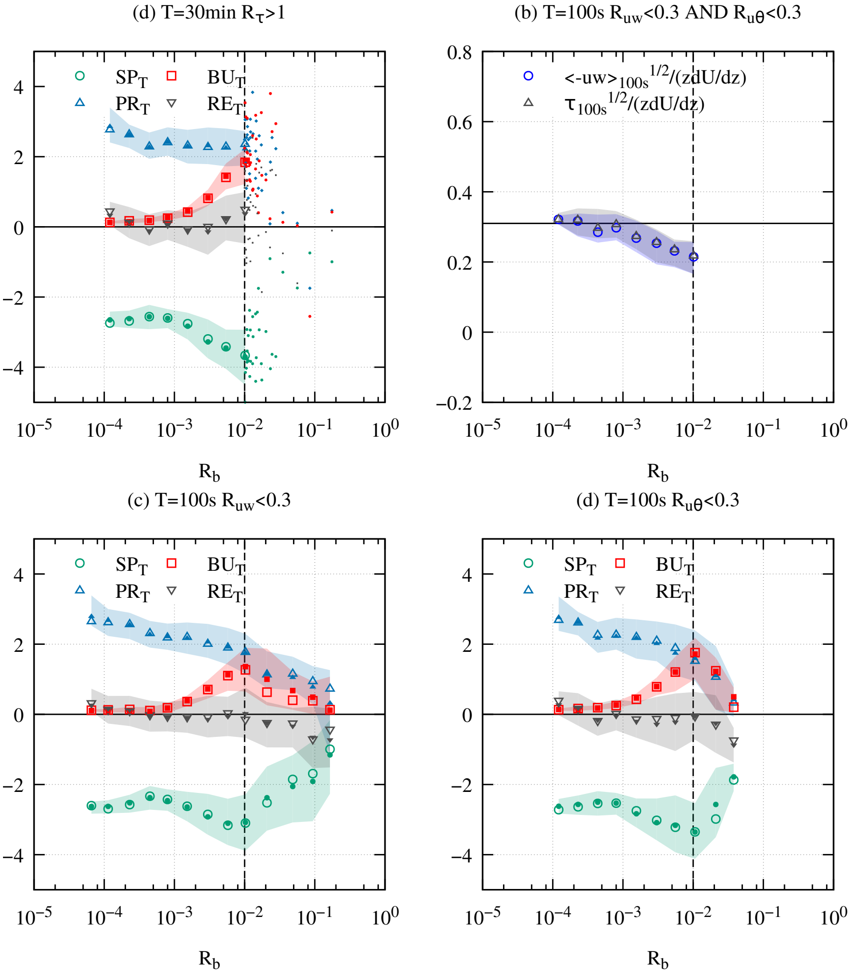
(d) T=30min R_τ>1

(b) T=100s R_{uw}<0.3 AND $R_{u\theta}$<0.3

(c) T=100s R_{uw}<0.3

(d) T=100s $R_{u\theta}$<0.3

Figure S13: As in Fig. 21a, but for alternative data selection: (a) $R_{uw} < 0.3$ AND $R_{u\theta} < 0.3$; (c) $R_{uw} < 0.3$; (d) $R_{u\theta} < 0.3$. (b) is the flux-gradient relationship for data selected as in (a). Data refer to CCT $z = 7.5\,\text{m}$.